Investigation of Frustrated Quasi-One-Dimensional Quantum Spin-Chain Materials

by

Kevin Caslin

A THESIS SUBMITTED IN PARTIAL FULFILMENT OF
THE REQUIREMENTS FOR THE DEGREE OF

DOCTOR OF PHILOSOPHY

in

The Faculty of Mathematics and Sciences

Department of Physics

BROCK UNIVERSITY

September 14, 2015

In presenting this thesis in partial fulfilment of the requirements for an advanced degree at the Brock University, I agree that the Library shall make it freely available for reference and study. I further agree that permission for extensive copying of this thesis for scholarly purposes may be granted by the head of my department or by his or her representatives. It is understood that copying or publication of this thesis for financial gain shall not be allowed without my written permission.

(Signature) _____

Department of Physics

Brock University
St.Catharines, Canada

Date _____

Abstract

Copper arsenite $CuAs_2O_4$ and Copper antimonite $CuSb_2O_4$ are S=1/2 (Cu^{2+} $3d^9$ electronic configuration) quasi-one-dimensional quantum spin-chain compounds. Both compounds crystallize with tetragonal structures containing edge sharing CuO_6 octahedra chains which experience Jahn-Teller distortions. The basal planes of the octahedra link together to form CuO_2 ribbon-chains which harbor Cu^{2+} spin-chains. These compounds are magnetically frustrated with competing nearest-neighbour and next-nearest-neighbour intrachain spin-exchange interactions. Despite the similarities between $CuAs_2O_4$ and $CuSb_2O_4$, they exhibit very different magnetic properties. In this thesis work, the physical properties of $CuAs_2O_4$ and $CuSb_2O_4$ are investigated using a variety of experimental techniques which include x-ray diffraction, magnetic susceptibility measurements, heat capacity measurements, Raman spectroscopy, electron paramagnetic resonance, neutron diffraction, and dielectric capacitance measurements.

$CuAs_2O_4$ exhibits dominant ferromagnetic nearest-neighbour and weaker antiferromagnetic next-nearest-neighbour intrachain spin-exchange interactions. The ratio of the intrachain interactions amounts to $J_{\mathrm{nn}}/J_{\mathrm{nnn}} \approx$ -4.1. $CuAs_2O_4$ was found to order with a ferromagnetic groundstate below $T_{\mathrm{C}} \approx 7.4$ K. An extensive physical char-

acterization of the magnetic and structural properties of $CuAs_2O_4$ was carried out. Under the effect of hydrostatic pressure, $CuAs_2O_4$ was found to undergo a structural phase transition at $\approx$ 9 GPa to a new spin-chain structure. The structural phase transition is accompanied by a severe alteration of the magnetic properties. The high-pressure phase exhibits dominant ferromagnetic next-nearest-neighbour spin-exchange interactions and weaker ferromagnetic nearest-neighbour interactions. The ratio of the intrachain interactions in the high-pressure phase was found to be $J_{nn}/J_{nnn} \approx$ 0.3. Structural and magnetic characterizations under hydrostatic pressure are reported and a relationship between the structural and magnetic properties was established.

$CuSb_2O_4$ orders antiferromagnetically below $T_N \approx 1.8$ K with an incommensurate helicoidal magnetic structure. $CuSb_2O_4$ is characterized by ferromagnetic nearest-neighbour and antiferromagnetic next-nearest-neighbour spin-exchange interactions with $J_{nn}/J_{nnn} \approx$ -1.8. A (H, T) magnetic phase diagram was constructed using low-temperature magnetization and heat capacity measurements. The resulting phase diagram contains multiple phases as a consequence of the strong intrachain magnetic frustration. Indications of ferroelectricity were observed in the incommensurate antiferromagnetic phase.

Preface

List of Publications:

1) K. Caslin, R. K. Kremer, F. S. Razavi, M. Hanfland, K. Syassen, E. E. Gordon, and M.-H. Whangbo. **Submitted:** Physical Review B, (2015).

2) P. Reuvekamp, K. Caslin, Z. Guguchia, H. Keller, R. K. Kremer, A. Simon, J. Köhler, and A. Bussmann-Holder, Journal of Physics: Condensed Matter. **27**, 262201 (2015).

3) K. Caslin, R. K. Kremer, F. S. Razavi, A. Schulz, A. Muñoz, F. Pertlik, J. Liu, M.-H. Whangbo, and J. M. Law, Physical Review B **89**, 014412 (2014).

4) K. Caslin, R. K. Kremer, Z. Guguchia, H. Keller, J. Köhler, and A. Bussmann-Holder, Journal of Physics: Condensed Matter. **26**, 022202 (2014).

5) Z. Guguchia, K. Caslin, R. K. Kremer, H. Keller, A. Shengelaya, A. Maisuradze, J. L. Bettis Jr., J. Köhler, A. Bussmann-Holder and M.-H. Whangbo, Journal of Physics: Condensed Matter. **25**, 376002 (2013).

Acknowledgements

Firstly, I would like to thank Dr. F. Razavi for organizing and providing me with the opportunity to carry out my thesis research at the Max Planck Institute. I would also like to thank him for his continuous support throughout my academic career.

I would like to thank Dr. R. K. Kremer for everything he has done for me during my time at the Max Planck Institute, I had an incredible experience in Germany. I am truly grateful to have been able to work under him and learn from his expertise. I will miss our daily lunches together and 1 o'clock Wednesday group meetings.

Many thanks to my colleagues and friends Dr. J. Chun, Dr. J. M. Law, Dr. A. Bussmann-Holder, Dr. K. Syassen, B. Tuffy and Dr. V. Lau, who I have worked with at the Max Planck Institute. A special thanks to my office mate and good friend Dr. P. Reuvekamp for always giving me a hand in times of need. I would also like to thank all the Faculty members and students of the Brock physics department who I have studied along side over the years.

I am very grateful for the many collaborators I had the privilege of working with. I would especially like to thank F. Pertlik from Vienna University of Technology for providing the $CuAs_2O_4$ sample; A. Muñoz from Universidad de La Laguna for performing DFT calculations on lattice properties; M.-H. Whangbo from North Carolina

State University for providing many DFT calculations on spin-exchange parameters; J. M. Law from Hochfeld-Magnetlabor Dresden for performing TMRG calculations and measuring pulsed field magnetization; M. Hanfland from E.S.R.F. for measuring and refining the synchrotron x-ray diffraction data; M. T. Atanasova for providing the $CuSb_2O_4$ sample; T. Hansen from I.L.L. for assisting with the neutron diffraction measurements. Thank you to all the technicians at the Max Planck Institute who have assisted me, especially E. Brücher, G. Siegle, and S. Höhn from the Chemieservice group.

Thank you to my girlfriend Adrienne for supporting me, surprising me with home-made meals, being my travel companion on countless trips, and always being there for me.

Finally, thank you to my parents for their continuous love and support.

Contents

List of Tables

List of Figures

1 Introduction

Low-dimensional magnetic materials are a matter of continuous interest for many reasons. Of particular interest is their ability to realize a variety of exotic quantum groundstates. Furthermore, they are highly amenable to theoretical models and in some cases even fit exact analytical solutions. The importance of dimensionality in magnetism was first encountered by Ernst Ising in 1925 with his theoretical work on a one-dimensional chain of magnetic moments.[1] To his own surprise, Ising concluded that no long-range ordered state was possible in such a system for $T > 0$ K (T represents temperature). Subsequently, it was found that low-dimensionality can give rise to many physical phenomena which cannot be observed in three-dimensions. As proposed by Mermin and Wagner, the lack of long-range order at finite temperatures, even for $T \rightarrow 0$ K, is an important characteristic of some low-dimensional magnetic systems.[2] The absence of long-range magnetic ordering allows for the development of unconventional quantum groundstates in many systems. Although many low-dimensional compounds do experimentally show long-range order below a critical temperature since they are three-dimensional compounds, they still exhibit low-dimensional characteristics. A few particularly interesting one-dimensional magnetic phenomena are spinons in a S=1/2 Heisenberg chain[3], Haldane gaps in integer-spin chains[4, 5], and spin-Peierls distortions in S=1/2 antiferromagnetic chain systems[6–

8].

Experimental realizations of one-dimensional systems known as "spin-chains" are compounds characterized by a linear arrangement of magnetic ions within a three-dimensional crystal lattice. Neighbouring chains of magnetic ions have a sufficient distance between them such that they are nearly magnetically decoupled and constitute a quasi-one-dimensional chain. Due to small interchain interactions, no ideal one-dimensional magnetic system can be physically realized this way. However, many spin-chain materials exhibit spin-exchange interactions with $J_{\text{interchain}} << J_{\text{intrachain}}$ which enables investigations on good approximations of one-dimensional magnetic phenomena.

Despite being *quasi*-one-dimensional, many spin-chain compounds have been experimentally found to follow one-dimensional theoretical predictions well. For example, in the 1970s there was a great deal of interest in spin-Peierls transitions, a magnetic analog to the electronic Peierls transition of a one-dimensional crystal.[6–8] In 1975, the first experimental evidence of a spin-Peierls transition was reported for a few organic compounds.[9] In 1993, the first inorganic spin-Peierls material, $CuGeO_3$, was reported.[10] This transition only occurs in S=1/2 antiferromagnetic chains that have a spin-phonon coupling which dominates any interchain interactions. A magnetoelastic dimerization occurs which separates the spin-chains into singlet spin-pairs, each with S=0, leading to a non-magnetic groundstate and a finite energy gap to a magnetic excited state. To date, there are only a hand full of known materials which exhibit a spin-Peierls transition.

In the 1980s, Haldane established the principal difference between one-dimensional chains of integer and half-integer spins.[4, 5] Haldane predicted that a S=1, 2, 3,... antiferromagnetic chain groundstate would develop an energy gap at q=0, referred to as a "Haldane Gap". Only a few compounds have experimentally realized the

Haldane groundstate, many of these compounds contain Ni^{2+} (S=1) magnetic ions. Some examples are $CsNiCl_3$[11, 12], Y_2BaNiO_5[13, 14], and $RbNiCl_3$[15, 16].

In 1981, Faddeev and Takhtajan revealed the spinon nature of the magnetic excitation of a S=1/2 antiferromagnetic Heisenberg chain.[3] Using the Bethe-Ansatz exact solution as a starting point, they argued that a spinon is a S=1/2 excitation as compared to the general S=1 magnon excitation.[3, 17] Spinons are created in pairs and are essentially propagating domain walls which create a 180° phase flip. Thus, the excitation spectrum of a spin-1/2 antiferromagnetic Heisenberg chain constitutes a continuum of non-interacting pairs of spinons.[18] Experimentally, these excitations have been observed using inelastic neutron scattering on a number of compounds including $KCuF_3$[19, 20], $CuGeO_3$[21, 22], and $LiCuVO_4$[23].

Lately, there has been a great deal of interest in one-dimensional systems which contain CuX_2 (X = O, Cl, Br) ribbon-chains with competing intrachain spin-exchange interactions. The ribbon-chains in such compounds may constitute quasi-one-dimensional magnetic chains with competing nearest- and next-nearest-neighbour intrachain interactions. The magnetic frustration may lead to unusual magnetic groundstates, for example, an antiferromagnetic incommensurate helicoidal ordering.[24–27] Compounds in which this has been observed are $LiCuVO_4$[28, 29], $CuBr_2$[30], $CuCl_2$[31], $LiCu_2O_2$[32, 33], $PbCu(OH)_2SO_4$[34, 35], and $NaCu_2O_2$[36, 37]. Sometimes the incommensurate antiferromagnetic ordering is accompanied with magnetoelastic distortions which may induce ferroelectric ordering across the ribbon-chains.[38] To date, this effect has been experimentally reported in only a few compounds including $LiCuVO_4$[39], $CuBr_2$[30], $CuCl_2$[40], and $LiCu_2O_2$[33].

Compounds which contain CuX_2 ribbon-chains are essential because they allow for investigations into the interplay of one-dimensionality and magnetic frustration. Multiferroicity is a highly sought after physical phenomenon which has great potential

for application in fields such as computer memory storage. It would allow for the switching of a memory bit to be achieved using an electric field rather than a magnetic field. Developing the fundamental knowledge around the processes giving rise to multiferroicity will allow for a clearer picture of what to search for in new naturally occurring minerals or how to artificially engineer them (such as multi-layer thin-films).

In this thesis, I investigate the quasi-one-dimensional cuprate systems $CuAs_2O_4$ and $CuSb_2O_4$. Physical characterizations of these systems are studied with a focus on the magnetic and structural properties. Correlations between the structural characteristics of the spin-chain distortions and the quasi-one-dimensional magnetic behaviour are examined. Both systems contain CuO_2 ribbon-chains in their crystal structures with Jahn-Teller distortions and competing intrachain spin-exchange interactions. $CuAs_2O_4$ is found to exhibit a ferromagnetic groundstate in proximity to a quantum critical point. With the application of external pressure, I investigate how this groundstate is altered. $CuSb_2O_4$ exhibits an incommensurate antiferromagnetic groundstate with helicodial ordering. Indications of induced ferroelectricity in the magnetic groundstate were observed.

2 Magnetism in One-Dimensional Cuprates

Cuprates make up many of the one-dimensional compounds known to date. The Cu^{2+} ion, $3d^9$ electronic configuration with one spin-hole in the $3d$ shell, constitutes an almost ideal S=1/2 magnetic ion. Generally, the Cu^{2+} ions in such compounds interact via super-exchange interactions through mediating O^{2-} ions. Low-dimensional magnetism in the cuprate family notably came into focus through high-T_C superconductors; however, low-dimensional cuprates have a large variety of interesting properties to offer. In this chapter, I will briefly review fundamental concepts of magnetism relevant to this thesis work and then describe how one-dimensional cuprates are formed in nature.

2.1 Long-Range Magnetic Ordering

In an atom with an open electron shell, the unpaired electrons carry a net magnetic moment due to their intrinsic spin and angular orbital momenta. Exchange interactions between magnetic moments is a consequence of the Coulomb repulsion and the requirement for an antisymmetric wavefunction arising from the Pauli exclusion principle. Hence, exchange interactions and long-range magnetic ordering are quantum mechanical phenomena. When all the magnetic moments in a magnetic

compound reach an equilibrium orientation, the system is said to be in a long-range ordered state. Long-range magnetic order is a result of broken symmetry since a paramagnetic disordered system with randomly fluctuating magnetic moments will have rotational invariance. Additional consequences of broken symmetry are phase rigidity and the formation of well-defined excitations.[41] Phase rigidity implies that the system has an energetic preference to maintain its current state. Symmetry does not gradually change, it is either present or absent with no in-between state. Thus, phase-transitions are sharp abrupt changes between ordered (broken-symmetry) and disordered (high-symmetry) states which can be experimentally observed.[41] Long-range magnetic ordering can be observed by the formation of a macroscopic magnetization in a sample. Another method of investigating long-range magnetic order is through magnetic excitations. Magnetic excitations (magnons or spinons) are analogous to phonons in a crystal lattice; they are the quantized disturbance waves in magnetically ordered systems.

It is a common characteristic of low-dimensional magnetic systems to exhibit short-range magnetic correlations, commonly referred to as "short-range order".[42–45] In a short-range ordered system, the correlations of the magnetic moments do not extend over the entire crystal but are confined to a smaller average temperature dependent correlation volume. Effects from short-range magnetic ordering experimentally show up as characteristic phenomena. For example, common experimental observations are broad maxima ('humps') in the magnetic susceptibility and heat capacity measurements.[42–45]

A magnetic compound can be described by the magnetic lattice dimensionality, d, and the spin-model (or spin dimensionality), d. The magnetic lattice dimensionality is related to the crystallographic structure and describes whether the magnetic lattice can be represented by chains ($d = 1$), planes (d=2), or a network (d=3). The spin-

model describes the anisotropy experienced by the magnetic moments. The Ising model describes magnetic moments which are confined to align either up or down along one direction (d=1). The XY-model describes magnetic moments which are confined to orient within a plane with no perpendicular component (d=2). The Heisenberg-model describes isotropic magnetic moments (d=3). Long-range magnetic ordering is generally a three-dimensional effect, however, for low-lattice-dimensions (d = 1,2), it is influenced by the spin-model of the system. In three-dimensions at finite temperatures, long-range magnetic ordering is possible for all spin-models. In two-dimensions, long-range magnetic ordering is not possible at finite temperatures for both the Heisenberg and XY spin-models with finite range interactions. In a few Ising model cases, a phase transition is possible with an exact solution; some examples are the Onsager solution for a square lattice[46], and the exact solutions for triangular and honeycomb lattices[47]. In one-dimension, no long-range magnetically ordered groundstate is possible for any spin-model. Thus, short-range ordering effects may dominate the experimental observations.[42–45]

2.1.1 Ferromagnetism

The defining property of a ferromagnetic (FM) ordered state is the existence of a spontaneous magnetization for $T < T_c$ (the Curie temperature). Spontaneous magnetization is due to a parallel alignment of magnetic moments in the absence of a magnetic field. In the presence of an applied magnetic field for $T < T_c$, the magnetic moments tend to align along the field lines and remain in this state even after the field is removed. For $T > T_c$, thermal fluctuations will destroy the magnetically ordered state resulting in a paramagnetic phase. Generally, a ferromagnet can be

well described by the following Hamiltonian,

$$\hat{H} = -\sum_{ij} J_{ij}^{xx} \hat{S}_i^{\,x} \cdot \hat{S}_j^{\,x} + J_{ij}^{yy} \hat{S}_i^{\,y} \cdot \hat{S}_j^{\,y} + J_{ij}^{zz} \hat{S}_i^{\,z} \cdot \hat{S}_j^{\,z} - g\mu_{\mathrm{B}} \sum_i \hat{S}_i \cdot \vec{H}, \qquad (2.1)$$

where $J_{ij}^{DD}(>0)$ is the exchange integral between spin i and spin j in the D-direction. The second sum in the Hamiltonian describes the contribution from an applied magnetic field, $\vec{H}$. In many compounds, not only are nearest-neighbouring (NN) spin interactions important, but the next-nearest-neighbour (NNN) and sometimes even further neighbour spin-exchange interactions are significant.

2.1.2 Antiferromagnetism

In an antiferromagnetic (AFM) ordered state, $T < T_N$ (the Néel temperature), neighbouring magnetic moments tend to align antiparallel, for $T > T_N$ the system transitions to a paramagnetic state. Generally, the Hamiltonian in Eq. 2.1 can be used to describe an antiferromagnet with $J_{ij} < 0$. An antiferromagnetic system is sensitive to the direction and strength of an applied magnetic field. If a relatively weak field is applied parallel to a particular moment, its neighbours will both be antiparallel to the field, thus, it is no longer energetically favorable (nor unfavorable) for the moments to align along the field.[41]

Antiferromagnetic systems can undergo two different field induced transitions which can be described by the interplay of internal and external fields. The internal exchange field H_{exch} represents the effective strength of the magnetic exchange interactions between magnetic moments. The internal anisotropy field H_{ani} represents the effective strength of the magnetic easy-axis. The external applied field H_{app} represents the magnitude of a laboratory applied magnetic field. A "spin-flip" transition occurs when the applied magnetic field is strong enough to overcome the antiferromagnetic

coupling ($H_{\text{app}} > H_{\text{exch}}$) and "flip" the spins to a ferromagnetic-like orientation. A "spin-flop" transition occurs when an applied field is strong enough to overcome the internal anisotropy fields of the crystal structure but not stronger than the exchange field such that antiferromagnetic order is maintained ($H_{\text{exch}} > H_{\text{app}} > H_{\text{ani}}$). All the spins will rotate ("flop") out of the easy-axis direction such that they are perpendicular to the field. As the applied field is increased further, all the moments tilt slightly along the field resulting in an overall magnetization until the applied field overcomes the exchange field (spin-flip), see Figure 2.1.

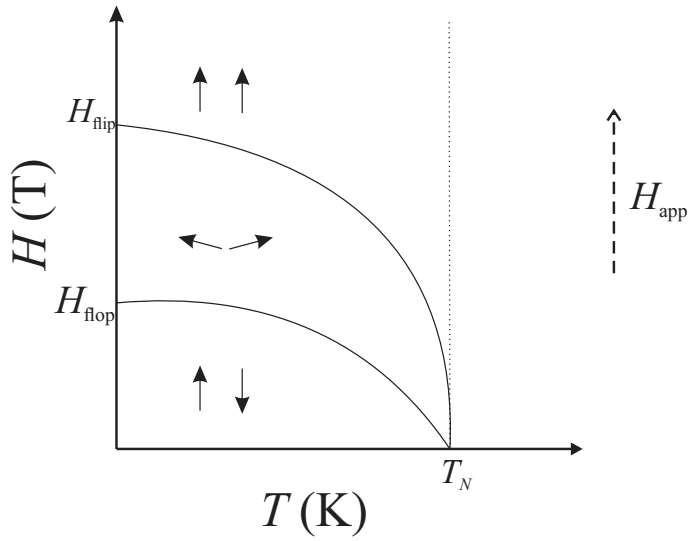

Figure 2.1: **Spin Transitions.** A (T, H) diagram depicting a spin-flop transition at H_{flop} and a spin-flip transition at H_{flip}. The magnetic alignment is represented by two arrows for each phase with respect to the applied field.

Antiferromagnetism is somewhat more diverse than ferromagnetism due to the large variety of ordering, excitations, and groundstates. Antiferromagnetism can lead to phenomena such as ferrimagnetism or incommensurate ordering, and can exhibit exotic excitations such as spinons. In one-dimension, antiferromagnetic ordering can lead to groundstates with Haldane gaps or spin-Peierls distortions.

2.1.3 Magnetic Frustration

In a magnetically frustrated system, competing interactions result in a situation where not every spin-exchange interaction can be completely satisfied. Magnetic frustration can arise from the geometry of the system, e.g., an AFM triangle (Figure 2.2 a), or from competing interactions between multiple neighbours (usually in one- and two-dimensional compounds), e.g., FM-NN interactions and AFM-NNN interactions in a spin-chain (Figure 2.2 b). Magnetic frustration in spin-chain systems from competing NN and NNN intrachain interactions can lead to complex ground-states such as helicoidal incommensurate ordering which has the potential to induce multiferroicity.[27, 38] Multiferroic compounds show ferroic order in multiple order parameters, such as magnetic, electric, or structural.

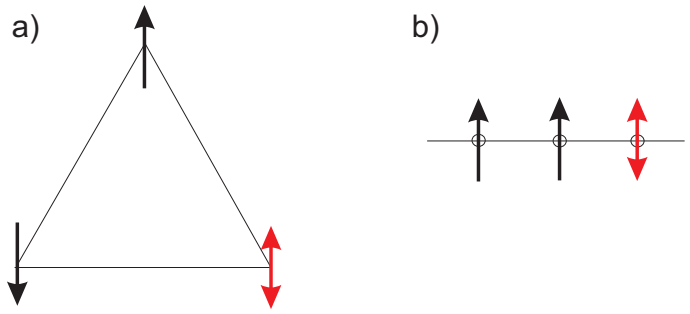

Figure 2.2: **Magnetic Frustration.** Two situations where magnetic frustration may occur: a) Geometric frustration in an antiferromagnetic triangle and b) competing FM-NN and AFM-NNN interactions in a one-dimensional chain.

2.1.4 Super-Exchange Interactions

The simplest interaction between two magnetic ions is a direct exchange. However, this requires a direct overlap of the electron wavefunctions which is not normally present in insulating materials relevant to this work. In cuprate spin-chain materials investigated in this thesis, the magnetic ions (Cu^{2+}) are separated by diamagnetic

anions (O^{2-}). The interactions between neighbouring moments is thus mediated by the intermediate anion. Exchange via an intermediate anion is known as a super-exchange interaction. This indirect interaction can act over a long-range compared to the direct interaction and is the dominant source of long-range ordering in most non-itinerant magnetic materials. Super-exchange interactions require hybridization of the magnetic d-orbitals with the non-magnetic p-orbitals of the intermediate anions. The unpaired electron of the d-orbital hops to the p-orbital while one electron from the p-orbital simultaneously hops to the next d-orbital, see Figure 2.3. The details, sign, and strength of the interaction are strongly dependent on the geometry of the $d-p-d$ hybridization, i.e., the super-exchange depends on the distances and angles between the participating ions.[48–50] Additionally, higher-lying orbitals may contribute to the exchange.

The range of a super-exchange interaction can extend beyond nearest-neighbour ions, however, super-exchange still falls off rapidly with distance.[51] In the case of next-nearest neigbouring moments, the exchange interactions occurs over two anions (Cu-O-O-Cu). This is sometimes referred to as a super-super-exchange. As commonly found in spin-chain systems, the NN cation-anion-cation angle is near 90° resulting in a small super-exchange interaction which is comparable in magnitude to the NNN interactions.[48–50] Such situations can exhibit a strong competition between NN and NNN interactions leading to large magnetic frustration.

2.2 Environmental Influence on Magnetic Ions

2.2.1 Crystal Electric Field

The crystal electric field, generated by the electric charges of surrounding ions, in a magnetic system has two major effects; firstly, the $2L + 1$ degeneracy of a given

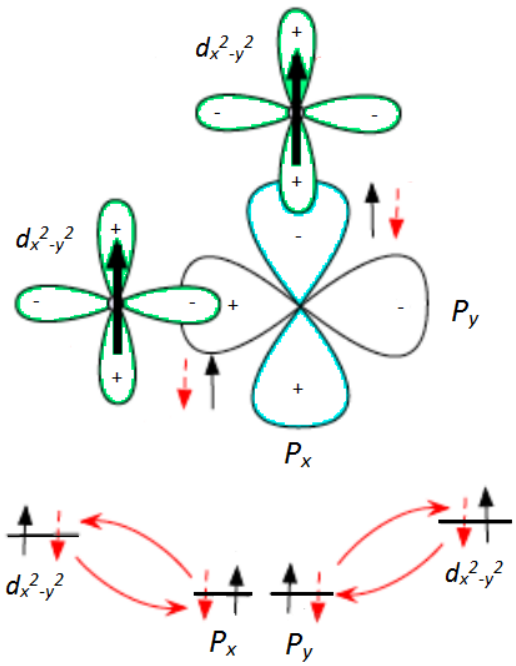

Figure 2.3: **Super-Exchange Interaction.** A representation of a 90° oriented Cu-O-Cu super-exchange interaction. The magnetic $d_{x^2-y^2}$ orbitals are the open Cu^{2+} orbitals. The P_x and P_y orbitals are the participating O^{2-} anion orbitals.

orbital angular momentum L is split; secondly, the spin momentum and angular momentum become partly decoupled.[52] An isolated transition metal ion (e.g Cu^{2+}) will have a five-fold degeneracy of the $3d$ levels. Once the transition metal ion is exposed to a crystal electric field originating from its neighbouring ions, the five-fold degeneracy is lifted. The details of the splitting are dependent on the symmetry of the crystal environment and the number of d electrons of the ion. For an octahedral environment, the five-fold degeneracy is split into a three-fold degenerate level, the t_{2g} triplet, and a two-fold degenerate level, the e_g doublet, separated by an energy gap ΔE (conventionally ΔE is named 10Dq), see Figure 2.4. For Cu^{2+}, ΔE is typically on the order of 20 000 cm^{-1}. The t_{2g} triplet is lowered in energy from the five-fold degenerate state by 40% of ΔE and the e_g doublet is raised in energy from the fivefold-degenerate state by 60% of ΔE. The crystal field splitting gap, ΔE, determines the physical colour of many insulating materials because ΔE is on the magnitude order of visible light. Most Cu^{2+} materials appear blue-green because $\Delta E \approx 650$ nm (red light).

The second significant effect of the crystal electric field is a quenching of the orbital angular momentum. This applies mainly to d-transition metal ions because the d-shells are the outer most electron shell and are in no way shielded from the crystal electric field which is the case for rare earth metals.[52] In the case of a $3d$ transition metal ion, orbital angular momentum quenching occurs because the influence of the crystal electric field on the outer d electrons is larger than the spin-orbit coupling. The crystal electric field constitutes a non-central Coulomb potential and consequently, L_z is no longer a good quantum number.[52] The d electrons become "locked" and L becomes quenched, in other words $< L > = 0$. As a result, the total magnetic moment is purely determined by the spin moment. The degree of angular momentum quenching is dependent on the crystal symmetry around the ion and the number of

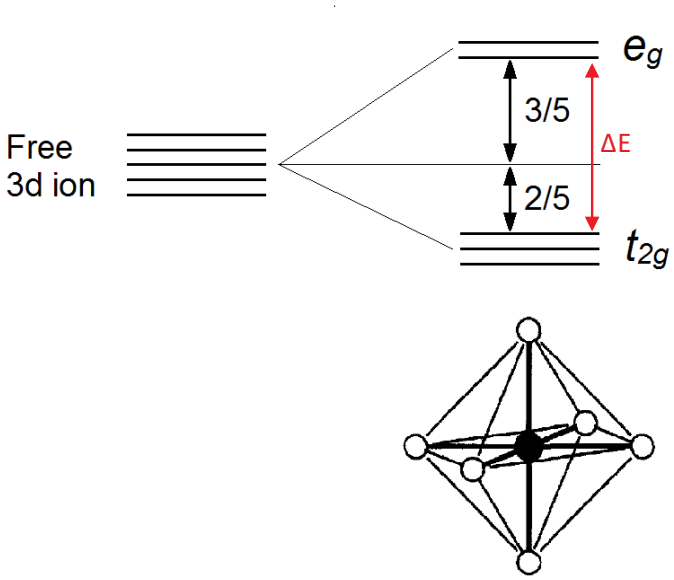

Figure 2.4: **Crystal Electric Field.** The effect of the crystal electric field on a $3d$ ion in an octahedral environment. The degeneracy of the $2L+1$ levels is split. In this example of a $3d$ transition metal ion, $L=2$ and the five-fold free ion energy level is split into the t_{2g} and e_g energy levels. The crystal electric field here is generated by the ions surrounding the $3d$ ion in an octahedral configuration.

valence electrons in the d shell.

For the situation of interest in this work, the Cu^{2+} transition metal ion is coordinated in an octahedral environment with a $3d^9$ valence shell. Although the orbital angular momentum is quenched, the effect of spin-orbit coupling cannot be completely ignored. Perturbations from spin-orbit coupling are found for instance in the electronic g-factor:

$$g_{\text{eff}} = g - f(\lambda) \tag{2.2}$$

where $f(\lambda)$ is linearly proportional to the spin-orbit coupling constant, λ. Generally, the magnitude of λ increases as one progresses through the transition metal series.[53] The sign of λ is positive for transition metal ions with less than half-filled shells, hence, $g_{\text{eff}} < g = 2$. The spin-orbit constant is negative for transition metal ions with more than half-filled shells, $g_{\text{eff}} > g = 2$.

2.2.2 Jahn-Teller Distortions

In addition to crystal field splittings, a magnetic transition metal ion may also experience Jahn-Teller effects which induce a structural distortion in the local environment.[54] Jahn-Teller effects arise from the degeneracy in either the t_{2g} levels, e_g levels, or a combination of both. The Jahn-Teller distortion depends on the symmetry of the local ion environment.

In the case of a magnetic Cu^{2+} ion with a $3d^9$ configuration, see Figure 2.5, there is a single spin-hole in the e_g doublet states which is degenerate with the $d_{3r^2-z^2}$ and the $d_{x^2-y^2}$ states. If this $3d^9$ ion is coordinated in an O_6 octahedron, for example, the local octahedral environment experiences a tetragonal distortion such that the two apical oxygens of the octahedron are pushed outwards, by convention in the z-direction. This distortion lowers the Coulomb repulsion between the Cu^{2+} $3d_{3r^2-z^2}$ orbital and the

$2p$ orbitals of the O^{2-} apical atoms. Hence, the $3d_{3r^2-z^2}$ is lowered in energy from its degenerate state with the $d_{x^2-y^2}$ level. Additionally, the tetragonal distortion causes the d_{xz} and d_{yz} levels of the t_{2g} triplet to drop in energy from a triple-degenerate state to a double-degenerate state, leaving the d_{xy} level non-degenerate. The magnitude of the energy gap depends on the magnitude of the structural distortions which varies from system to system.

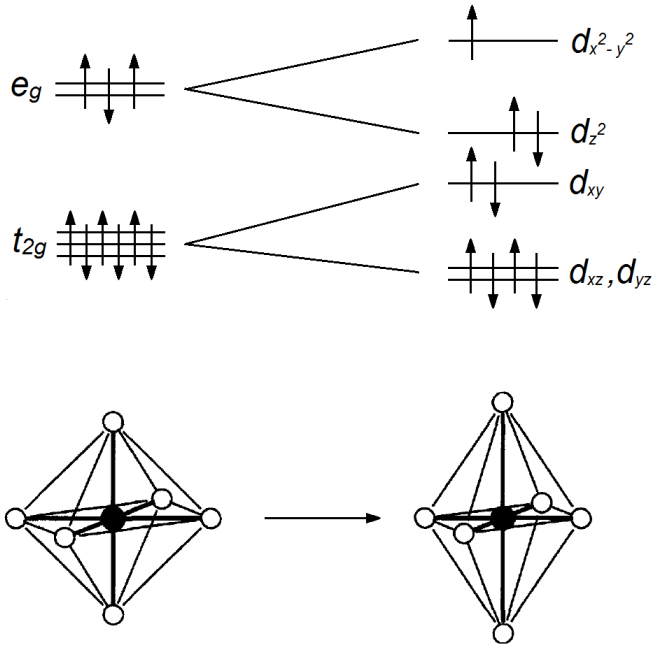

Figure 2.5: **Jahn-Teller Distortions.** The effect of Jahn-Teller distortions on a $3d$ ion in an octaherdral configuration. The elongation along the axial directions of the octahedron splits the degeneracy of the t_{2g} and e_g energy levels. In this example, the central (solid black) atom is the Cu^{2+} ion ($3d^9$) and the ligand (empty white) atoms are O^{2-} ions.

2.3 Realizations of Cu Spin-Chains

Quasi-one-dimensional spin-chains can be realized in crystals with magnetic moments which align in a linear fashion with strong spin-exchange interactions along

the direction of propagation. In compounds pertaining to this work, the Cu^{2+} spin-chains are located within CuO_2 ribbon chains which are formed in the basal planes of edge sharing CuO_6 octahedra. The basal plane of a CuO_6 octahedron consists of a central Cu^{2+} ion with four O^{2-} ions which are labeled as O(2). The two apical oxygen ions of the octahedron are labeled as O(1). Figure 2.6 displays the crystal structure of CuX_2O_4 (X = As, Sb), a typical Cu spin-chain crystal structure. In the crystal structure, neighbouring CuO_6 octahedra chains are connected by XO_3 groups.

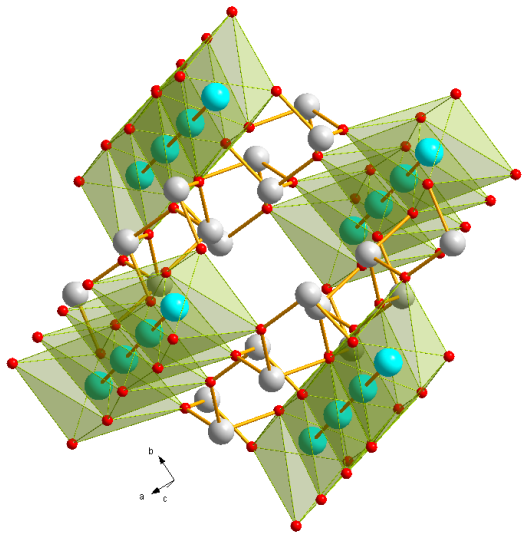

Figure 2.6: **Spin-Chain Crystal Structure.** A general crystal structure of a spin-chain cuprate compound. The cyan spheres are Cu^{2+}, the red spheres are O^{2-} and the white spheres are As^{3+} or Sb^{3+}. The Jahn-Teller elongated CuO_6 octahedra are highlighted in green, the spin-chains are formed in the linking basal planes of these octahedra.

When these chains are sufficiently far apart in the crystal structure, it is typically found that $J_{\text{intra}} >> J_{\text{inter}}$, where J_{intra} and J_{inter} are the intra- and interchain interactions. In this scenario, the interchain interactions, which cannot be realistically avoided, only become significant at low temperatures and source any long-range ordered state. The significant intrachain interactions are Cu-O(2)-Cu NN super-exchange interactions and Cu-O(2)-O(2)-Cu NNN super-super-exchange interactions.

Since the super-exchange interactions are sensitive to the geometry of the spin-chains, often corrugation or distortion of the octahedra influence the NN and NNN spin-exchange interactions, J_{nn} and J_{nnn}. It is typically found that in cuprate spin-chain compounds, the NN interactions are FM and the NNN interactions are AFM, both of comparable magnitude. This leads to an inherent intrachain frustration which adds severe complexity to the magnetic properties and can lead to unconventional magnetic ground states.

2.4 S=1/2 Heisenberg Chain Magnetic Phase Diagram

A $T = 0$ magnetic phase diagram for a one-dimensional S=1/2 Heisenberg chain from coupled-cluster calculations of quantum many-body theory reported by R. Bursill *et al.*[55] is shown in Figure 2.7. It is related to the spin-exchange ratio, $\alpha = J_{\mathrm{nn}}/J_{\mathrm{nnn}}$, with the Hamiltonian:

$$\hat{H} = -J_{\mathrm{nn}} \sum_i (\hat{S}_i \cdot \hat{S}_{i+1} + \alpha^{-1} \hat{S}_i \cdot \hat{S}_{i+2}) \tag{2.3}$$

The phase diagram is mainly characterized by three regimes, Ferromagnetic, Antiferromagnetic, and Highly Frustrated. In the Ferromagnetic regime, the NN and NNN super-exchange interactions are both ferromagnetic (positive) or the NN interaction is ferromagnetic and much greater than the NNN interaction, regardless of its sign. In the Antiferromagnetic regime, the NN super-exchange interaction is antiferromagnetic (negative) and the NNN interaction is ferromagnetic or NN interaction is antiferromagnetic and much greater than the NNN interaction, regardless of its sign. In the Highly Frustrated phase, the NNN spin-exchange interaction

is antiferromagnetic, and comparable in magnitude to the NN interactions, which leaves the system in a state which cannot simultaneously satisfy the NN and NNN spin-exchange requirements.[56] Compounds which fall in the Frustrated phase of the diagram exhibit the most unconventional magnetic behaviour, it is these compounds which contain the prerequisites required for helicoidal ordering and potential ferroelectricity.[26, 57]

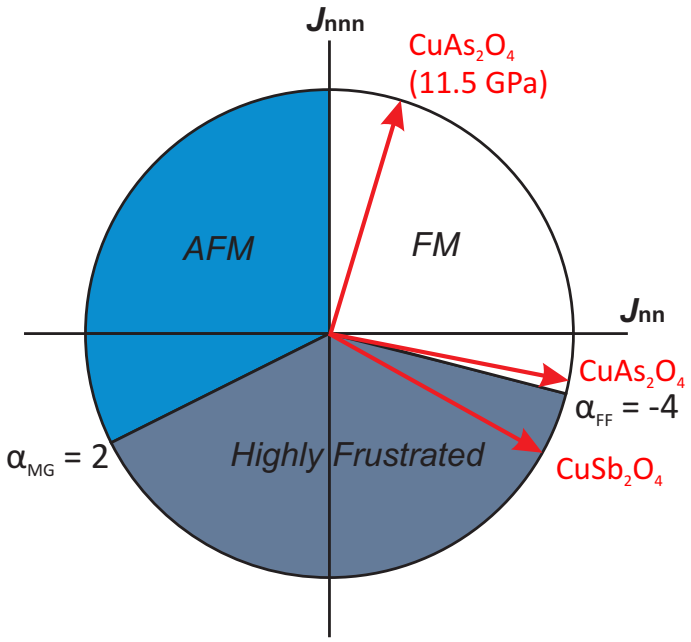

Figure 2.7: **S=1/2 Heisenberg Chain Phase Diagram.** Magnetic phase diagram for a S=1/2 Heisenberg chain with NN and NNN spin-exchange interactions based on $\alpha = J_{nn} / J_{nnn}$ constructed from the results reported by Ref. [55]. Note: Negative J values indicate antiferromagnetic and positive J values indicate ferromagnetic. The red arrows indicate the α positions of $CuAs_2O_4$ and $CuSb_2O_4$.

In the phase diagram, there are three points of significant interest. Firstly, at the boundary between the FM and Frustrated regimes is a quantum critical point, α_{FF} = -4, where a first-order phase transition occurs between ferromagnetic and frustrated groundstates. Secondly, at the boundary between the AFM and Frustrated regimes is the Majumdar-Ghosh quantum critical point $\alpha_{MG} = 2$. At the the Majumdar-Ghosh

point, α_{MG}, there is an exact groundstate solution,

$$\hat{H}_{\mathrm{MG}} = -J_{\mathrm{nn}} \sum_{i} (\hat{S}_i \cdot \hat{S}_{i+1} + \frac{1}{2} \hat{S}_i \cdot \hat{S}_{i+2}) \tag{2.4}$$

for the groundstate which consists of dimerized singlets with a gapped first excited state.[58, 59] The third point of interest is along the negative x-axis with $J_{\mathrm{nnn}} = 0$ and J_{nn} AFM. At this point, the groundstate is a spin-liquid.[26, 55, 57]

The phase diagram in Figure 2.7 was calculated for Heisenberg-type spin-chains. Calculations for deviations from Heisenberg type models to XY-type models, which can be accounted for with the parameter Δ, have been reported by Hikihara *et al.*[57] and Furukawa *et al.*[26]. A pure Heisenberg-type compound is represented by $\Delta = 1$ and a pure XY-type compound is represented by $\Delta = 0$. Anything in between can be expressed as 1 - Δ. Typically for one-dimensional cuprate compounds, $\Delta \gtrsim 0.95$, nearly Heisenberg-type, the slight deviation can be attributed to spin-orbit effects.[26, 57] However, for cuprate compounds in the Frustrated regime, the slight deviation introducing a small XY anisotropy may force the Cu^{2+} moments to the equatorial planes of the CuO_6 octahedra.[26, 57]

By evaluating the NN and NNN spin-exchange constants, J_{nn} and J_{nnn}, of a spin-chain cuprate, the groundstate phase diagram provides an estimation of the magnetic behaviour and groundstate of the compound. Furthermore, if Δ is determined, a more accurate estimation is possible.

2.5 Super-Exchange Interactions in Cuprate Spin-Chain Compounds

Historically, the Goodenough-Kanamori-Anderson (GKA) rules were a useful approach to characterize super-exchange interactions according to the atomic arrangement within a magnetic system.[48–50] For super-exchange interactions in Cu^{2+} systems with a Cu-X-Cu bridging angle, where X is the intermediate anion, the GKA rules propose a FM coupling for bridging angles close to 90° and an AFM coupling elsewhere. A FM exchange is expected for bridging angles close to 90° where two anion orbitals participate (Figure 2.3) and an AFM exchange is expected for an exchange with only one participating anion orbital. Side group/ligands and structural distortions may cause a deviation from a FM-AFM crossover angle of 90°. Many factors including higher-lying orbitals, direct exchange, geometry of the environment, and orbital degeneracies need to be considered. A number of DFT calculations based on the GKA rules for Cu^{2+} compounds which include the influence of side groups/ligands and distortions have been performed. Some of these calculations have been reported by Braden *et al.*[60] on the Cu-O-Cu system $CuGeO_3$, and more recently by Lebernegg *et al.*[61] on Cu-X-Cu, X = F, Cl, Br, systems, and also by Geertsma and Khomskii[62] on general Cu-O-Cu systems. All three studies come to a similar conclusion, proposing that the crossover angle, Φ_C, between FM and AFM coupling occurs between $\Phi_C \approx 95°$ - 98°. Figure 2.8 displays the results of DFT calculations reported by Braden *et al.*[60] describing the Cu-O-Cu coupling constant in $CuGeO_3$ versus the bridging angle. Experimentally, the crossover angle appears to be at $\Phi_C \approx 95.5°$, see Figure 2.9, which agrees with the calculations. Depending on whether the Cu-O-Cu bonding angle is above or below $\approx 95°$ in a particular compound can predict whether the interaction is FM or AFM. Furthermore, the closer the bonding angle is to the crossover

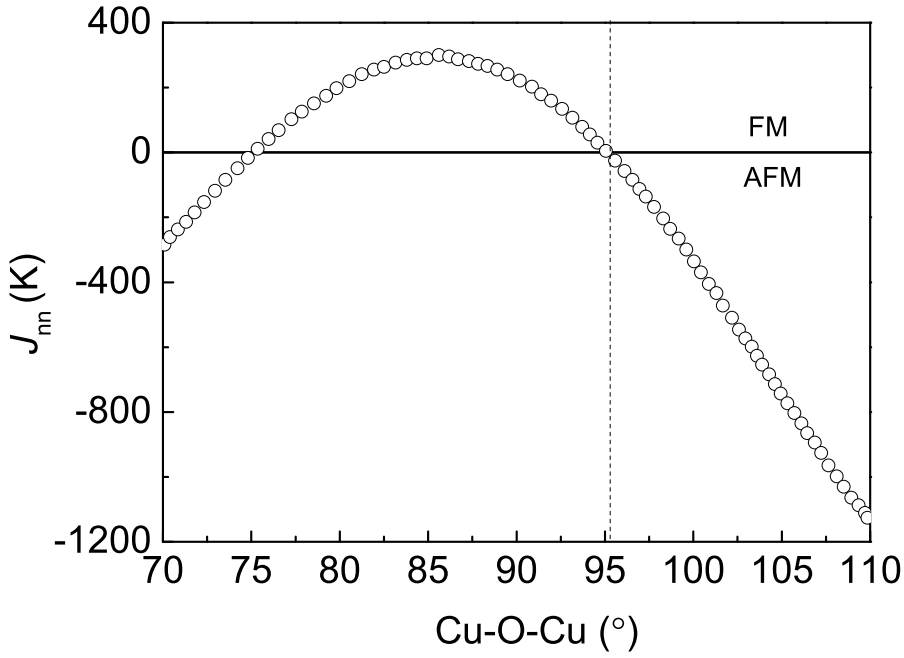

Figure 2.8: **Super-exchange versus Bridging Angle.** Graph constructed from the results reported by M. Braden *et al.*, [60], depicting how the Cu-O-Cu super-exchange interaction in $CuGeO_3$ is affected by the bridging angle for angles near 90°.

angle, the smaller its interaction becomes in magnitude.

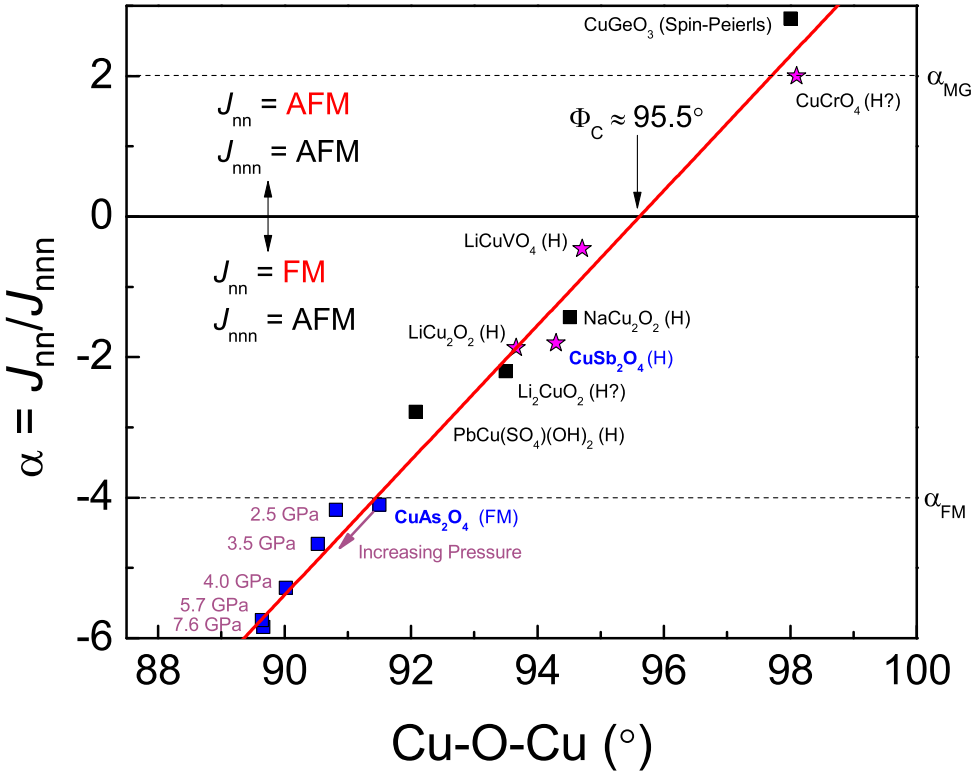

Figure 2.9: α **versus Cu-O-Cu Bridging Angle.** Summary of reported $\alpha = J_{\rm nn}/J_{\rm nnn}$ values for cuprate spin-chain compounds versus their Cu-O-Cu bridging angles ($J_{\rm nnn}$ AFM). The groundstate of each compound is listed in parentheses (H = helicoidal, FM = ferromagnetic). The three compounds with stars are found to exhibit ferroelectricity. The pressures listed in purple pertain to $CuAs_2O_4$ under the application of pressure. The compounds written in blue font are investigated further in this thesis work. The dashed lines at $\alpha_{\rm MG}$ and $\alpha_{\rm FM}$ represent the Majumdar-Ghosh and FM quantum critical points, respectively. References: $CuGeO_3$[63], $CuCrO_4$[64], $LiCuVO_4$[29], $NaCu_2O_2$[36], $LiCu_2O_2$[65], Li_2CuO_2[66], $PbCu(SO_4)(OH)_2$[35], $CuAs_2O_4$[67]

Figure 2.9 displays a collection of reported Cu-O-Cu angles and $\alpha = J_{\rm nn}/J_{\rm nnn}$ values for magnetically frustrated ($J_{\rm nnn}$ AFM) spin-chain cuprates. Near 90°, there is a linear relationship between the Cu-O-Cu bridging angle and $\alpha = J_{\rm nn}/J_{\rm nnn}$, with an intercept $\Phi_{\rm C} \approx 95.5°$. $J_{\rm nn}$ is AFM for angles above $\Phi_{\rm C}$ and FM for angles below $\Phi_{\rm C}$ in the linear regime near $\Phi_{\rm C}$. Apart from the comparatively large Jahn-Teller effect,

smaller structural distortions reflecting the bonding in the three-dimensional crystal become important. The sensitivity of the spin-exchange with respect to the bridging angle implies that secondary structural distortions significantly affect the magnetic properties of CuO_2 ribbon-chain compounds. Additional structural alterations may be introduced via external pressure and allow for an external tuning of the magnetic properties.

3 Experimental Methods

In this chapter, I will briefly describe the experimental techniques used in this thesis work with an account of the fundamental physics on which the experiment is based.

3.1 X-ray Diffraction

X-ray diffraction experiments are a useful method for characterizing crystal structures. The incident x-ray beam is diffracted by the electrons of the sample which are localized around the ions allowing for the identification of atomic positions in the sample. This measurement technique works by recording the Bragg diffraction angles and intensities of the x-ray beam which has been diffracted by a sample crystal. The incident x-rays are elastically scattered with an angle of 2θ by Bragg planes, which are separated by a distance d, and constructively interfere when their path length difference, $2d\sin\theta$, is a multiple of the wavelength, λ. This phenomenon can be expressed using Bragg's Law:

$$2d\sin\theta = \mathrm{n}\lambda \tag{3.1}$$

There is no energy transfer in elastic scattering but there is a momentum shift of

the incident x-rays, Δk. For constructive interference to occur, the scattering vector Δk must be equal to a reciprocal lattice vector. A geometric visualization, called the Ewald sphere, can be constructed over the reciprocal lattice where the diffraction condition is satisfied when a circle (in two-dimensions) of radius k intersects two reciprocal lattice points.

The measured x-ray diffraction reflections can be related to the unit cell dimensions of the sample with the 2θ angles at which they appear and the (hkl) indexing. In the orthorhombic case, the following relation holds:

$$d_{\mathrm{hkl}} = \lambda/2\sin(\theta) = \left(\frac{h^2}{a^2} + \frac{k^2}{b^2} + \frac{l^2}{c^2}\right)^{-\frac{1}{2}} \tag{3.2}$$

The exact relationship between d_{hkl} and the lattice parameters depends on the lattice classification of the unit cell. The measured diffraction pattern is indexed to a known unit cell, usually accomplished with a least squares matching algorithm refinement software, where the dimensions and symmetry of the matched unit cell are known. The atomic content of the unit cell is determined using the intensities of the Bragg reflections. The intensity of a Bragg reflection can be approximated using the square of the structure factor F_{hkl}:

$$F_{\mathrm{hkl}} = \sum_j f_j \exp\Big(- 2\pi i(hx_j + ky_j + lz_j)\Big) \tag{3.3}$$

Where f_j is the atomic form factor for the j^{th} atom which is dependent on the electron density distribution of each atom.

All the symmetry operations of a lattice form a mathematical group called a space group. This classification incorporates the lattice class (P, I, C, F, R) and the point-group elements. Generally, numbers in a space group represent rotational symmetry,

m represents a mirror reflection symmetry, i represents inversion symmetry, and numbers with a bar represent rotational-inversion. There are 230 crystallographic space groups which are used to represent the unit cell lattice classes and symmetries.

X-ray powder diffraction measurements were carried out on two-circle STOE Stadi P diffractometers, see Figure 3.1. Both Cu $K\alpha_1$ x-ray radiation ($\lambda = 1.54056$ Å) and Mo $K\alpha_1$ x-ray radiation ($\lambda = 0.70930$ Å) were used. Samples were ground and filled into 0.2 - 0.3 mm diameter quartz capillaries and rotated to reduce texture effects. Measurements were carried out for the appropriate 2θ range in 0.01 angular increments with a typical time constant of 90 seconds. Analysis of the diffraction patterns were performed using Rietveld profile refinements with FullProf Suite software.[68]

The Rietveld profile refinement method is a common approach for analyzing diffraction data. The Rietveld method fits profile points of a particular structure model to the entire diffraction pattern rather than fitting individual Bragg reflections. A trial structure is inputed into the Refinement software, a diffraction pattern is calculated for the trial structure, and a comparison to the measured pattern is performed. The trial structure is modified by adjusting parameters such as atomic positions, lattice parameters, thermal parameters, peak shape parameters, site occupation, etc., until a best-fit match is obtained. The Refinement software uses a least squares matching algorithm to determine the best-fit match.

In certain cases, measured diffraction patterns require data corrections. The most common data corrections are the Lorentz correction, polarization correction, and absorption correction. The Lorentz correction is related to offsets from the geometry of the collection mode, the polarization correction accounts for a partial polarization of the x-ray beam upon reflection from the sample, and an absorption correction accounts for x-rays which have been absorbed rather than scattered.

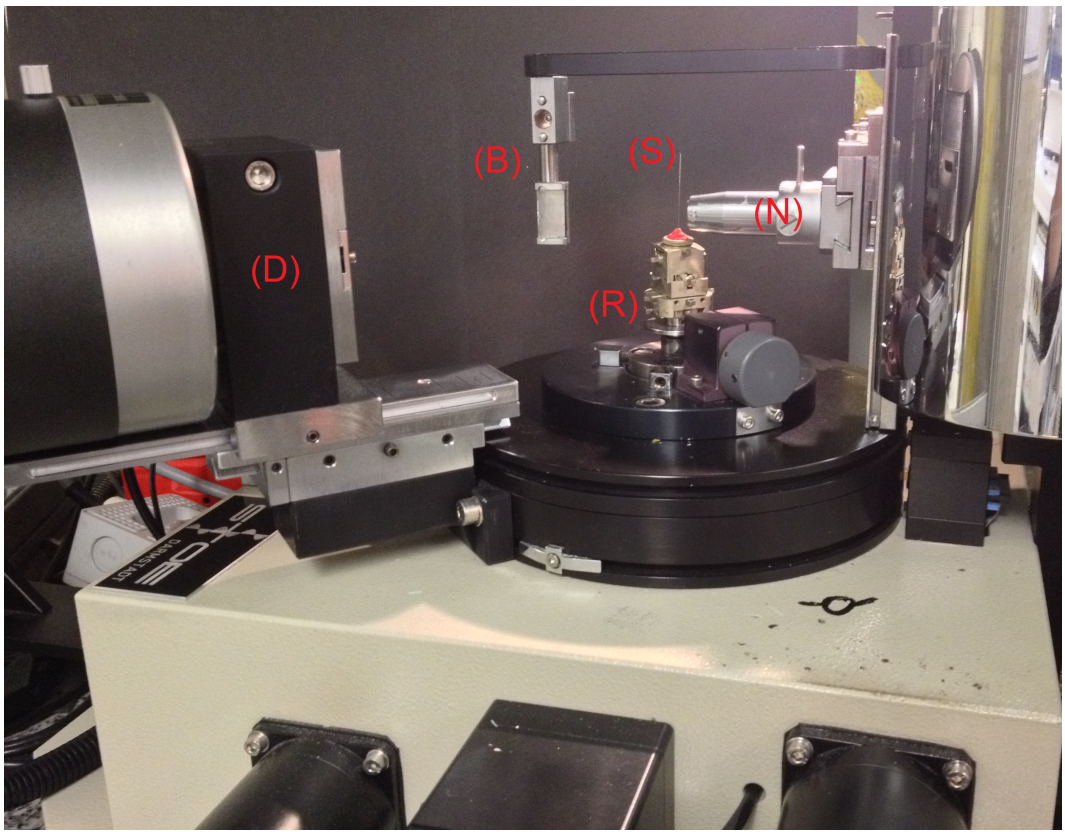

Figure 3.1: **X-ray Diffractometer**. A schematic of the Mo-radiation STOE Stadi P x-ray diffractometer. In the Figure, (S) designates the sample capillary, (R) the rotating sample holder, (B) the beam-stop, (D) the rotating 2θ detector, and (N) the incident x-ray collimator.

3.1.1 High-Pressure Synchrotron X-ray Diffraction

For measurements which require higher precision or higher x-ray intensities, synchrotron radiation is used. Synchrotron radiation facilities accelerate electrons radially causing them to emit electromagnetic radiation over a broad spectrum at a very high flux. In this thesis work, monochromatic high intensity synchrotron radiation was used to measure x-ray diffraction on single-crystal samples mounted in high-pressure diamond anvil cells. Experiments were performed at the European Synchrotron Radiation Facility (Grenoble, France) on the ID09A beamline.

For the application of pressure, a membrane-driven high-pressure cell following a diamond anvil design was employed. The stainless steel gasket had an initial hole diameter of 250 μm and was pre-indented to a thickness of $\approx$ 80 μm.[69] The samples were loaded into the pressure cell along with high-purity rubies to be used as manometers and He gas as a pressure transmission medium. Pressures were measured using a Ruby fluorescence technique.[70]

Details of the synchrotron diffraction setup are as follows. A monochromatic synchrotron x-ray beam with $\lambda = 0.413$ Å ($E \approx 30$ keV) was focused to a spot size of 15×10 μm^2. X-ray diffraction intensities were collected using a Mar555 flat-panel detector with an ω rotation, an integrated step scan of 0.5^o, and a counting time of 1 second per frame. In order to correct for variable diffracting volumes as a function of the ω position, frames were rescaled using the intensities of Friedel pairs. The collected diffraction data were processed and analyzed using CrysAlisPro-171.34.44, SIR2011, Crystals and Jana2006 software packages.[71–74]

3.2 Magnetic Susceptibility

The magnetization, $\vec{M}$, of a material is defined as the sum of individual magnetic moments, $\vec{\mu_i} = g\mu_B\vec{S_i}$,[1] per unit volume, V.

$$\vec{M} = \frac{g\mu_B}{V}\sum_i \vec{S_i} \tag{3.4}$$

Where g is the g-factor and μ_B is the Bohr magneton. In terms of thermodynamics, the isothermal magnetization is expressed as the first derivative of the Helmholtz free energy, F, with respect to the magnetic field, H.

$$M = -\left(\frac{\partial F}{\partial H}\right)_{T,V} \tag{3.5}$$

The magnetic susceptibility can be expressed as the second derivative of the Helmholtz free energy with respect to field,

$$\chi = -\left(\frac{\partial^2 F}{\partial H^2}\right)_{T,V} = \left(\frac{\partial M}{\partial H}\right)_{T,V} \approx \left(\frac{M}{H}\right)_{T,V} \tag{3.6}$$

In the case when M is linearly related to the H, we can approximate χ to be the ratio of the two. This approximation is used when experimentally measuring the magnetic susceptibility of a material and for this approximation to be valid, an applied magnetic field must be small, $\mu_B H << k_B T$.

Magnetization measurements versus temperature and magnetic field were carried out on a commercial Quantum Design Magnetic Property Measurement System (MPMS). The MPMS uses a Superconducting Quantum Interference Device (S.Q.U.I.D.) to perform very sensitive magnetic measurements.[75] The commercial system allows for measurements in the temperature range of 1.8 to 400 K with the

[1] L has been taken to be 0 here, thus, $J = S$

possible application of a magnetic field up to 7 T. Typically, the sample is mounted in a synthetic quartz tube composed of high purity diamagnetic quartz. The sample is either glued to the center of the tube with a minute amount of diamagnetic fast-drying varnish or, in the case of a powder, the quartz tube is sealed in the middle to enclose the sample. To obtain a correct measurement of the sample magnetization, a background measurement of the quartz tube was performed and subtracted from the data.

The MPMS measures the magnetic response in electromagnetic units, emu, which is the total magnetic moment. It is most convenient to express the data in CGS units in which case emu $\rightarrow$ cm^{3}G and Oe $\rightarrow$ G. The molar susceptibility can then be calculated by

$$\chi_{\mathrm{mol}}(T,H)[\frac{\mathrm{cm}^3}{\mathrm{mol}}] = \frac{\mu(T,H)[\mathrm{cm}^3\mathrm{G}] \times \mathrm{M}_{\mathrm{mol}}[\frac{\mathrm{g}}{\mathrm{mol}}]}{H[\mathrm{G}] \times m[\mathrm{g}]}, \tag{3.7}$$

where $\mu(T,H)$ is the total magnetic moment measured by the MPMS, $\mathrm{M}_{\mathrm{mol}}$ is the Molar mass, H is the applied magnetic field, and m is the mass of the sample. For field dependent measurements, the magnetization per Bohr magneton can be calculated according to

$$M(T,H)[\mu_{\mathrm{B}}] = \frac{\mu(T,H)[\mathrm{cm}^3\mathrm{G}] \times \mathrm{M}_{\mathrm{mol}}[\frac{\mathrm{g}}{\mathrm{mol}}]}{\mu_{\mathrm{B}}[\mathrm{cm}^3\mathrm{G}] \times \mathrm{N}_{\mathrm{A}}[\frac{1}{\mathrm{mol}}] \times m[\mathrm{g}]} \tag{3.8}$$

where N_{A} is Avogadro's number.

3.2.1 MPMS Extensions

Magnetic measurements under hydrostatic pressure were performed using a home-built copper:beryllium (98%:2%) alloy cell, following the design of Refs. [76] and [77]. The pressure cell, shown in Figure 3.2, was designed to be compatible with the MPMS system. The cell applies hydrostatic pressure up to $\approx$ 7 GPa with ceramic anvils and up to $\approx$ 10 GPa with diamond anvils. The maximum pressure also depends

on the anvil cutlet size. The cell uses a copper:beryllium gasket, ≈ 0.4 mm thick, as a sample holder providing a sample space of ≈ 0.03 mm^3, see Figure 3.3. In addition to the sample, the sample space is filled with silicon oil to act as a pressure transmitting medium and a high purity (99.999%) Pb sphere to act as a manometer. The applied pressure was determined from the superconducting critical temperature of the Pb sphere.[78, 79] Two anvils, composed of either diamagnetic ceramic or diamond, compress the sample gasket from either side to provide the pressure. Two outer screw clamps are tightened to maintain the pressure in the cell.

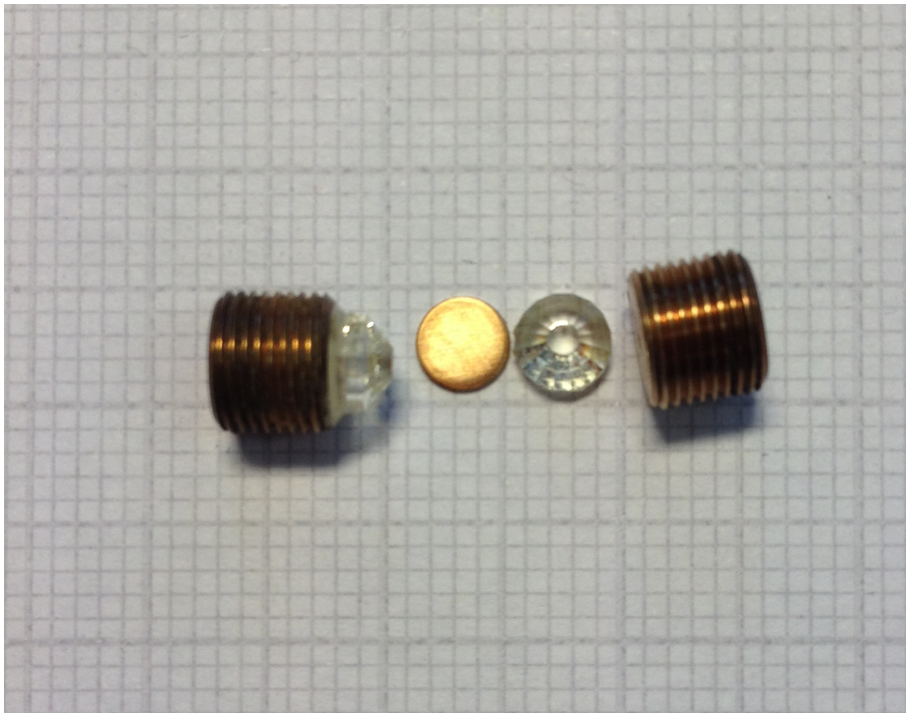

Figure 3.2: **MPMS Pressure Cell.** A diamond anvil pressure cell compatible with the MPMS measurement system. The cell is used in hydrostatic pressure measurements of magnetic susceptibility and magnetization. The image displays the outer Cu:Be screw clamps, the diamond anvils, and the Cu:Be gasket to be used as a sample holder.

To reach temperatures below 1.8 K (the base temperature of the commercial system), a home-built single-shot ^{3}He cooling system was inserted into the inner MPMS

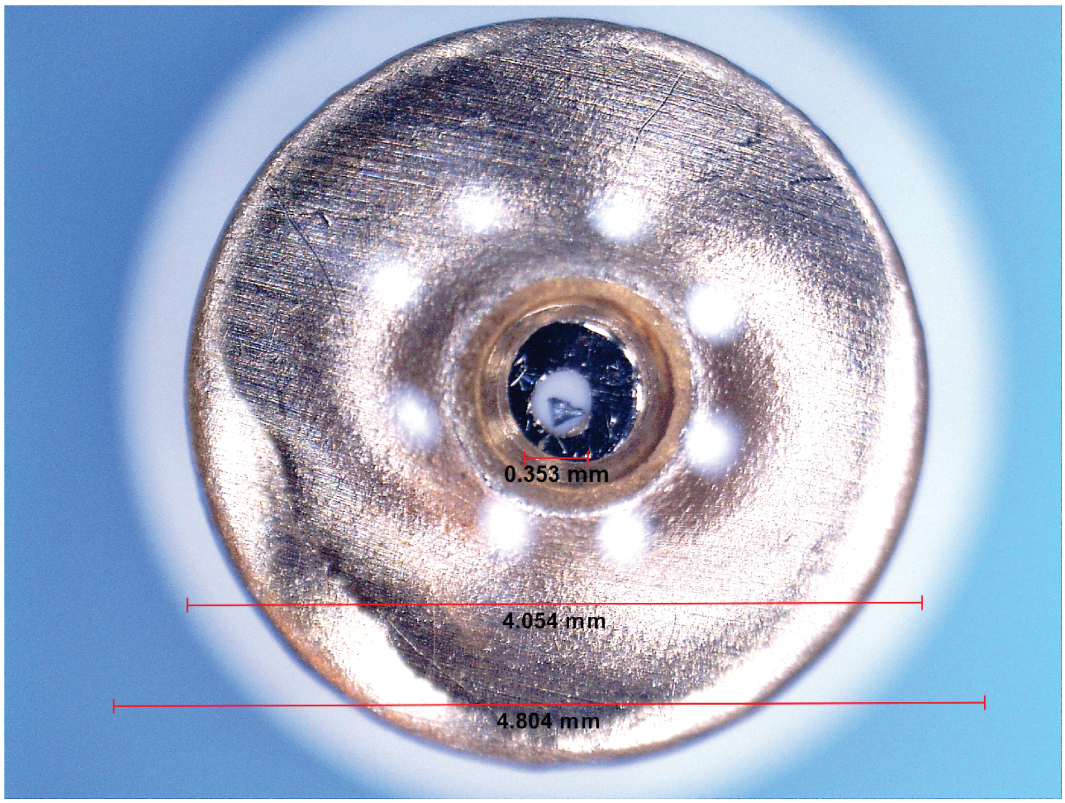

Figure 3.3: **Pressure Cell Gasket.** The pre-indented Cu98:Be2 gasket resting on a white ceramic anvil used in the MPMS compatible pressure cell. Diameters listed from top to bottom are the sample space (0.353 mm), the gasket (4.054 mm), and the ceramic anvil (4.804 mm). A (gray) piece of high-purity lead is located inside the sample space.

chamber.[80] The ^{3}He cooling system contains a mini cryostat which replaces the general MPMS sample rod. A flexible outer-shell at the top of the ^{3}He cryostat allows for vertical movements enabling measurements by the MPMS. To operate the cooling system below 1.8 K, ^{3}He gas is filled into the single-shot cryostat and the MPMS system is cooled as normal down to 1.8 K with ^{4}He, this allows for the condensation of the ^{3}He gas. At 1.8 K the ^{3}He is slowly pumped away with an absorption pump causing an evaporation cooling effect inside the cryostat. At $\approx$ 800 mK, a turbo pump is switched on increasing the pumping power and allowing for the system to reach a temperature of $\approx$ 580 mK.

3.3 Heat Capacity

The molar heat capacity of a system is defined as the heat added or removed, δQ (J), to one mole of material, required to change the temperature of the material by dT (K) under constant conditions. Starting with the internal energy at constant volume, $dU = TdS - pdV = \delta Q$:

$$C_V(T) = \left(\frac{\partial U}{\partial T}\right)_V = \left(\frac{\partial Q}{\partial T}\right)_V = T\left(\frac{\partial S}{\partial T}\right)_V = -T\left(\frac{\partial^2 F}{\partial T^2}\right)_V \tag{3.9}$$

Standard heat capacity experiments maintain constant pressure, p, and not constant volume. C_p is related to the Gibbs Free energy G and the change of enthalpy, $d\mathcal{H} = T(dS) - V(dp) = \delta Q$:

$$C_p(T) = \left(\frac{\partial \mathcal{H}}{\partial T}\right)_p = \left(\frac{\partial Q}{dT}\right)_p = T\left(\frac{\partial S}{\partial T}\right)_p = -T\left(\frac{\partial^2 G}{\partial T^2}\right)_p \tag{3.10}$$

In a first approximation, the heat capacities at constant volume and at constant

pressure are related by:

$$C_p(T) \approx C_V(T) + \frac{VT\alpha^2(T)}{\kappa_T} \tag{3.11}$$

where $\alpha(T)$ is the volumetric coefficient of thermal expansion and κ_T is the isothermal compressibility. However, for solids at sufficiently low temperatures $C_p \approx C_V$ is a very good approximation since typically $\alpha(T) \sim 10^{-6}$ K^{-1}.

Low temperature heat capacity measurements are particularly insightful towards the phonon, magnetic and electronic behaviours of a material. In many cases, the $T \to 0$ heat capacity can be expressed as a summation of contributions from the conduction electrons, phonons, and magnons (for magnetically ordered compounds):

$$C_p(T) = C_{\text{Electronic}} + C_{\text{Phonon}} + C_{\text{Magnetic}} = \gamma T + bT^3 + cT^{\frac{d}{n}} \tag{3.12}$$

Furthermore, in insulating systems, the Sommerfeld electronic contribution term can be ignored, $\gamma \approx 0$. For magnetic systems, d represents the dimensionality of the crystal lattice and n is the exponent of the wave vector $\vec{k}$ in the magnetic dispersion relation $\omega(k)$. For a FM compound $\frac{d}{n} = \frac{3}{2}$ and for an AFM compound, $\frac{d}{n} = \frac{3}{1}$.

As $T \to \infty$, the heat capacity approaches the temperature independent Dulong-Petit law, $C_{\text{V}} = 3\text{NR}$, where N is the number of moles and R is the molar gas constant.

Heat capacity measurements were performed in a commercial Quantum Design Physical Properties Measurement calorimeter System (PPMS). The system calculates the heat capacity using a relaxation method and allows for measurements in the temperature range of 0.3 K to 400 K with a magnetic field up to 9 T.[81] A commercial ^{3}He extension, similar to that of the MPMS, was used to reach temperatures down to 300 mK. Samples were thermally anchored to the calorimeter platform using a minute amount of Apiezon N grease. The heat capacity of the sample platform with grease was determined in a preceding run and subtracted from the total heat capacity

measurements. The PPMS measured heat capacity, C_m, can be normalized according to:

$$C_p(T,H)[\frac{\mathrm{J}}{\mathrm{molK}}] = C_m(T,H)[\frac{\mu\mathrm{J}}{\mathrm{K}}] \times \frac{\mathrm{M_{mol}}[\frac{\mathrm{g}}{\mathrm{mol}}]}{m[\mathrm{g}]} \times 10^{-6}[\frac{\mathrm{J}}{\mu\mathrm{J}}] \tag{3.13}$$

3.4 Electron Paramagnetic Resonance

Electron paramagnetic resonance (EPR) is a useful spectroscopy technique for investigating systems with unpaired spins. The measurement works by splitting the energy levels of a free electron using a magnetic field (Zeeman splitting) while exposing the sample to electromagnetic radiation perpendicular to the external field. The energy of a free electron in a magnetic field is:

$$E = g\mu_B m_s H \tag{3.14}$$

with $m_s = \frac{1}{2}$,$-\frac{1}{2}$. In a typical EPR spectrometer, the magnetic field is increased continuously until the resonance condition is reached, the applied field which satisfies the resonance condition is called the resonance field, H_{res}. At this point, the free electron will absorb (or emit) a quantum of energy, $h\nu$, and move to the higher (or lower) energy level. The resonance condition can be described by the following equation:

$$h\nu = g\mu_B \Delta m_s H_{\mathrm{res}} \tag{3.15}$$

From this equation, the g-factor of the system can be determined. The g-factor of a magnetic ($3d$) system contains information about its spin and angular momentum. The g-factor is a very useful characteristic parameter in spin-chain systems which, for example, can assist with fitting the magnetic susceptibility data.

EPR measurements were carried out using a Bruker ER040XK X-band microwave

spectrometer with a Bruker BE25 magnet and a BH15 field controller calibrated with Diphenylpicrylhydrazyl (DPPH). The measured spectra were collected with a microwave radiation of ≈ 9.48 GHz in a temperature range of 2.5 K to 300 K. The EPR spectra were well modeled by a field derivative of a Lorentzian absorption resonance line with a linewidth ΔH. It was found necessary to take the resonances $\pm\omega$ into account when the linewidth became comparable to the resonance field, $\Delta H \sim H_{\rm res}$. The equation used to fit the spectra is as follows

$$\frac{dP_{\rm abs}}{dH} \propto \frac{d}{dH}\left(\frac{\Delta H + \zeta(H - H_{\rm res})}{(H - H_{\rm res})^2 + \Delta H^2} + \frac{\Delta H + \zeta(H + H_{\rm res})}{(H + H_{\rm res})^2 + \Delta H^2}\right), \tag{3.16}$$

where $P_{\rm abs}$ is the absorbed microwave power, ΔH is the half-width at half-maximum (HWHM), $H_{\rm res}$ is the resonance field, and ζ measures the degree of admixture of dispersion to the signal. Additionally, a background offset and a linear variation of the background signal with the field were taken into account for the fits. From an individual spectrum, the g-factor can be conveniently calculated using the experimental parameters with the equation

$$g = \frac{0.71449[\frac{\rm G}{\rm MHz}] \times \nu[\rm MHz]}{H_{\rm res}[\rm G]} \tag{3.17}$$

where $0.71449[\frac{\rm G}{\rm MHz}] = h/\mu_{\rm B}[\frac{\rm T}{\rm Hz}] \times 10^6[\frac{\rm Hz}{\rm MHz}] \times 10^4[\frac{\rm G}{\rm T}]$, and h is Planck's constant.

3.5 Raman Spectroscopy

Raman spectroscopy is a sensitive measurement technique which can monitor inelastic optical photon scattering from a sample. This measurement can be very useful to identify crystal structure transformations. Photon scattering creates high frequency excitations within the sample such as phonons (vibrational modes). Raman

scattering corresponds to the creation of a phonon (Stokes scattering) or absorption of a phonon (anti-Stokes scattering). The shift in the wavelength between the incident and reflected laser light is called the Raman shift, in wavenumbers, and can be calculated by:

$$\Delta k[\mathrm{cm}^{-1}] = \left(\frac{1}{\lambda_i[\mathrm{nm}]} - \frac{1}{\lambda_f[\mathrm{nm}]} \right) \times 10^7 \left[\frac{\mathrm{nm}}{\mathrm{cm}} \right] \tag{3.18}$$

where λ_i, λ_f are the incident and reflected wavelengths of the laser light. Raman spectroscopy is particularly useful when searching for temperature or pressure induced structural phase changes. The crystal lattice symmetry determines the number of Raman active modes. A structural transition resulting in a change of the lattice symmetry will also alter the Raman active modes.

Raman spectra were measured with a Jobin Yvon Typ V 010 LabRAM single grating spectrometer with ≈ 1 cm^{-1} spectral resolution. The spectrometer setup was equipped with a double super razor edge filter, Peltier cooled CCD camera and a Mikrocryo cryostat with a copper cold finger. Measurements were performed with linearly polarized He/Ne gas laser light of 632.817 nm with < 1 mW of power. The light beam was focused to a 10 μm spot on the top surface of the sample using a microscope. Measurements were taken in temperatures ranging between 4 K and 325 K.

A diamond anvil cell, shown in Figure 3.4, was used to measure Raman spectra with the application of hydrostatic pressure. The pressure cell uses two diamond anvils to compress a copper:beryllium gasket used as a sample holder, similar to that described above (Figure 3.3). An ethanol-methanol pressure transmitting medium was filled into the sample space along with rubies to be used as manometers. Pressures were measured with the Ruby fluorescence method following a nonlinear hydrostatic

calibration.[82]

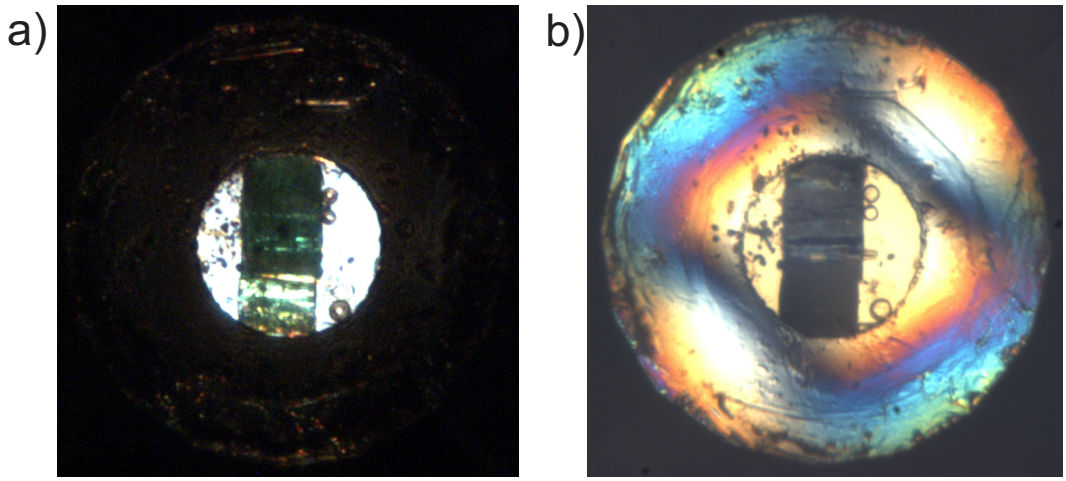

Figure 3.4: **Diamond Anvil Cell.** A diamond anvil cell used in hydrostatic pressure measurements. The cell is loaded with a sample (green) and three rubies (white spheres) at a) ambient pressure and b) $\approx$ 20 GPa.

3.6 Neutron Diffraction

Neutron diffraction experiments were carried out for the characterization of magnetic structures. Neutron diffraction follows the same principals as x-ray diffraction (Eq. 3.1), however, the neutrons are largely scattered off the nuclei of a sample rather than the electrons. Neutrons carry a spin S=1/2, and are electrically neutral, therefore neutrons can interact with the magnetic moments of unpaired electrons. Because of this, neutron scattering can be used to determine magnetic structures in magnetically ordered systems.

For the characterization of a magnetic structure, neutron diffraction must be performed on a magnetically ordered sample ($T < T_C$). At the low angular parts of the diffraction patterns, magnetic Bragg reflections can be observed in addition to the nuclear reflections. For weak magnetic moments, it is advantageous to subtract away the nuclear reflections with a diffraction pattern collected for a temperature

above the magnetic ordering temperature and extract a magnetic diffraction pattern. Difficulties arise when dealing with magnetic scattering due to the weak scattering amplitude which can become lost in the stronger nuclear scattering. The intensity of the magnetic scattering is proportional to the magnetic moment of the magnetic ion squared ($\propto \mu^2$), this becomes a serious issue when dealing with weak $S = 1/2$ magnetic moments such as Cu^{2+} moments.

For coherent elastic scattering, the nuclear differential cross section for N cells of volume V_0 can be expressed as:

$$\left(\frac{d\sigma}{d\Omega}\right)_{\text{Nuc}} = N\frac{(2\pi)^3}{V_0}\sum_{\boldsymbol{G}}\delta(\boldsymbol{Q}-\boldsymbol{G})|F_{\text{N}}(\boldsymbol{G})|^2 \tag{3.19}$$

where $\boldsymbol{G}$ is a reciprocal lattice vector, $F_{\text{N}}(\boldsymbol{G})$ is the nuclear structure factor, and $\boldsymbol{Q} = \boldsymbol{k}_{\text{f}} - \boldsymbol{k}_{\text{i}}$ is the scattering vector which can be derived from Bragg's Law as:

$$Q = \frac{4\pi\sin(\theta)}{\lambda} = \Delta k \tag{3.20}$$

For magnetic coherent elastic scattering, the magnetic differential cross section for N_m cells of volume V_m can be expressed as:

$$\left(\frac{d\sigma}{d\Omega}\right)_{\text{Mag}} = N_m\frac{(2\pi)^3}{V_m}\sum_{\boldsymbol{G}}\delta(\boldsymbol{Q}-\boldsymbol{G})|F_{\text{M}}(\boldsymbol{G})|^2 \tag{3.21}$$

where $F_{\text{M}}(\boldsymbol{G})$ is the magnetic structure factor. $|F_{\text{M}}(\boldsymbol{G})|^2$ is proportional to $\boldsymbol{Q}\times\boldsymbol{\rho}_{\text{m}}$, where $\boldsymbol{\rho}_{\text{m}}$ is the magnetization density so only the component of the magnetic moment perpendicular to the scattering vector contributes to magnetic scattering.

Elastic neutron powder diffraction experiments were carried out at the Institute Laue-Langevin (Grenoble, France). Diffraction patterns were collected on the high-intensity two-axis diffractometer D20 with a wavelength $\lambda = 2.41$ Å, see Figure 3.5.[83]

A closed-cycle ^{3}He system was used to reach temperatures down to 432 mK.

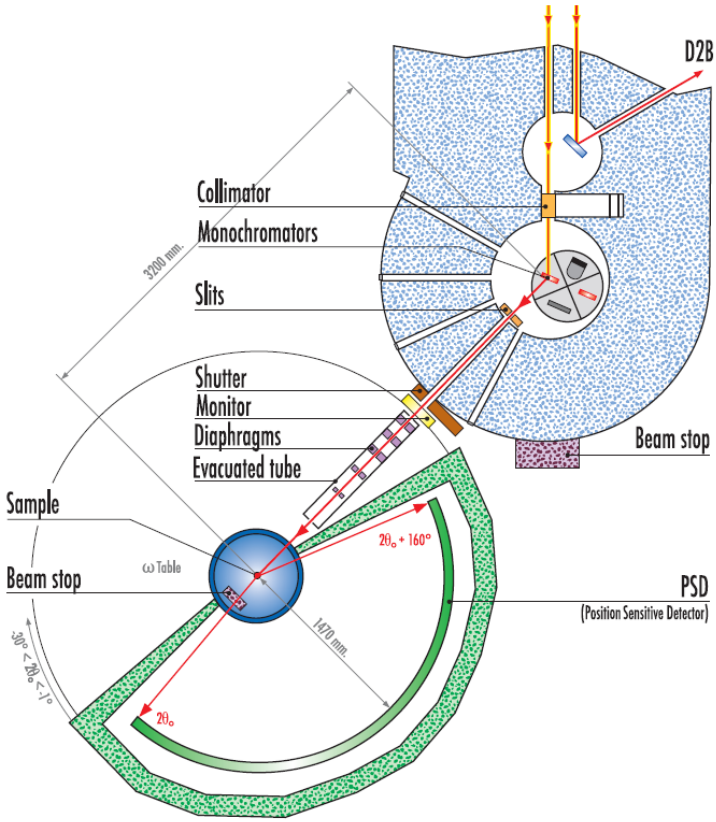

Figure 3.5: **D20 Diffractometer.** A schematic diagram of the high-intensity two-axis powder diffractometer D20 at Institute Laue-Langevin in Grenoble, France. Figure reprinted from Ref. [83] with permission.

3.7 Dielectric Capacitance

Dielectric capacitance measurements were performed to characterize the dielectric properties of materials. A powder capacitance cell was utilized to measure the dielectric capacitance of a powder sample, see Figure 3.6. The powder cell compacts the sample powder between two metal plates to form the dielectric of a two-plate capacitor. The powder cell connects to a measurement probe and used together with a low-temperature cryostat. Shielded coaxial cables connect the capacitance powder

cell to an ultra-precision Andeen-Hagerling commercial capacitance bridge (model AH2700). The instrument applies an oscillating voltage across the capacitor and analyses the response in terms of an electric circuit model.[84]

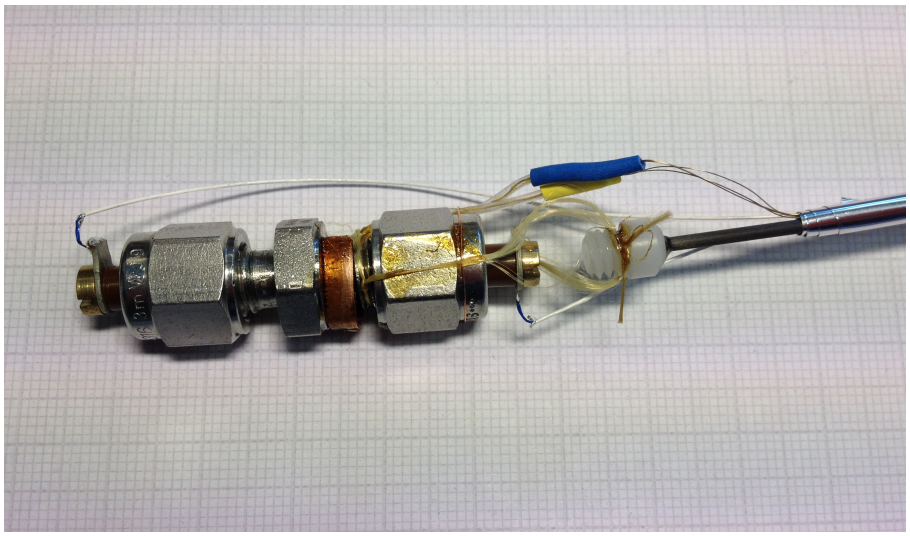

Figure 3.6: **Powder Capacitance Cell.** A powder capacitance cell used to characterize the dielectric properties of a powder sample. The cell compresses the sample powder between two metal plates to form the dielectric of a capacitor.

The capacitance of the powder capacitor cell as a function of frequency ω, magnetic field and temperature is measured according to:

$$C(\omega, H, T) = \epsilon_r(\omega, H, T)\epsilon_0 A/d \tag{3.22}$$

where $\epsilon_r(\omega, H, T)$ is the relative permittivity or the dielectric constant, ϵ_0 is the permittivity of free space, A is the capacitor plate area, and d is the distance between the two capacitor plates (sample thickness). The dielectric constant as a function of frequency, magnetic field, and temperature can be determined from the measured capacitance using:

$$\epsilon_r(\omega, H, T) = k \times C(\omega, H, T) \tag{3.23}$$

where k is the geometric factor, $k = d/A\epsilon_0$. For the capacitance powder cell, $k \approx 40$ F^{-1}.

4

Copper Arsenite - $CuAs_2O_4$

The contents of this chapter are reproduced with permission from the American Physical Society and have been previously published in Ref. [67]: "Characterization of the spin-$\frac{1}{2}$ linear-chain ferromagnet $CuAs_2O_4$" K. Caslin, R. K. Kremer, F. S. Razavi, A. Schulz, A. Muñoz, F. Pertlik, J. Liu, M.-H. Whangbo, and J. M. Law, Physical Review B **89**, 014412 (2014).

This chapter is dedicated to the structural and magnetic characterization of $CuAs_2O_4$, a S=1/2 quantum spin-chain ferromagnet. No previous study on the magnetic properties of $CuAs_2O_4$ has been reported. The decision to investigate this compound was based on an x-ray diffraction study performed by J. Zeeman in 1951 which revealed a crystal structure which could support low-dimensional magnetism.[85] $CuAs_2O_4$ is structurally characterized by CuO_2 ribbon-chains which are located in CuO_6 Jahn-Teller distorted octahedra. $CuAs_2O_4$ is particularly interesting because it exhibits competing NN and NNN intrachain interactions with $\alpha = J_{\mathrm{nn}}/J_{\mathrm{nnn}} \approx$ -4.1. Consequently, $CuAs_2O_4$ represents a rare example of a magnetically frustrated spin-chain system in close proximity to the quantum critical limit at α = -4 where Highly Frustrated and FM groundstates meet in the phase diagram (Figure 2.7). In this chapter, I will report on the structural properties using results from x-ray diffraction and Raman Scattering measurements. I characterize the bulk magnetic properties

with magnetic susceptibility, heat capacity and electron paramagnetic resonance results. Additionally, I use single-crystal magnetization data to investigate directional dependent magnetic behaviour. Density functional theory and transfer matrix renormalization group calculations with collaborators are used to support my experimental findings.

4.1 Sample Characterization

$CuAs_2O_4$ single-crystals of ≈ 0.15 mm^3 in size were grown using a hydrothermal synthesis route. Precursor powders of As_2O_3 and CuO were mixed in a 1:1 ratio and filled into a teflon lined autoclave along with acetic acid. The autoclave was heated to 200°C at $\approx$ 15 bar for 3 days. More details on the single-crystal preparation can be found in Refs. [86] and [87]. Figure 4.1a displays the (hkl) faces of one crystal oriented using single-crystal x-ray diffraction and Figure 4.1b displays the typical crystal size measured using scanning electron microscopy.

X-ray powder diffraction measurements, shown in Figure 4.2, were carried out to evaluate the sample quality and characterize the crystal structure. The measurement was performed with Mo $K\alpha_1$ radiation ($\lambda = 0.70930$ Å) on a polycrytalline sample which was prepared by thoroughly grinding crystals into a powder. The sample holder was a 0.3 mm diameter, $\approx$ 4cm long, quartz capillary. A two-phase Rietveld fit to the x-ray diffraction pattern, also shown in Figure 4.2 as a solid black line, was calculated using FullProf Suite software.[68] The refined cell parameters and atom positions, see Table 6.1, were in very good agreement with the previously reported values by J. Zemann.[85] The green dashes in Figure 4.2 represent the Brag positions of both phases and the blue line represents a difference between the calculated and measured patterns. From the Rietveld refinement, an impurity phase of diamagnetic

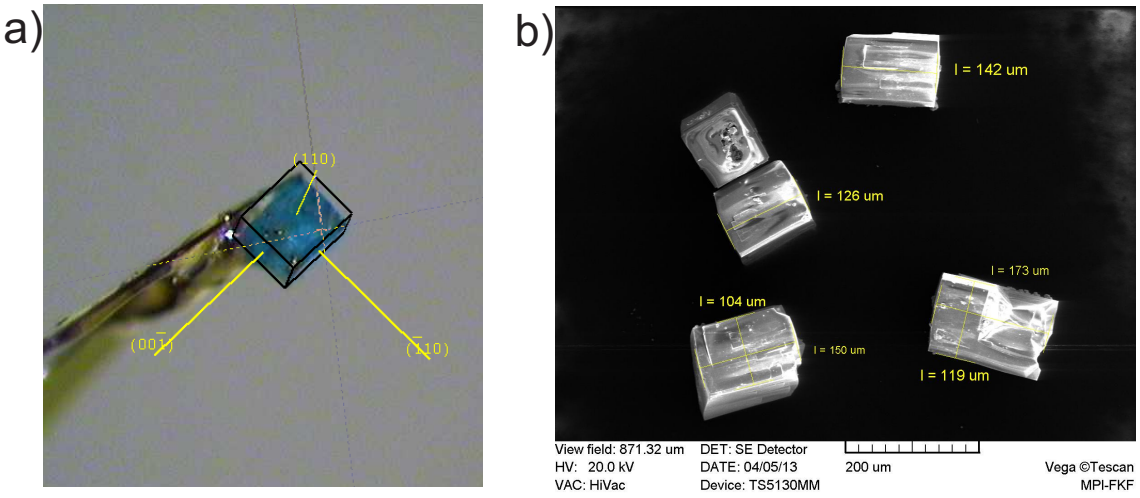

Figure 4.1: **$CuAs_2O_4$ Samples.** (a) A single-crystal of $CuAs_2O_4$ with labeled (hkl) faces, oriented using an image-plate detector. (b) An energy-dispersive x-ray spectroscopy (EDX) image of five $CuAs_2O_4$ single-crystals depicting the approximate size of the samples.

Cu_2O (Cuprite) amounts to $\approx 5\%$ of the sample. The brownish impurity could be seen under microscopic inspection of the crystals and those crystals which where free of visible impurities where selected to be studied.

Table 4.1: **$CuAs_2O_4$ Refined Structural Parameters.** Refined positional parameters of $CuAs_2O_4$ from a two-phase Rietveld refinement of x-ray diffraction data. The tabulated parameters for were refined in space group $P4_2/mbc$ (no. 135) with lattice parameters $a = 8.58(1)$ Å and $c = 5.54(1)$ Å. The agreement indicies for $CuAs_2O_4$ were Bragg R-factor = 8.86 and RF-factor = 5.90. The agreement indicies for Cu_2O were Bragg R-factor = 1.83 and RF-factor = 11.5. The global index $\chi^2 = 0.00153$.

Atom:Wyck.	As:8h	Cu:4d	O(2):8h	O(1):8g
Site symm.	m..	2.22	m..	..2
x/a	0.2003(3)	0	0.101(1)	0.704(1)
y/b	0.1604(3)	1/2	0.630(1)	0.204(1)
z/c	0	1/4	0	0.25

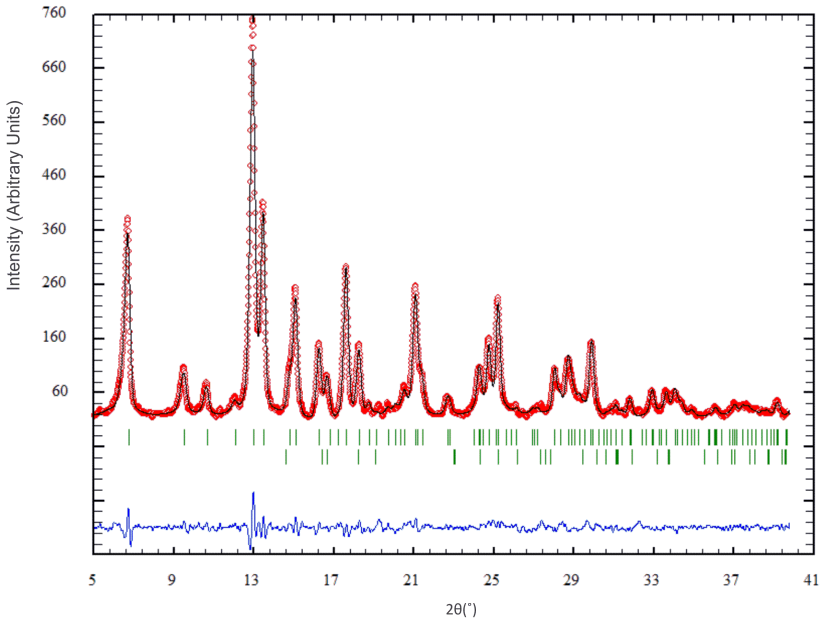

Figure 4.2: **$CuAs_2O_4$ X-ray Diffraction.** A Mo $K_{\alpha 1}$ x-ray diffraction pattern of a $CuAs_2O_4$ polycrystalline sample (red circles). The two-phase Rietveld fit (black line) to the pattern was calculated using FullProf Suite software. The first phase (upper green lines) is the main sample, $CuAs_2O_4$, and the second impurity phase (lower green lines) is Cu_2O. The impurity phase amounts to $\approx 5\%$ from the fit calculation. The difference between the measured pattern and calculated fit is shown as the blue line.

4.2 Crystal Structrure

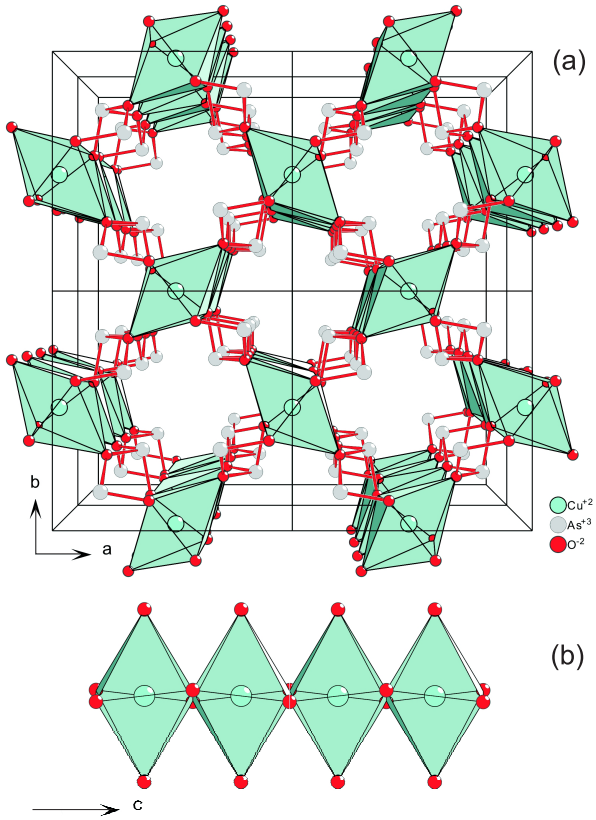

Figure 4.3: **$CuAs_2O_4$ Crystal Structure.** (a) Projection along the [001] direction of the $CuAs_2O_4$ crystal structure. The Cu^{2+} atoms are represented by the large (green) spheres, the oxygen atoms by small (red) spheres, and the As atoms by (grey) medium spheres. (b) A corrugated chain of trans-edge connected CuO_6 octahedra highlighting the twisted basal planes of the octahedra in $CuAs_2O_4$, which lead to a corrugation of the CuO_2 ribbon chains.

$CuAs_2O_4$ crystallizes in a tetragonal structure (space group $P4_2/mbc$) with lattice parameters $a = b = 8.592(4)$ Å and $c = 5.573(4)$ Å.[86] The Cu atoms are located on Wyckoff sites $4d$ and the As atoms on sites $8h$. The O atoms occupy Wyckoff sites $8g$(O1) and $8h$(O2). As shown in Figure 4.3, the Cu atoms are centered in Jahn-Teller elongated O_6 octahedra (Cu - O distances: 4×1.95 Å; 2×2.47 Å).

These CuO_6 octahedra connect via opposite edges to form CuO_2 ribbon-chains in their basal-planes. The O(1) and O(2) atoms are located at the apical and basal positions of the octahedra, respectively. The As atoms form AsO_3 pyramids, which link the oxygen atoms in the basal planes with the apical oxygen atoms of neighboring chains such that the basal planes of neighboring chains are perpendicular to each other.[86] The $4s^2$ electrons of the As atoms act as pseudo-ligands and extend into the channels enclosed by four neighboring chains.[88]

4.3 Lattice Properties

To gain insight on the lattice properties of $CuAs_2O_4$, Density Functional Theory (DFT) calculations with a generalized gradient approximation (GGA) and DFT calculations with a local density approximation (LDA) were performed by collaborator A. Muñoz of Universidad de La Laguna (Tenerife, Spain) for the hypothetical diamagnetic compound $ZnAs_2O_4$. For details on the DFT calculations refer to Ref. [67]. Since the masses and ionic radii of Cu^{2+} and Zn^{2+} are similar, the calculations for $ZnAs_2O_4$ were compared to the Raman spectroscopy and heat capacity measurements performed on $CuAs_2O_4$. Replacing the magnetic Cu^{2+} ion with a diamagnetic Zn^{2+} ion provides information on the phonon contribution to the specific heat of $CuAs_2O_4$ and disregards any magnetic contributions. Figure 4.4 displays the total and partial phonon densities of states for the hypothetical compound $ZnAs_2O_4$. The calculated Raman frequencies with their assigned symmetries are listed in Table 4.2 in comparison to experimental observations of $CuAs_2O_4$.

As displayed in Figure 4.4, the phonon spectrum of $ZnAs_2O_4$ is characterized by a set of rather sharp bands indicating nearly localized lattice vibrations extending up to 800 cm^{-1}. The set of phonon bands decomposes into three subgroups, one

group below ≈ 300 cm^{-1}, corresponding mainly to Zn and As vibrations with little contribution from O vibrations. The remaining two subgroups are found above ≈ 300 cm^{-1} and correspond mainly to O vibrations with almost no contribution from the heavier Zn and As atoms. The high frequency vibrations were dominated by the O(2) atoms of the basal planes of the distorted octahedra. For the purpose of fitting the phonon contribution to the heat capacity data (see below), the total phonon spectrum can be roughly described by two major groups of phonon modes centered at ≈ 150 cm^{-1} (≈ 220 K) and ≈ 500 cm^{-1} (≈ 720 K).

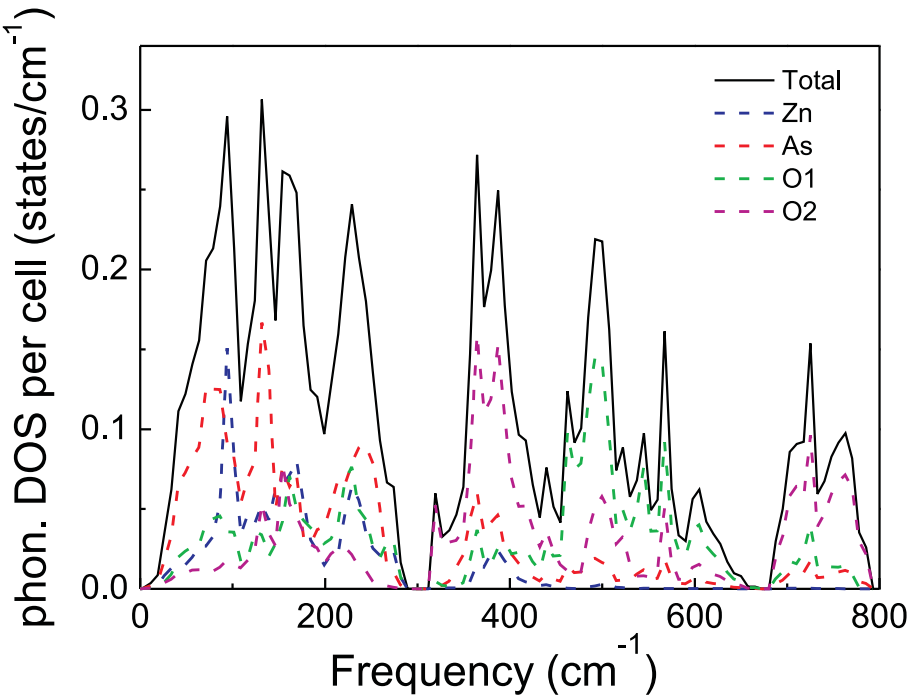

Figure 4.4: **$ZnAs_2O_4$ Phonon D.O.S.** Total and partial phonon densities of states of a hypothetical compound $ZnAs_2O_4$ per unit cell.

4.4 Raman Scattering

Raman spectra of $CuAs_2O_4$ with light polarized along the crystallographic *c*-axis were measured for various temperatures between 4 K and 325 K, see Figure 4.5. The measured spectra are similar to that previously measured at room temperature by S. Kharbish with the exception of two additional peaks.[89] Table 4.2 lists the Raman mode positions in comparison with data from S. Kharbish. The peak positions and symmetry assignments according to the DFT-GGA and -LDA calculations are also listed.

The measured spectra show that there are no temperature induced peak splittings indicating that the crystal symmetry, and therefore crystal structure, remains unchanged down to 4 K. Overall there is a slight increase in energies as the temperature is decreased reflecting the thermal lattice contraction, see Figure 4.5 inset. Peaks with wavenumbers 403, 763, and 812 cm^{-1} (marked by arrows in Figure 4.5) become narrower and better resolved with decreasing temperature.

4.5 Spin-Exchange Interactions

An energy-mapping analysis [90, 91] based on first principles DFT calculations has been performed by collaborators M. Whangbo and J. Liu of North Carolina State University. These calculations include spin-orbit coupling and calculate the absolute energies for a number of magnetic configurations such that an adequate set of spin-exchange parameters can be derived. The NN and NNN intrachain spin-exchange interactions, J_{nn} and J_{nnn}, of $CuAs_2O_4$ were evaluated for the three ordered spin states depicted in Figure 4.6. The energies of the three order states can be written

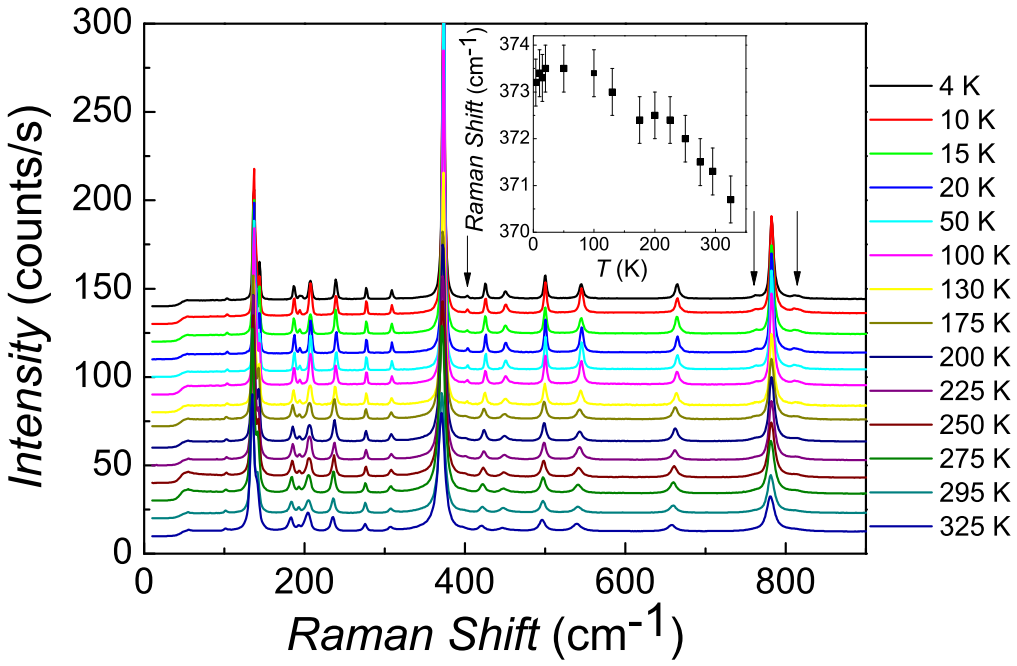

Figure 4.5: **$CuAs_2O_4$ Raman Spectra.** Raman spectra of $CuAs_2O_4$ at various temperatures as indicated. The spectra have been shifted for clarity. The inset shows a typical down shift with increasing temperature of the 371.3 cm^{-1} peak, attributed to lattice expansion.

Table 4.2: **$CuAs_2O_4$ Raman Active Modes.** Comparison of the Raman peak positions with those found by S. Kharbish[89] and those obtained from DFT calculations. The notation n.o. indicates a peak which was not observed. The E_g mode at 101.8 cm^{-1} and B_{1g} mode at 307.9 cm^{-1} were not seen by S. Kharbish.[89]

Symmetry (GGA-LDA)	295 K (cm^{-1})	Kharbish(RT)[89] (cm^{-1})	GGA (cm^{-1})	LDA (cm^{-1})
B_{1g}	n.o.	n.o.	23.2	28.9
E_g	n.o.	n.o.	32.5	35.3
E_g	n.o.	n.o.	98.9	105.3
E_g	101.8	n.o.	103.9	107.9
A_{1g}	n.o.	n.o.	123.6	128.6
B_{2g}	134.9	136	127.2	136.5
B_{1g}	141.1	140	128.1	135.3
E_g	183.6	184	174.9	179.4
A_{1g}	192.8	194	179.9	186.8
B_{2g}	204.7	205	194.5	204.3
B_{1g}	235.8	236	219.8	224.2
E_g	275.7	277	255.1	264.0
B_{1g}	307.9	n.o.	281.0	286.3
A_{1g}	n.o.	n.o.	364.3	370.9
E_g	371.3	372	374.6	381.4
B_{2g}	400.4	398	388.4	401.7
B_{1g}	421.8	423	410.7	419.0
E_g	448.1	448	439.9	449.1
A_{1g}	n.o.	n.o.	477.4	481.3
E_g	497.3	498	496.4	511.8
B_{2g}	n.o.	n.o.	509.9	514.2
E_g	540.8	541	535.4	549.0
B_{1g}	659.5	659	625.6	644.7
A_{1g}	758.5	768	722.8	733.9
B_{1g}	781.5	782	731.9	743.2
B_{2g}	806.4	812	735.3	742.2

in terms of the Heisenberg spin Hamiltonian:

$$\mathcal{H} = -\sum J_{\mathrm{ij}} \vec{S}_{\mathrm{i}} \vec{S}_{\mathrm{j}}, \tag{4.1}$$

where J_{ij} are the exchange parameters for the coupling between spin sites i and j. According to the energy expressions for spin dimers with N=1 unpaired spins per spin site [92, 93], the total spin-exchange energies of the three ordered spin states per eight formula units (FUs) are expressed, see Figure 4.6.

For further details on the DFT calculations of the spin-exchange parameters refer to Ref. [67]. The absolute energies of the three ordered spin states were calculated by employing the projected augmented-wave (PAW) method [94, 95] encoded in the Vienna *ab initio* simulation package (VASP) [96] and the GGA approximation for the exchange and correlation functional.[97] The plane-wave cut-off energy was set to 400 eV and a set of 18 k-points for the irreducible Brillouin zone was used. To probe the effect of electron correlations associated with the Cu 3d state, DFT plus on-site repulsion (DFT+U_{eff}) calculations were performed with U_{eff} = 0, 4, 6 and 8 eV.[98] By mapping the relative energies of the three ordered spin states obtained from the DFT+U_{eff} calculations onto the corresponding Heisenberg Hamiltonian (Eq. (4.1)), the values of the nearest- and next-nearest neighbour spin-exchange parameters, J_{nn} ($\equiv J_1$) and J_{nnn} ($\equiv J_2$), were obtained.

The results of the DFT calculations are summarized in Table 5.2. The NN spin-exchange is found to be FM and dominant while the NNN spin-exchange is found to be AFM. This implies that the system is magnetically frustrated with competing NN and NNN interactions. The Curie-Weiss temperatures listed in Table 5.2 were

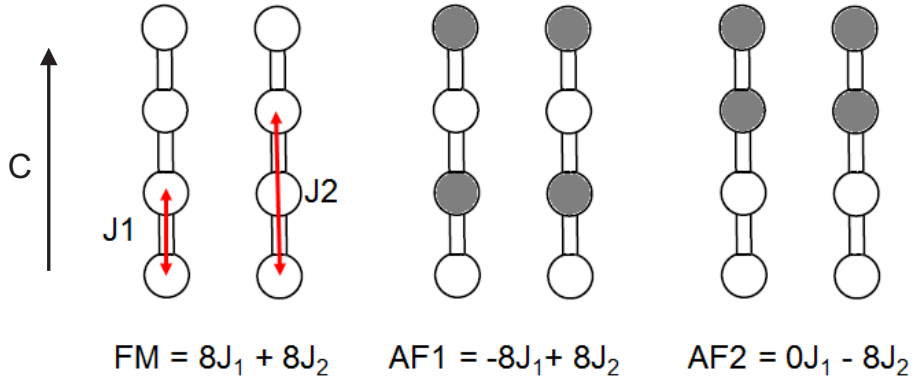

Figure 4.6: **Spin Configurations for DFT Calculations.** Three order spin states of $CuAs_2O_4$ used to determine the values of J_{nn} ($\equiv J_1$) and J_{nnn} ($\equiv J_2$) by DFT+U_{eff} calculations. Only the Cu sites are shown for simplicity. The unfilled and filled circles represent up-spin and down-spin Cu^{2+} sites, respectively.

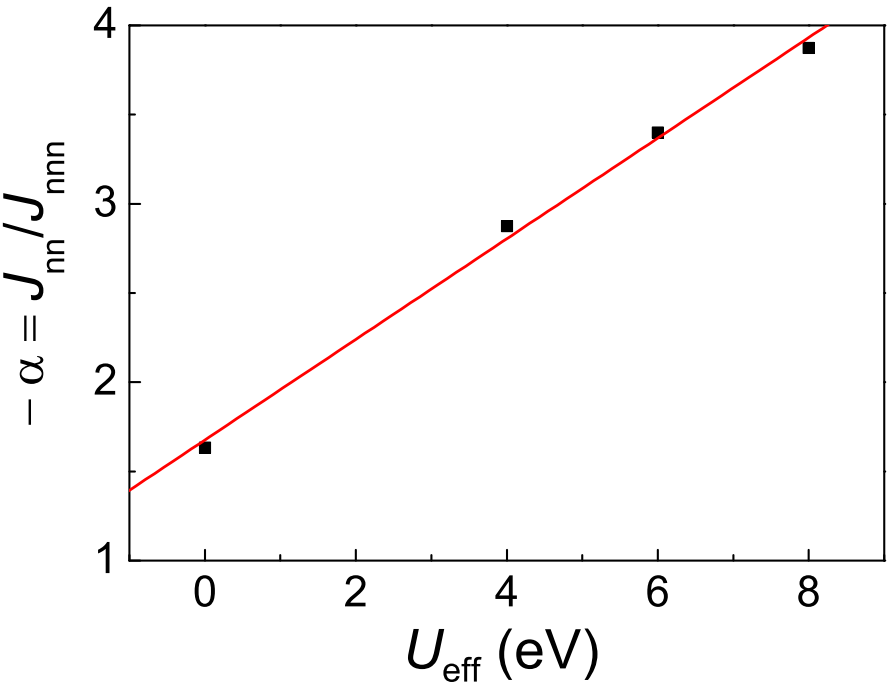

Figure 4.7: **$CuAs_2O_4$ Spin-Exchange Ratio.** The ratio of the NN to NNN spin exchange constants of $CuAs_2O_4$ calculated from the DFT+U_{eff} calculations as a function of U_{eff}.

calculated with the equation,

$$\Theta_{\mathrm{CW}} = \frac{1}{3}S(S+1)\sum_i z_i J_i. \tag{4.2}$$

The J_i's represent the NN and the NNN spin exchange interactions along the ribbon chains, J_{nn} and J_{nnn}, respectively. z_i is the number of neighbors with spin exchange J_i in the NN and NNN shell, $z_{\mathrm{nn}} = z_{\mathrm{nnn}} = 2$ for $CuAs_2O_4$. The calculated Curie-Weiss temperatures are positive as a result of the predominant FM-NN spin-exchange interaction. The U_{eff} values of 6 and 8 eV, most appropriate for Cu^{2+},[38, 98] indicate -3.9 $< \alpha <$ -3.4 (see Figure 4.7), close to the FM-Frustrated quantum critical limit at α_{FM} = -4 (Figure 2.7). Since the $3d_{x^2-y^2}$ magnetic orbitals of neighboring ribbon-chains are largely orthogonal to each other, the interchain spin-exchange interactions are expected to be small and not easily accessible with DFT calculations. An estimation of the interchain interactions can be calculated using an equation for an antiferromagnetic spin-chain system proposed by H. J. Schulz[99] and slightly modified by Rosner *et al.*[100].

$$J_{\mathrm{inter}} \sim T_{\mathrm{N}}\frac{\pi}{2}\left(\ln(5.8 \times J_{\mathrm{nn}}/T_{\mathrm{N}})\right)^{-1/2} \tag{4.3}$$

Despite that $CuAs_2O_4$ orders with a FM groundstate, an estimation of the order of magnitude of the interchain interactions can still be obtained. The calculated interchain interactions are estimated to be $J_{\mathrm{inter}} \sim 5$ K, much smaller than the NN and NNN intrachain interactions.

As shown in Figure 4.7, the ratio of the NN over the NNN spin exchange interactions ($\equiv \alpha$) increases with increasing U_{eff} values used in the DFT+U_{eff} calculations. The strong FM-NN interaction in $CuAs_2O_4$ can be traced back to the fact that the bond angle of the Cu-O-Cu super-exchange path is close to 90° ($\approx 91.5°$, see Figure 2.9) and the magnetic $3d_{x^2-y^2}$ orbital of the Cu^{2+} ion has a large overlap density with

Table 4.3: **$CuAs_2O_4$ Spin-Exchange Parameters.** Values of the NN and NNN spin exchange constants, $J_{\rm nn}$ and $J_{\rm nnn}$, respectively, obtained from the DFT+$U_{\rm eff}$ calculations along with the calculated Curie-Weiss temperatures. (Note: The spin-exchange parameters were erroneously scaled by a factor of 4 in Ref. [67].)

$U_{\rm eff}$ (eV)	$J_{\rm nn}$ (K)	$J_{\rm nnn}$ (K)	$\Theta_{\rm CW}$ (K)
0	174.4	-100.7	36.9
4	154.5	-52.9	50.8
6	134.8	-39.0	47.9
8	108.7	-27.5	40.6

the bridging oxygen $2p$ orbitals.[90, 91] The weaker AFM-NNN interaction may be a consequence of the twisting of the CuO_2 ribbon chains since it reduces the hopping integral between the NNN Cu^{2+} ions.

4.6 Electron Paramagnetic Resonance

EPR measurements of polycrystalline $CuAs_2O_4$ were performed to investigate the Cu^{2+} g-factor. This provides insight on the crystal environment surrounding the magnetic ion. The EPR spetra were measured with a microwave frequency 9.48 GHz in a temperature range of 15 K to 275 K. An EPR spectrum collected at 15 K is displayed in Figure 4.8. The spectrum can be very well modeled by a field derivative of a Lorentzian absorption resonance line, Eq. (3.16). The inset in Figure 4.8 shows how the g-factor varies with temperature. The room-temperature averaged g-factor was determined to be

$$g = 2.103 \pm 0.001.$$

Typically, for a Cu $S = 1/2$ system in an elongated octahedral environment, it is found that $g_\perp \approx 2.05$ to 2.10 and $g_\parallel \approx 2.15$ to 2.25.[101] The EPR measurement is more sensitive to the perpendicular components of the g-factor[102], with this in mind,

the measured g-factor agrees well with what is expected.[101] From the measured g-factor, an effective magnetic moment of $\mu_{\text{eff}} = 1.82\ \mu_{\text{B}}$ is obtained. An analysis of the inverse EPR intensity for $T > 150$ K is shown in Figure 4.9 with a Curie-Weiss type temperature of $\Theta_{\text{EPR}} \approx 40$ K. The positive Θ_{EPR} indicates a predominant FM spin-exchange in accordance with the positive magnetic susceptibility Curie-Weiss temperature (see below) and the DFT calculations. Below ≈ 150 K the inverse integrated intensity bends upwards, away from the Curie-Weiss type fit. A similar behaviour is also seen in the inverse susceptibility data and discussed in detail below. The temperature dependence of the linewidth, shown in the Figure 4.9 inset, displays a broadening with temperatures above ≈ 50 K. Below ≈ 50 K the linewidth decreases which is attributed to a build-up of internal fields caused by magnetic short-range ordering. This may also the source of the temperature variation of the g-factor along with minute changes of the crystal field due to the lattice contractions.

4.7 Magnetization and Magnetic Susceptibility

The magnetic susceptibility as a function of temperature of a randomly oriented selection of $CuAs_2O_4$ crystals is displayed in Figure 4.10. The measurement was collected with a field of 1 T in a temperature range of 1.8 K to 375 K.

At high temperatures, the magnetic susceptibility follows a Curie-Weiss law according to

$$\chi_{\text{mol}} = \frac{C}{T - \Theta_{\text{CW}}} + \chi_0. \tag{4.4}$$

The Curie constant, C, depends on Avogadro's number N_A, the spin of the system S =1/2, the Boltzmann constant k_B, the g-factor g, and the Bohr magneton μ_B, according to

$$C = \text{N}_\text{A} g^2 {\mu_\text{B}}^2 S(S+1)/3k_\text{B}. \tag{4.5}$$

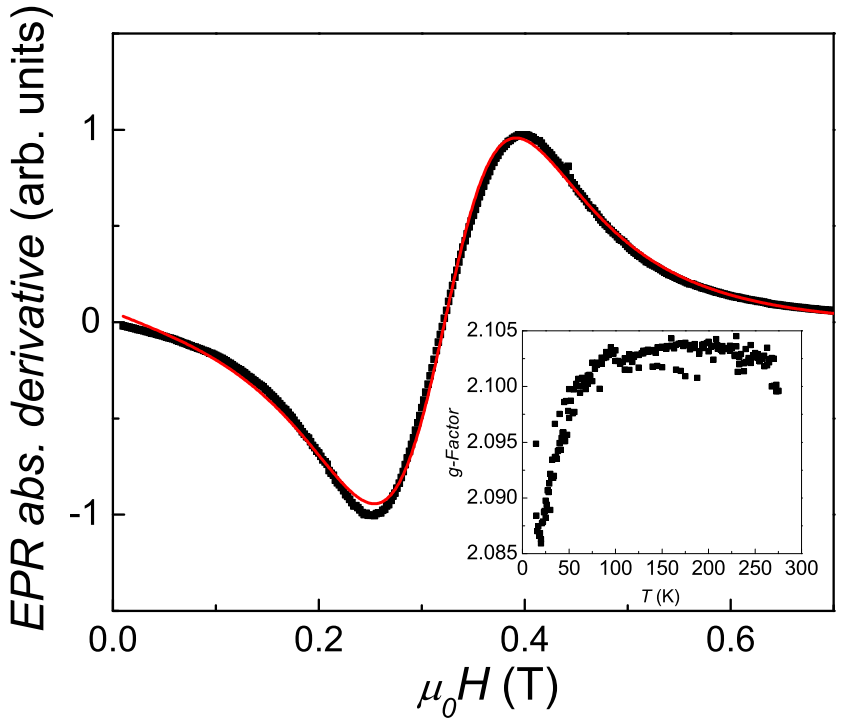

Figure 4.8: **$CuAs_2O_4$ EPR Spectrum.** An EPR spectrum of a polycrystalline $CuAs_2O_4$ sample collected at 15 K with a microwave frequency of 9.48 GHz. The (red) solid line is a fit of the field derivative of the microwave power absorption with a single Lorentzian resonance line according to Eq. (3.16). The inset displays the g-factor variation with temperature.

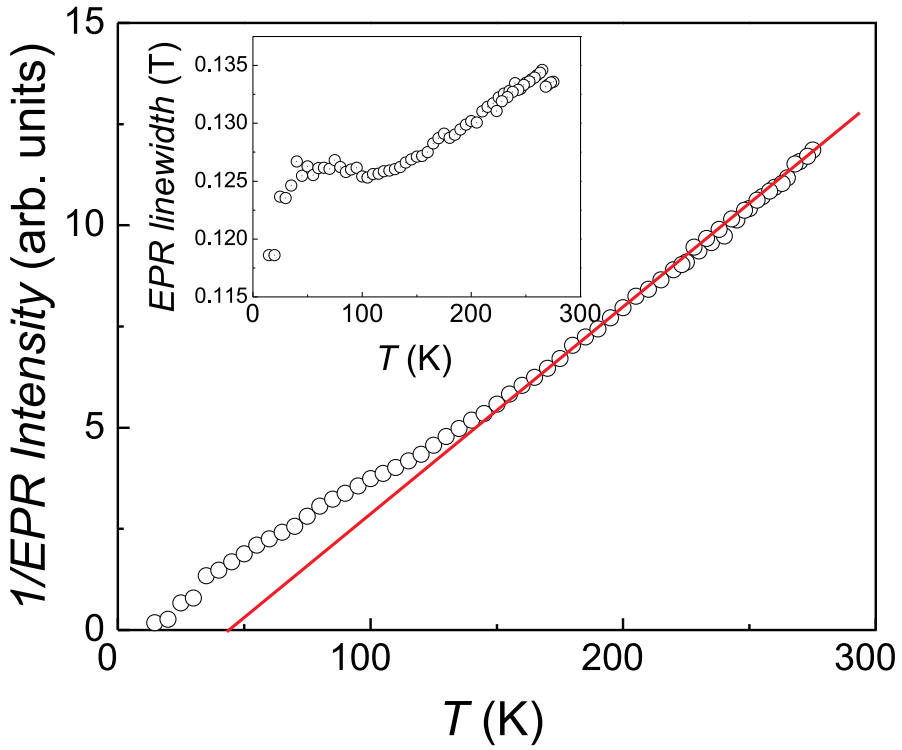

Figure 4.9: **$CuAs_2O_4$ Reciprocal EPR Intensities.** Reciprocal intensities of the EPR resonance lines of a polycrystalline $CuAs_2O_4$ sample obtained from the fits. The (red) solid line is a linear fit of the intensity with a Curie-Weiss like temperature dependence. The inset displays the resonance linewidth (FWHM) broadening with temperature.

The temperature independent term in Eq. (4.4), χ_0, represents a sum of the diamagnetic contributions, χ_{dia}, from the closed electron shells and the van Vleck susceptibility, χ_{VV}, arising from admixtures of the groundstate wave functions into excited Cu electronic levels.

$$\chi_0 = \chi_{\mathrm{dia}} + \chi_{\mathrm{VV}}. \tag{4.6}$$

From the tabulated diamagnetic increments for individual ions, χ_{dia} can be estimated to contribute -77$\times 10^{-6}$ cm^3/mol.[103] The van Vleck susceptibility depends on the direction of the external field with respect to the crystal axes and the energy level separation. For a polycrystalline Cu^{2+} system, it typically amounts to values between +100$\times 10^{-6}$ cm^3/mol and +120$\times 10^{-6}$ cm^3/mol, resulting in a χ_0 of approximately +43$\times 10^{-6}$ cm^3/mol.[104, 105] For more details on diamagnetic and van Vleck contributions, refer to Appendix A.

The (red) solid line in Figure 4.10 shows a fit of the experimental inverse susceptibility to Eq. (4.4) obtained by varying the g-factor and the Curie-Weiss temperature. The best fit to the data above $\approx$ 150 K was found with a g-factor of

$$g = 2.15 \pm 0.01.$$

and a Curie-Weiss temperature of

$$\Theta_{\mathrm{CW}} = 39 \pm 1\mathrm{K}.$$

The positive Curie-Weiss temperature indicates predominant FM spin-exchange interactions, as also found by the EPR measurement and the DFT calculations.

The slight difference in the g-factor obtained by the magnetic susceptibility measurement to that obtained by the EPR measurement (see above) is likely caused by

an anisotropy of the g-factor. The magnetization measurement picks up an average g-factor over randomly oriented crystallites, the EPR experiment is more sensitive to the perpendicular components of the g-factor.[102] Taking $g_{\mathrm{epr}} \approx g_{\perp} \approx 2.10$ and $g_{\mathrm{susc}} \approx g_{\mathrm{avg}} \approx 2.15$ indicates a parallel component of the g-factor of ≈ 2.25, which is an appropriate value for Cu^{2+} in an elongated octahedral environment.[101] Such a g-factor anisotropy corresponds to a difference of the resonance fields which is approximately 15% of the EPR signal linewidth, therefore, typical features of a Cu^{2+} powder cannot be resolved.

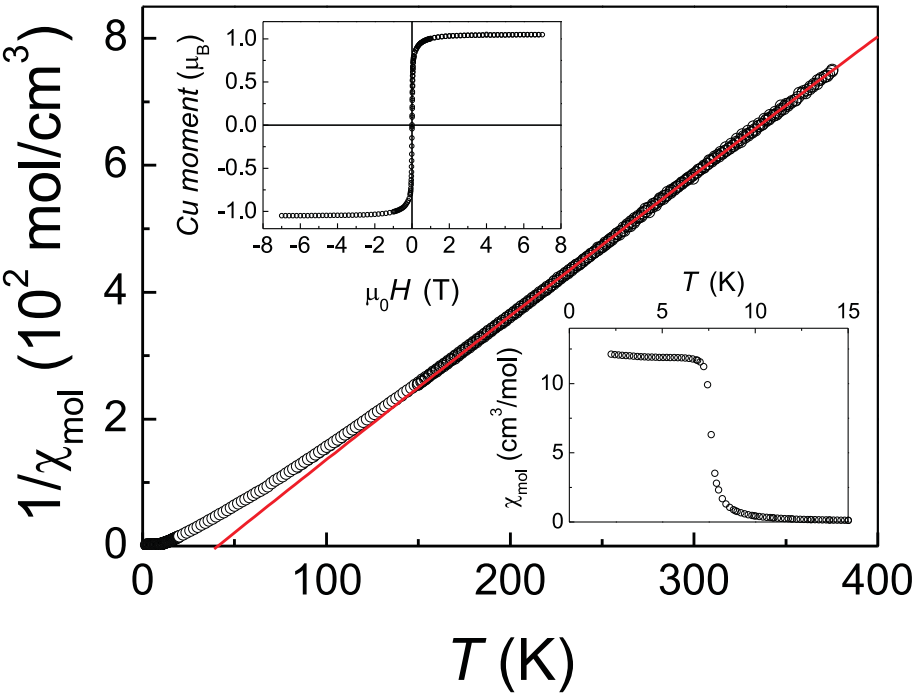

Figure 4.10: **$CuAs_2O_4$ Magnetic Susceptibility.** Reciprocal magnetic susceptibility of a polycrystalline $CuAs_2O_4$ sample measured in a field of 1 T. The solid (red) line is a fit of the Curie-Weiss law (Eq. (4.4)) to the data above 150 K. The lower inset shows the data below 20 K, collected at 0.01 T, in an enlarged scale. The upper inset displays the magnetization versus field collected at 1.85 K.

Below ≈ 8 K the magnetization rises sharply, indicative of a FM transition, see Figure 4.10 lower inset. The Curie temperature, T_C, obtained from the inflection point of the susceptibility curve amounts to

$$T_C = 7.6 \pm 0.2\text{K}.$$

An isothermal magnetization measured at 1.85 K, plotted in the upper inset of Figure 4.10, reveals saturation of the magnetization above a field of ≈ 2.5 T with a value of 1.05 ± 0.01 μ_B. This saturation moment is in good agreement with the expected ≈ 1.1 μ_B value for a S=1/2 system.

Figure 4.11 displays the magnetization at 1.85 K of a single crystal (8 ± 2 μg) oriented with the c-axis parallel and perpendicular to the magnetic field. With the field perpendicular to the c-axis, saturation is readily achieved above ≈ 0.5 T. With the field oriented along the c-axis, saturation is not obtained at 1 T indicating the c-axis to be a magnetic hard axis. The saturation moment is in fair agreement with an expected value of ≈ 1.1 μ_B, the slight excess can be attributed to errors in the mass determination of the crystal.

Below ≈ 150 K, the inverse magnetic susceptibility of $CuAs_2O_4$ noticeably bends upwards from the high-temperature Curie-Weiss law (Figure 4.10), similar to what has also been observed in the integrated signal intensity from the EPR spectroscopy experiment (Figure 4.9). To model the temperature dependence of the susceptibility over the whole temperature range, including the upward deviation from the high-temperature Curie-Weiss law, the magnetic susceptibilities of a S=1/2 Heisenberg spin-chain with NN and NNN spin-exchange interactions were calculated for various α values. These calculations were performed using Transfer-matrix density-matrix renormalization group (TMRG) calculations by collaborator J. M. Law at Dresden

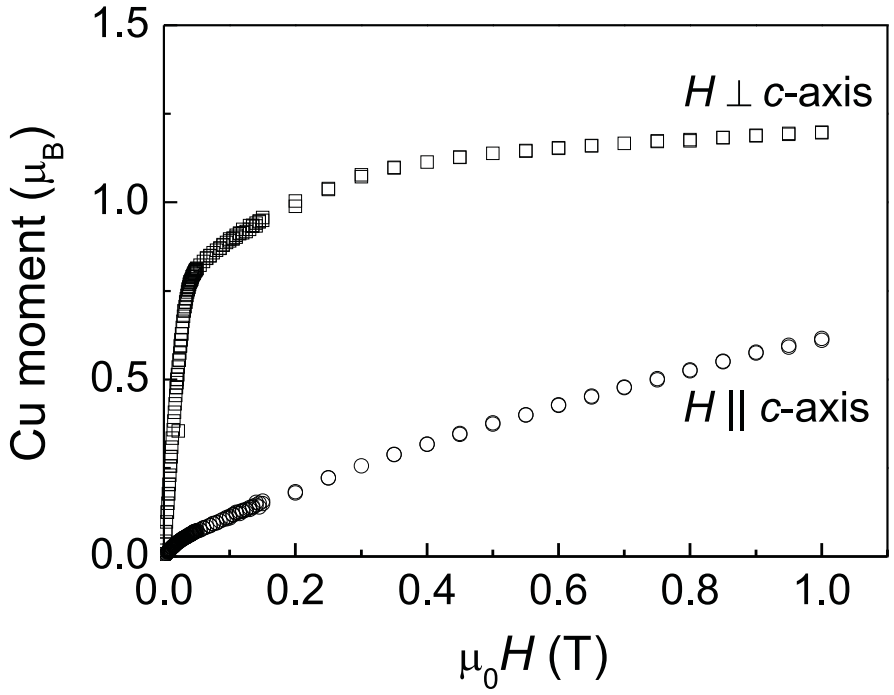

Figure 4.11: **$CuAs_2O_4$ Single-Crystal Magnetization.** Magnetization of an oriented $CuAs_2O_4$ single crystal measured at 1.85 K with the magnetic field $H \parallel c$-axis and $H \perp c$-axis.

Hochfeld-Magnetlabor.[106, 107] The temperature dependent magnetic susceptibilities, χ^* of a S=1/2 Heisenberg spin-chain with NN and NNN spin-exchange interactions are shown in Figure 4.12. χ^* was calculated for ratios -4.5 $\leq J_{\mathrm{nn}}/J_{\mathrm{nnn}} \leq$-3.5 and an antiferromagnetic NNN spin-exchange constant of J_{nnn} = -38 K, consistent with the results of the DFT calculations. Additionally, a g-factor of g_{TMRG} = 2.155, very close to the g-factor obtained from the Curie-Weiss fit, was used.

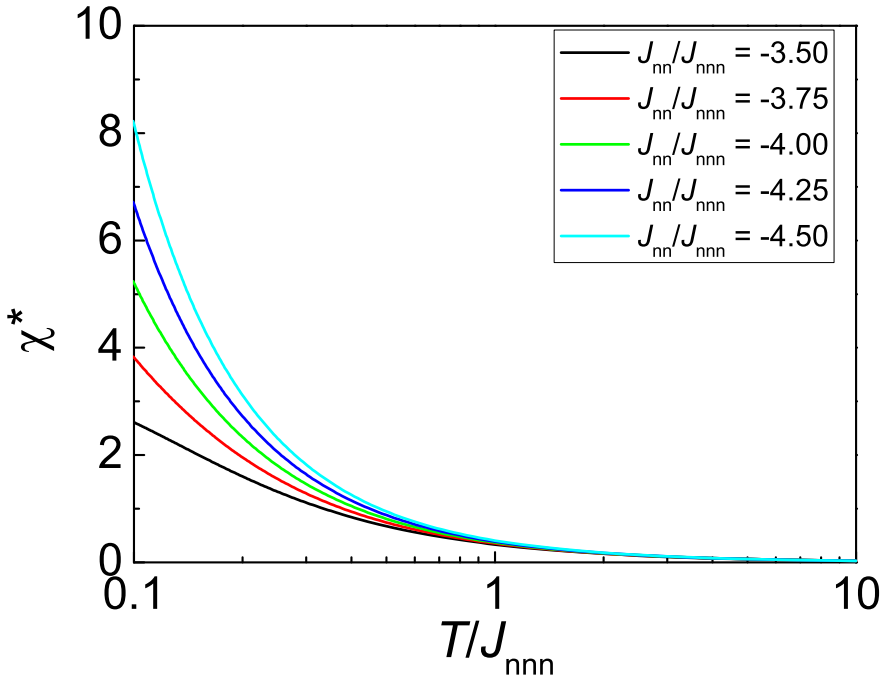

Figure 4.12: **Magnetic Susceptibilities from TMRG Calculations.** TMRG spin susceptibilities, χ^*, versus temperature for various ratios of the NN to NNN spin exchange interactions as indicated in the inset. $\chi^* = \chi_{\mathrm{mol}} J_{\mathrm{nnn}}/N_{\mathrm{A}}\mu_{\mathrm{B}}^2 g^2$.

Figure 4.13 displays the experimental data in comparison with the TMRG susceptibility results. The best fit was achieved for α = -4.25. Combining this result with the DFT calculations leads to an average value of $\alpha \approx$ -4.1, in close proximity to the quantum critical limit at α = -4 (Figure 2.7).

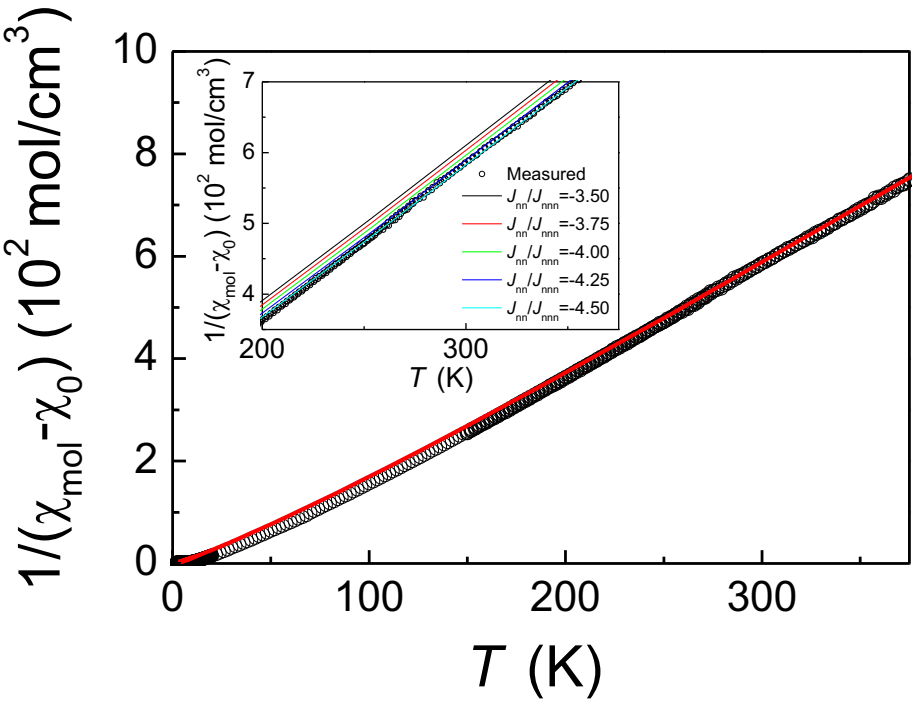

Figure 4.13: **TMRG fit to $CuAs_2O_4$.** The inverse experimental susceptibility shown in Figure 4.10 (corrected by a temperature independent part χ_0 = 43×10^{-6} cm^3/mol) compared with the results of the TMRG calculations, solid (red) line, for the ratio $J_{\rm nn}/J_{\rm nnn}$ = -4.25 (main frame). The inset displays the TMRG results, solid (red) lines, for $J_{\rm nn}/J_{\rm nnn}$ = -3.5, -3.75, -4, -4.25, -4.5 (from top to bottom). For all theoretical curves $J_{\rm nnn}$= -38 K and a g-factor of 2.155 was used. For further details see text.

4.8 Arrott-Noakes Plot

An Arrott plot analysis of magnetization isotherms of a ferromagnet is a well-established method to determine the Curie temperature, T_C, and the zero-field magnetic polarization. Arrott and Noakes proposed a modified equation of state which takes into account the critical exponents β and γ of the magnetization and the magnetic susceptibility, respectively.[108] The Arrott-Noakes equation of state is given by

$$(\mu_0 H/M)^{1/\gamma} = (T - T_C)/T_1 + (M/M_1)^{1/\beta}. \tag{4.7}$$

T_1 and M_1 are material constants which for $CuAs_2O_4$ were fitted to $T_1 = 0.04 \pm 0.01$ K and $M_1 = 1.42 \pm 0.01$ T. The critical exponents can be extracted from a representation of $M^{1/\beta}$ versus $(\mu_0 H/M)^{1/\gamma}$, with the critical exponents adjusted such that the isotherms close to the Curie temperature follow a linear behaviour. A modified Arrott-Noakes plot of $CuAs_2O_4$ is shown in Figure 4.14. The critical isotherm, which extrapolates to the origin of the graph, lies between the isotherms measured at 7.00 K and 7.50 K. The best agreement with linear behavior for the isotherms near T_C was obtained by adjusting the critical exponents to

$$\beta = 0.35 \pm 0.01,$$

and

$$\gamma = 1.32 \pm 0.01.$$

The critical exponent β for the magnetization is consistent with values for standard universality classes 3d-Heisenberg and 3d-XY, but within the experimental error does not allow for a differentiation between the two cases.[109–111] γ is clearly lower than the value expected for a 3*d*-Heisenberg model but is close to the value expected for

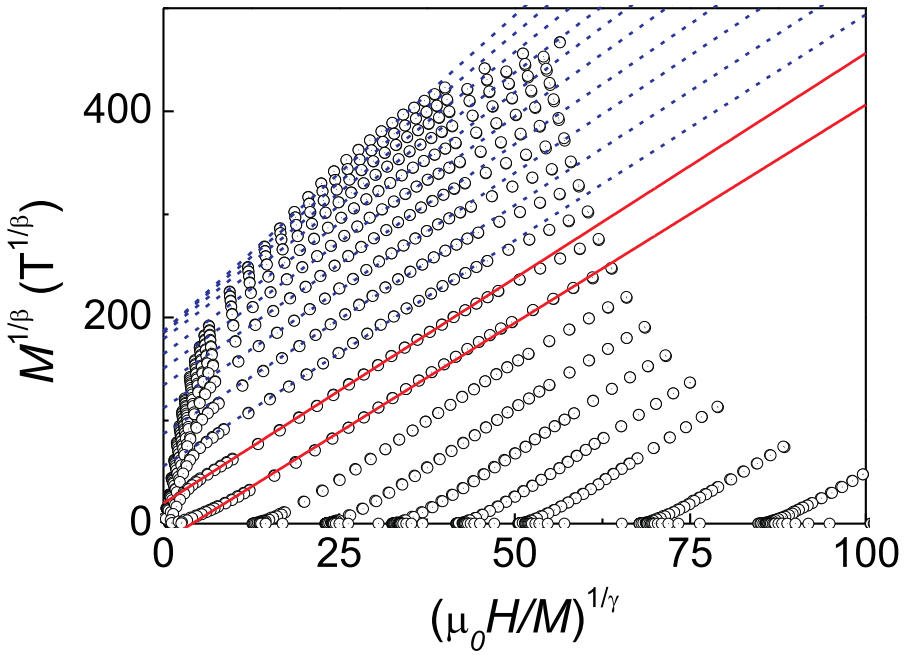

Figure 4.14: **Arrott-Noakes Plot of $CuAs_2O_4$.** Arrott-Noakes plot of the isothermal magnetization of a $CuAs_2O_4$ polycrystalline sample. The two solid (red) lines mark the magnetization curves measured at 7.00 K and at 7.50 K. The dashed (blue) lines mark the isotherms used to extract the zero-field magnetic polarization plot. The isotherms are in steps of 0.5 K starting from top curve at ≈2 K.

a 3*d*-XY class.[109–111] This finding is consistent with the anisotropy seen in the single-crystal magnetization measurement indicating an easy-plane perpendicular to the *c*-axis.

Figure 4.15 displays the temperature dependence of the zero-field polarization obtained by extrapolating the high-field data in the modified Arrott plot, $H \to 0$. By fitting a critical power law according to

$$M(T) = M_0(1 - T/T_{\mathrm{C}})^{\beta}. \tag{4.8}$$

With β fixed to 0.35 as shown in the Modified Arrott plot, a Curie temperature of

$$T_{\mathrm{C}} = 7.35 \pm 0.05\mathrm{K}$$

is extracted. This Curie temperature is in good agreement with the magnetic susceptibility data.

4.9 Heat Capacity

Heat capacity measurements were performed on a sample of randomly oriented $CuAs_2O_4$ crystals versus temperature and magnetic field. The results are shown in Figure 4.16. In zero-field, a λ-shaped anomaly appears at 7.4 $\pm$ 0.1 K, which agrees with the T_{C} results from the magnetic data. Applying a magnetic field causes a slight up-shift in temperature and broadening of the anomaly.

Two approaches were taken in order to subtract the lattice contribution to the heat capacity and extract the magnetic heat capacity, $C_{\mathrm{mag}}(T)$. i) The lattice contribution to the heat capacity of $CuAs_2O_4$ was approximated by fitting a superposition of a

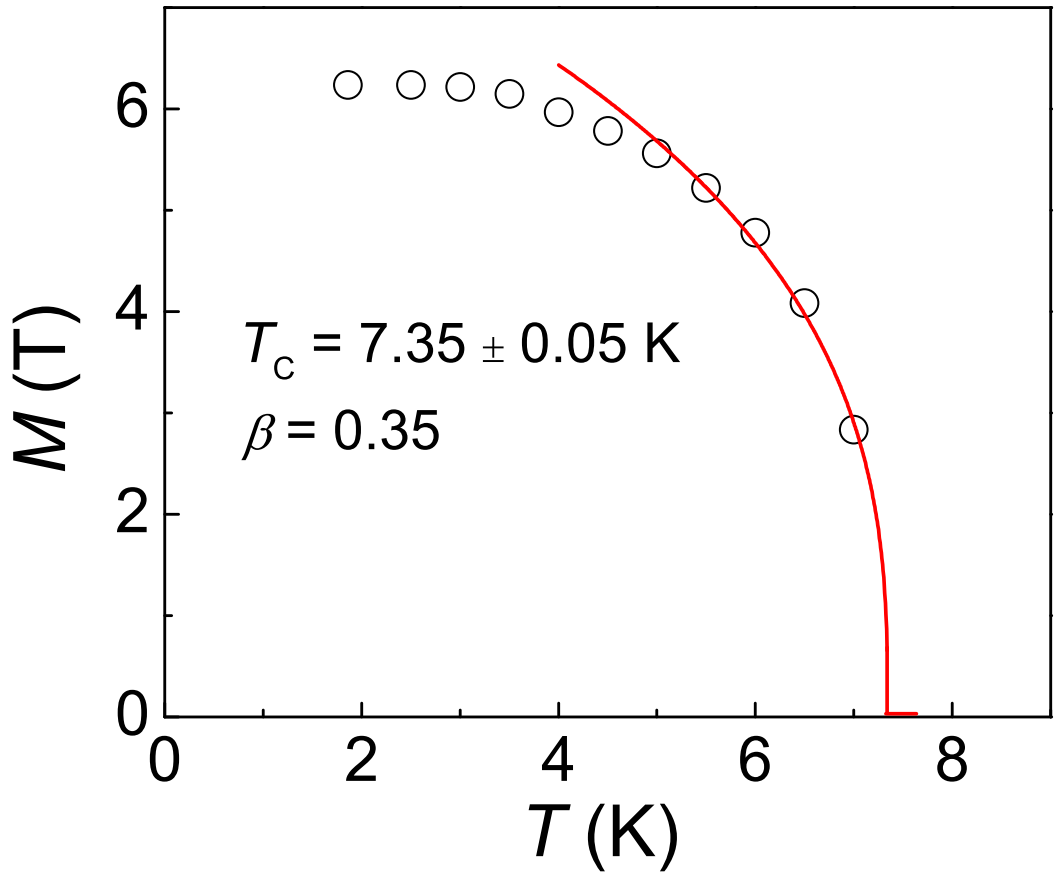

Figure 4.15: **$CuAs_2O_4$ Magnetic Polarization.** Temperature dependence of the zero-field magnetic polarization of $CuAs_2O_4$. The data points were obtained from the intersections with the ordinate of the linearly extrapolated high-field branches in the Arrott-Noakes plot (i.e. $H \to 0$). The (red) solid line represents a critical power law fitted to the data points near T_C with a fixed critical exponent $\beta = 0.35$.

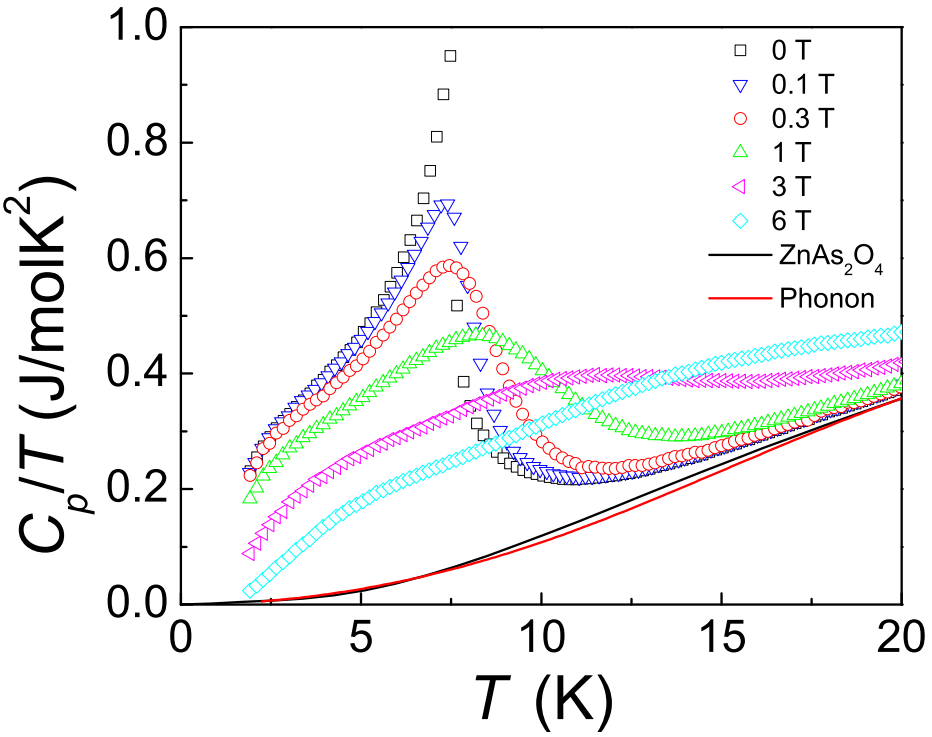

Figure 4.16: **Heat Capacity of $CuAs_2O_4$.** Heat capacity of a randomly oriented ensemble of $CuAs_2O_4$ crystals versus temperature and external magnetic field. The solid lines represent the scaled heat capacity of the hypothetical compound $ZnAs_2O_4$ and a phonon contribution to the heat capacity as obtained by extrapolating the Debye-Einstein fit (Eq. 4.9) to low temperatures.

Debye-type and two Einstein-type heat capacity terms according to

$$C_P(T) = f_{\mathrm{D}} C_{\mathrm{Deb}}(\Theta_{\mathrm{Deb}}, T) + \sum_i g_i C_{\mathrm{Ein},i}(\Theta_{\mathrm{Ein},i}, T). \tag{4.9}$$

The Debye-type heat capacity is given by

$$C_{\mathrm{Deb}}(T) = 9R(T/\Theta_{\mathrm{Deb}})^3 \int_0^{\Theta_{\mathrm{Deb}}/T} \frac{x^4 \exp(x)}{(\exp(x)-1)^2} dx. \tag{4.10}$$

In order to simplify the fit procedure, a Padé approximation for the Debye-type heat capacity, proposed by Goetsch *et al.*, was utilized.[112] The Einstein-type heat capacities, $C_{\mathrm{Ein},i}(T)$, were calculated according to

$$C_{\mathrm{Ein},i}(T) = 3R(\frac{E_i}{k_{\mathrm{B}}T})^2 \frac{\exp(E_i/k_{\mathrm{B}}T)}{(\exp(E_i/k_{\mathrm{B}}T)-1)^2}. \tag{4.11}$$

The weight prefactors, f_D, g_1 and g_2, were conditioned such that at sufficiently high temperatures the Petit-Dulong value of $7\times3R$ (R is the molar gas constant) was satisfied. By fitting the weights, the Debye-temperature, and two Einstein-temperatures, the experimental heat capacity above 20 K could be well approximated and extrapolated to $T \to 0$ K (see Figure 4.16). The Einstein-temperatures were given initial values of $E_1 = 215$ K and $E_2 = 720$ K. These initial values correspond to the center positions of the two major groups of phonon modes in the $ZnAs_2O_4$ DOS (Figure 4.4). The fitted parameters are summarized in Table 4.4.

ii. Alternatively, the heat capacity of the hypothetical compound $ZnAs_2O_4$ was calculated from the phonon density of states obtained by *ab initio* calculations (see above, Figure 4.4) and the second derivative of the free energy, $F(T)$. The relation is as follows

$$C_V(T) \approx C_P(T) = -T \left(\frac{\partial^2 F(T)}{\partial T^2} \right)_V, \tag{4.12}$$

Table 4.4: **$CuAs_2O_4$ Lattice Heat Capacity Fit Parameters.** Weights and characteristic temperatures used to approximate the lattice contribution to the heat capacity of $CuAs_2O_4$ according to Eq. (4.9). The weights were conditioned such that $f_D + g_1 + g_2 = 7$.

contribution	weight	T(K)
Debye	1.5	136.59(7)
Einstein, i=1	2.25	284.5(3)
Einstein, i=2	3.25	789(1)

where $C_V(T)$ and $C_P(T)$ are the heat capacities at constant volume and at constant pressure (accessible by the experiment), respectively. $F(T)$ is the free energy given by

$$F(T) = -\int_0^\infty (\frac{\hbar\omega}{2} + k_\mathrm{B}T\ln[2n_\mathrm{B}(\omega)])\rho(\omega)d\omega. \tag{4.13}$$

Where k_B represents the Boltzmann constant, n_B the Bose-Einstein factor, and $\rho(\omega)$ the phonon density of states. The high frequency cut-off of the latter defines the upper limit of integration in Eq. (4.13).

The extracted magnetic contribution to the specific heat was obtained by subtracting the lattice contribution from the experimental results. A plot of $C_\mathrm{mag}(T)/T$ versus T is shown in the Figure 4.17. At low temperatures the magnetic heat capacity follows a power law

$$C_\mathrm{mag}(T) \propto T^n, \tag{4.14}$$

with $n \approx 1.2$, somewhat lower than expected for 3D FM magnon ($n = 3/2$, Eq. 3.12) contributions. Above ≈ 20 K, a shoulder becomes visible which is attributed to short-range ordering contributions.

By integrating $C_\mathrm{mag}(T)/T$, the magnetic entropy removed by the magnetic ordering is obtained according to

$$S_\mathrm{mag}(T) = \int_0^T C_\mathrm{mag}(T')/T'dT'. \tag{4.15}$$

The magnetic entropy amounts to

$$S_{\mathrm{mag}} = 4.0(1)\mathrm{J/molK},$$

which is $\approx 70\%$ of the entropy expected for a $S = 1/2$ system,

$$S_{\mathrm{mag}} = R\ln(2S+1) = R\ln(2). \tag{4.16}$$

The largest fraction of the entropy is contained in the λ-anomaly and only a minor fraction is removed by short-range ordering effects which were also seen in the g-factor temperature dependence.

4.10 Conclusion

In summary, I have investigated the structural and magnetic properties of $CuAs_2O_4$. A system characterized by Jahn-Teller elongated CuO_6 octahedra which link together via opposite edges of their basal planes to form CuO_2 ribbon chains. The ribbon-chains are magnetically frustrated with FM-NN and AFM-NNN intra-chain interactions. Additionally, $CuAs_2O_4$ exhibits a spin-exchange ratio $\alpha = J_{\mathrm{nn}}/J_{\mathrm{nnn}} \approx$ -4.1. This value places $CuAs_2O_4$ in the ferromagnetic regime of the magnetic phase diagram (Figure 2.7), near to the quantum critical point between frustrated incommensurate spin-spiral and ferromagnetic order. To date, $CuAs_2O_4$ seems to lie closest to quantum criticality at α = -4 of all systems reported so far. Two other Cu spin-chain systems reported close to quantum criticality are Li_2ZrCuO_4 and $Ca_2Y_2Cu_5O_{10}$ which exhibit spin-exchange ratios or -4.5 and -5.3 respectively.[113–115]

X-ray diffraction measurements showed that $CuAs_2O_4$ crystallizes in a tetragonal structure supporting CuO_2 ribbon-chains and strong Jahn-Teller elongations. Mag-

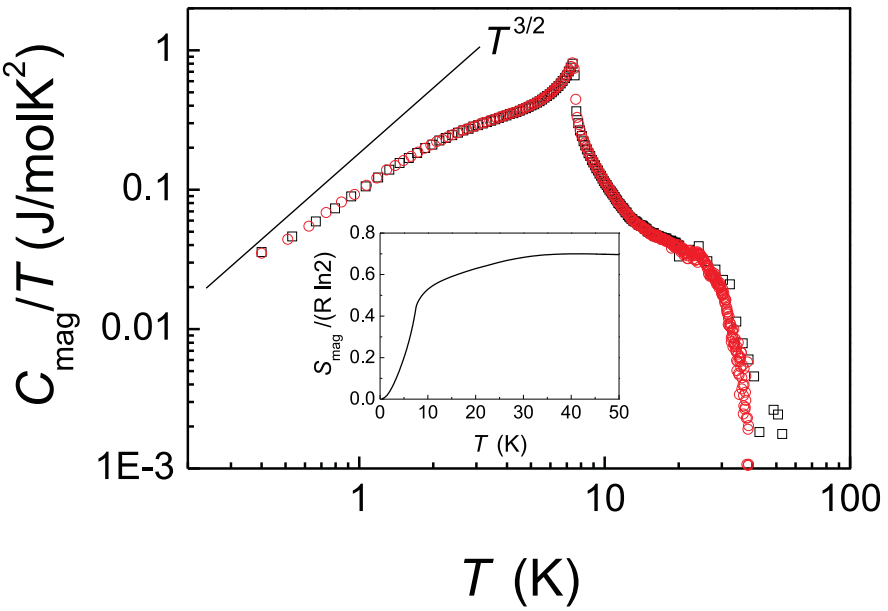

Figure 4.17: **$CuAs_2O_4$ Magnetic Heat Capacity.** Magnetic contribution to the specific heat of $CuAs_2O_4$ ($H = 0$ T). Different symbols (red and black) indicate two independent runs of a selection of $CuAs_2O_4$ crystals. The inset displays the temperature dependence of the magnetic entropy obtained according to Eq. (4.15). The straight (black) line indicates a $T^{3/2}$ power law.

netic susceptibility and heat capacity measurements revealed long-range FM order below $\approx$ 7.4 K. The dominant spin-exchange interactions are the competing FM-NN and AFM-NNN intrachain interactions while the smaller interchain interactions lead to the long-range ordering. Arrott-Noakes analysis and single-crystal magnetization measurements indicated a magnetic anisotropy with an easy-axis along the crystallographic c-axis. EPR measurements and a Curie-Weiss fit to the magnetic susceptibility revealed an average g-factor of $g \approx 2.15$ and a positive Curie-Weiss temperature reflecting the dominant FM-NN interactions. Raman scattering measurements showed that the crystal structure is preserved across the T_C and down to 4 K.

5

Competing Jahn-Teller Distortions and Pressure Effects in $CuAs_2O_4$

The contents of the chapter have been submitted as a manuscript for publication to the American Physical Society: "Competing Jahn-Teller Distortions and Pressure Effects in the Quasi-One-Dimensional Quantum Ferromagnet $CuAs_2O_4$" K. Caslin, R. K. Kremer, F. S. Razavi, M. Hanfland, K. Syassen, E. E. Gordon, and M.-H. Whangbo, Physical Review B **Submitted**, (2015).

In this chapter, I extend the investigation of $CuAs_2O_4$ to include structural and magnetic characterizations under hydrostatic pressure up to $\approx$ 11.5 GPa. Of particular interest was whether the pressure-induced changes in the interatomic distances and angles could be used to tune the ratio of the NN and NNN spin-exchange interactions and possibly push $CuAs_2O_4$ towards a new magnetic groundstate. It was found that the magnetic ordering temperature of $CuAs_2O_4$ increases continuously with pressure up to $\approx$ 9 GPa, at which point a structural phase transition occurs with a severe alteration of the magnetic properties. Crystal structure analysis with single-crystal x-ray diffraction experiments up to $\approx$ 9 GPa indicated that the axial elongations of the CuO_6 octahedra caused by Jahn-Teller distortions were markedly suppressed. The derived structural parameters could favorably be used as input for

calculations on the intrachain spin-exchange parameters versus pressure. The calculations indicated that external pressure up to $\approx$ 9 GPa increases the ferromagnetic NN spin-exchange by about 40% whereas the antiferromagnetic NNN spin-exchange remained approximately constant.

A single-crystal to single-crystal structural phase transition (Phase I $\rightarrow$ Phase II) was identified at $\approx$ 9 GPa by Raman spectroscopy and synchrotron x-ray diffraction measurements. The crystal structure in Phase II is characterized by an increased twisting of the CuO_2 ribbon-chains and a tetragonal-to-orthorhombic distortion of the oxygen environment in the basal plane of the CuO_6 octahedra. In Phase II, the NN and NNN spin-exchange parameters were found to be both ferromagnetic and significantly reduced in magnitude as compared to Phase I. Magnetic susceptibility measurements with pressure above 9 GPa identified a drastic reduction of the magnetic ordering temperature.

5.1 Raman Scattering Under Hydrostatic Pressure

In order to search for pressure induced structural changes, the Raman spectra of $CuAs_2O_4$ single-crystals were measured from 0 to 20 GPa at T = 295 K in a diamond anvil cell. The Raman spectra for various pressures are displayed in Figure 5.1. With the limitations imposed by the diamond anvil cell, only five definite Raman modes out of the 26 expected from symmetry considerations could be identified.[67] At a pressure of 2.67 GPa, the identifiable modes were centered at wavenumbers 203.5 cm^{-1}, 290.3 cm^{-1}, 382.3 cm^{-1}, 512.7 cm^{-1}, and 794 cm^{-1}, consistent with the previously published data for ambient pressure.[67] Up to 9 GPa, the Raman peaks shift to higher wavenumbers reflecting the lattice stiffening due to external

pressure. Above 9 GPa, new peaks and peak splittings appear and continue to grow as pressure is increased. These features indicate a structural phase transition at $\gtrsim 9$ GPa. The Raman spectra of the high pressure phase show an increased number of peaks compared to the ambient pressure phase, indicating a symmetry reduction of the crystal structure.

Figure 5.2 displays the Raman shift of the observed peaks versus the pressure and the unit cell volume, $v(P)$, as determined from synchrotron x-ray diffraction (see below). It allows for the determination of the average Grüneisen parameters of the respective modes, γ_i, at the center of the Brillouin zone according to

$$\gamma_i = -\frac{\delta \ln(\omega_i(P))}{\delta \ln(v(P))} \approx -\frac{v(0)}{\omega_i(0)} \frac{\Delta\omega_i(P)}{\Delta v(P)}, \tag{5.1}$$

where $\omega_i(P)$ is the frequency for the respective Raman mode, and $\Delta\omega_i(P)$ and $\Delta v(P)$ are the pressure induced changes in the frequency of the mode i and the pressure induced volume change, respectively. For all Raman modes, a linear relationship $\Delta\omega_i(P)$ versus $\Delta v(P)$ can be fitted to the data. The initial linear slopes are listed in Table 5.1. A closer inspection of the the E_g modes with resonance frequencies of 275.4 cm^{-1} and 497.1 cm^{-1}, revealed slight deviations from linearity for pressures above ≈ 7 GPa. The 275.1 cm^{-1} mode curves slightly downwards whereas the the 497.1 cm^{-1} bends slightly upwards.

5.2 Synchrotron X-ray Diffraction

At ambient pressure (Phase I), $CuAs_2O_4$ crystallizes in a tetragonal structure with space group $P4_2/mbc$ (no. 135), see Figure 4.3. The system contains Cu^{2+} spin-chains running along the crystallographic c-axis within CuO_2 ribbon-chains. The ribbon-chains are formed from linked basal planes of edge sharing CuO_6 octahedra.

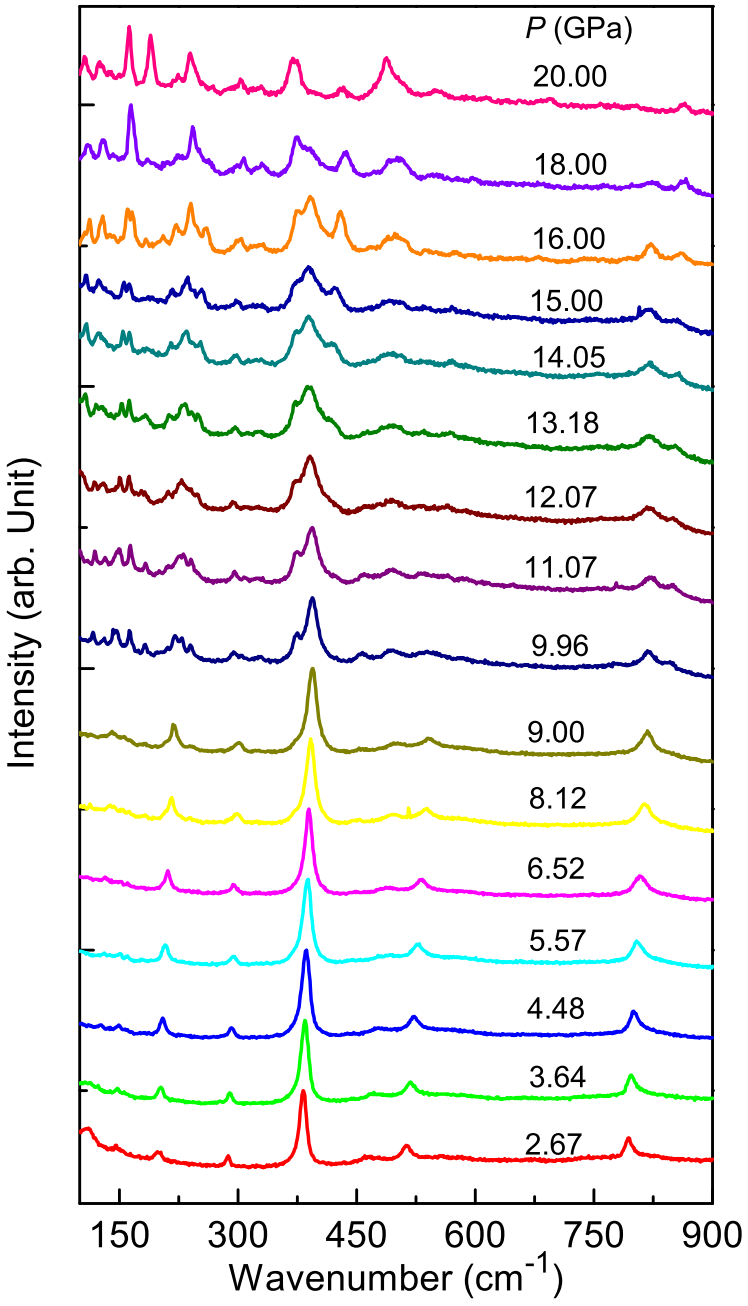

Figure 5.1: **$CuAs_2O_4$ Raman Spectra Under Hydrostatic Pressure.** Raman spectra of a single-crystal of $CuAs_2O_4$ at various external pressures. Additional peaks appear above 9 GPa indicating the occurrence of a structural phase transition.

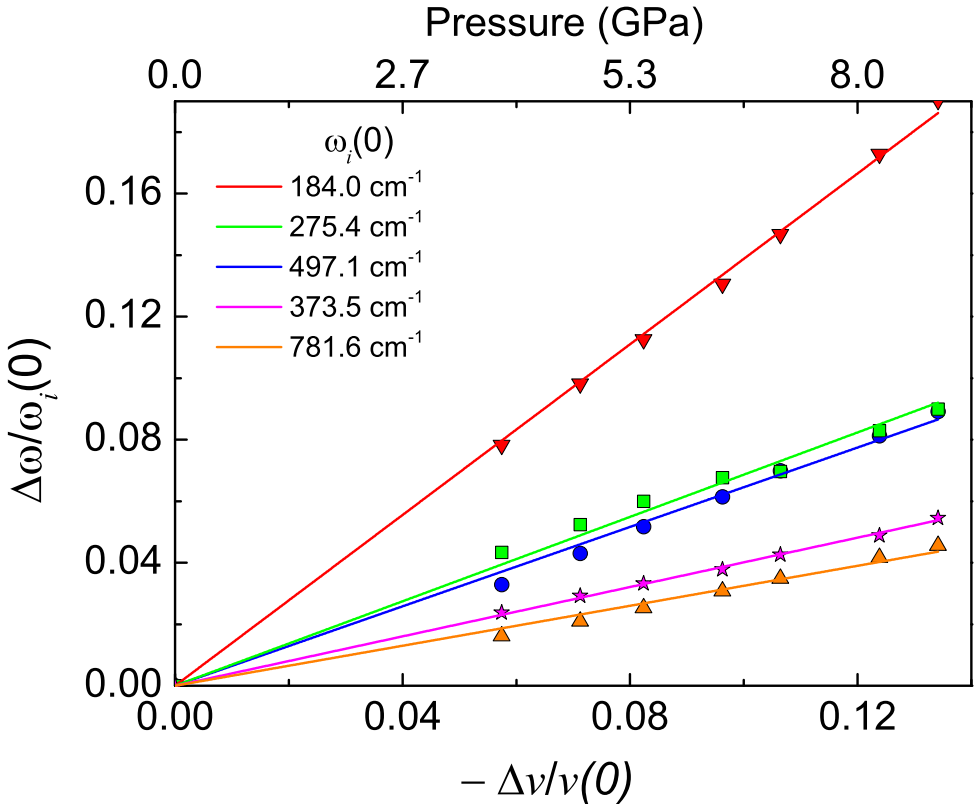

Figure 5.2: **$CuAs_2O_4$ Average Grüneisen Parameter.** Variation of the Raman mode positions versus the unit cell volume variation of $CuAs_2O_4$ in Phase I. The solid lines represent linear slopes obtained from least-squares fits to Eq. (5.1).

Table 5.1: **$CuAs_2O_4$ Raman Grüneisen parameters.** Mode Grüneisen parameters, γ_i, for the five observed Raman modes obtained from the fits shown in Figure 5.2. The $\omega_i(0)$ values are the ambient pressure frequencies for the selected Raman modes.

Symmetry	$\omega_i(0)$ (cm^{-1})	γ_i
E_g	184.0	1.39(1)
E_g	275.4	0.73(1)
E_g	373.5	0.40(1)
E_g	497.1	0.61(1)
B_{1g}	781.6	0.33(1)

The CuO_6 octahedra experience Jahn-Teller distortions and are axially elongated along the crystallographic diagonals in the *a*-*b* plane. The octahedra are composed of two different oxygen sites, four O(2) atoms in the basal planes, and two O(1) atoms at the apex positions. The Cu-O(1) distances are enlarged by 20% compared to the Cu-O(2) distances reflecting strong Jahn-Teller distortions. The ribbon-chains are twisted so that each edge of the CuO_2 ribbon-chain has the buckled O(2)-O(2)-O(2) buckling angle of $\approx 168.2^o$, and the two edges have opposite senses of a buckling. The apex oxygen atoms are exactly centered above and below the Cu atoms such that the O(1)-Cu-O(1) angle amounts to 180^o.

The reduction of the lattice parameters with pressure as determined from the x-ray diffraction data are displayed in Figure 5.3. The lattice compression is prominent along the *a*,*b*-axes and less so along the *c*-axis. Application of pressure leads to a non-linear decrease of the distances between the Cu and the apex O(1) atoms. At 9 GPa, the decrease amounts to $\approx 10\%$. Consequently, the large reduction with pressure of the Cu-O(1) bond length implies a suppression of the Jahn-Teller elongation. The Cu-O(2) distances in the basal planes, however, decrease linearly with pressure and at 9 GPa the reduction amounts to only $\approx 1\%$. Figure 5.4 displays the Cu-O(2)-Cu angle, relevant for the NN super exchange, and the O(2)-O(2)-O(2) buckling angle. The Cu-O(2)-Cu angle decreases linearly with pressure and at 9 GPa the decrease amounts to ≈ 2.5 %. The O(2)-O(2)-O(2) buckling angle decreases by ≈ 3.5 % at 9 GPa.

The x-ray diffraction data evidenced no symmetry change of the crystal structure up to a pressure of 9.2(2) GPa. At this pressure, a structural phase transition from single-crystal Phase I $\rightarrow$ single-crystal Phase II is observed. Figure 5.5 displays two single-crystal x-ray diffraction frames for Phase I and Phase II with *hkl* indices of the Bragg reflections given. In Phase II, the structure can be described by the spacegroup

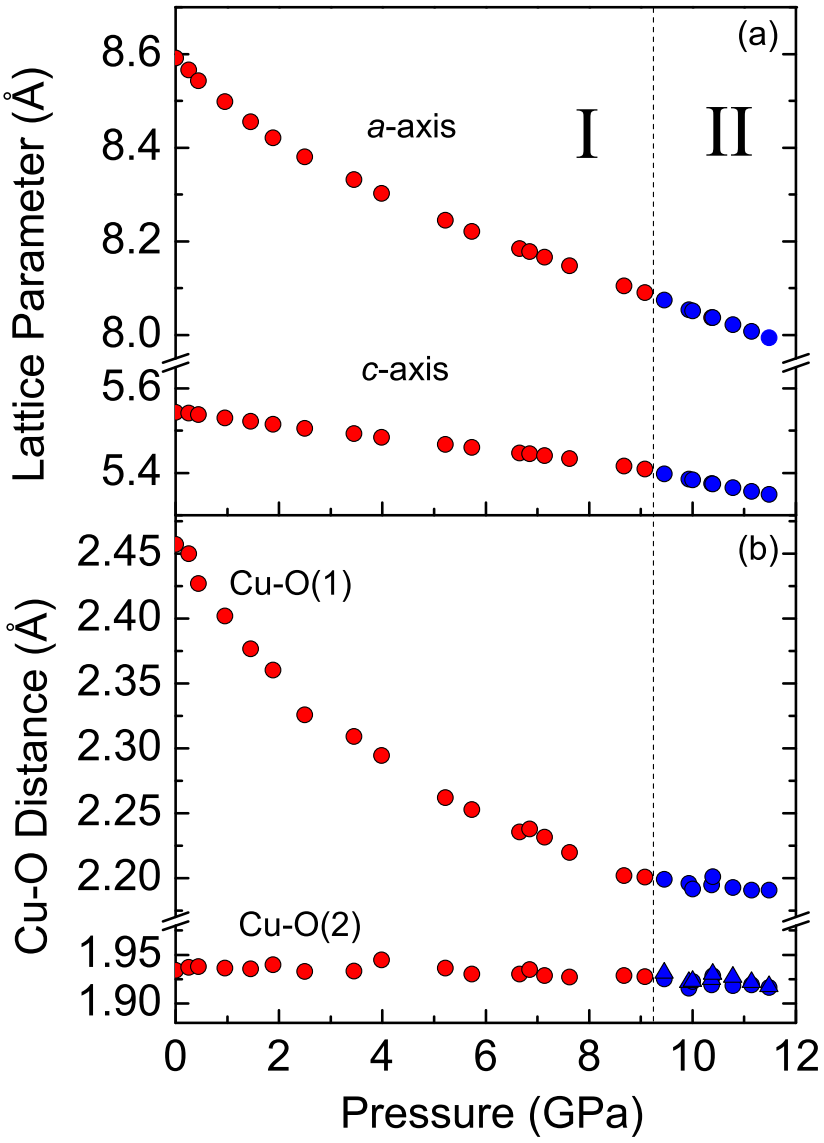

Figure 5.3: **$CuAs_2O_4$ Structural Parameters.** (a) The lattice parameters of $CuAs_2O_4$ versus pressure in Phase I and Phase II. (b) The bond length of the Cu atoms to the apex oxygen atoms, Cu-O(1), and to the oxygen atoms in the equatorial plane (O(2) atoms). In Phase II two different Cu-O(2) distances are found which are labeled by different symbols. The non-linear decrease of the Cu-O(1) distance with increasing pressure is clearly visible. Data points from Phase I (red) and Phase II (blue) are shown with the phase transition indicated by a dashed line.

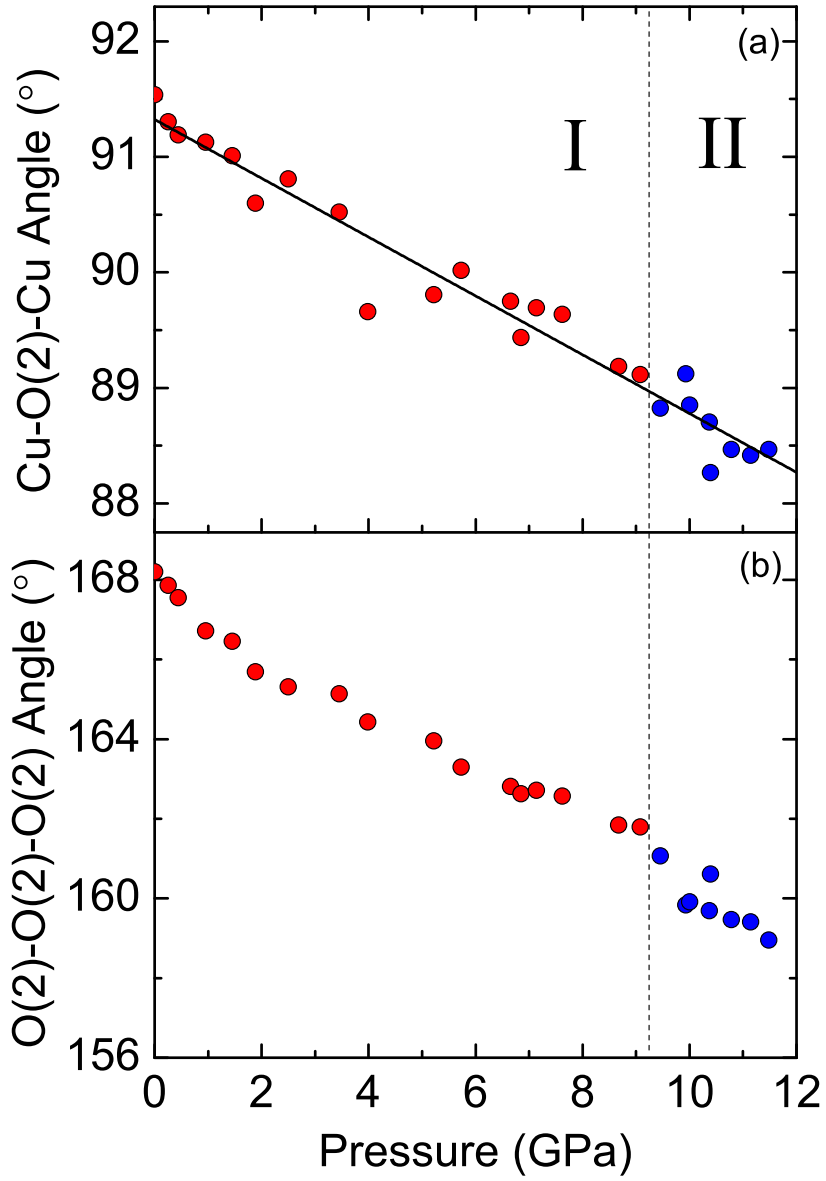

Figure 5.4: **$CuAs_2O_4$ Ribbon-Chain Angles.** The effect of pressure on the (a) NN exchange bonding angle, Cu-O(2)-Cu, and (b) the ribbon-chain buckling angle, O(2)-O(2)-O(2). Data points from Phase I (red) and Phase II (blue) are shown with the phase transition indicated by a dashed line.

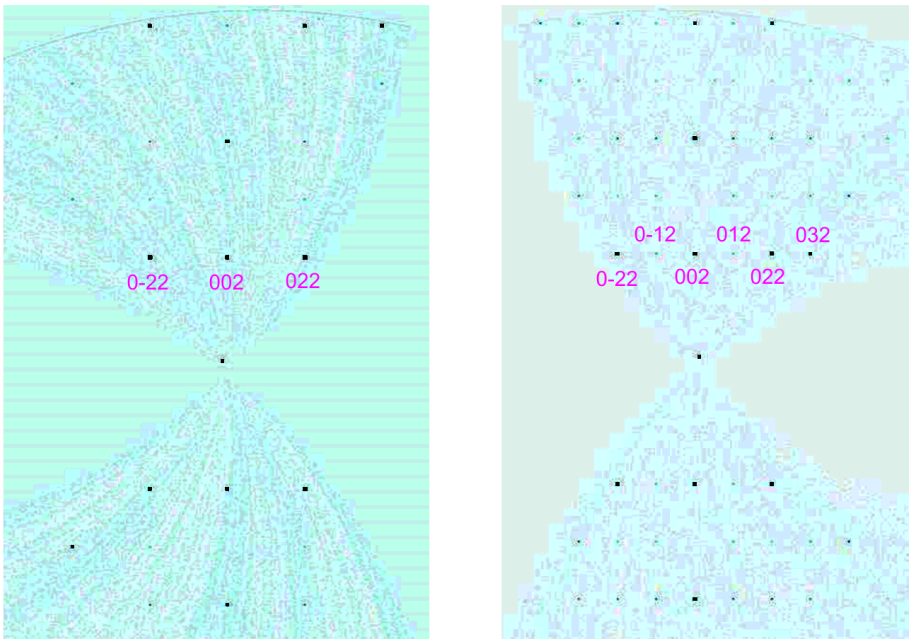

Figure 5.5: **$CuAs_2O_4$ Single-Crystal Diffraction Pattern.** Reciprocal space reconstruction of the 0kl-plane of $CuAs_2O_4$ at 9.1 (Phase I, left) and 10.4 GPa (Phase II, right). Above 10.4 GPa, weak additional 0kl reflections with k odd appear.

$P\bar{4}2_1c$ (no. 114). The number of accessible Raman modes for $CuAs_2O_4$ in Phase II is 52 compared to the 26 Raman modes accessible in Phase I, an increased number of modes in Phase II was observed. The structural parameters refined from the x-ray diffraction data collected at ambient pressure and 11.5 GPa are summarized in Table 5.2.

The transition from Phase I to Phase II is a translationsgleiche (lattice equivalent) transition of index 2 according to $P4_2/mbc \rightarrow t2 \rightarrow P\bar{4}2_1c$, where $P\bar{4}2_1c$ is a maximal subgroup of $P4_2/mbc$. In Phase II, $CuAs_2O_4$ maintains a tetragonal crystal structure supporting CuO_2 ribbon-chains. Compared to Phase I, the structural changes in Phase II are predominantly found in the distortions of the oxygen octahedra. Figure 5.6 displays a projection of the CuO_6 octahedra chains along the [110] direction in the low and high pressure phases. In Phase II, the four equidistant Cu-O(2) bonds in

Table 5.2: **$CuAs_2O_4$ Structural Parameters Under Pressure.** Structural parameters of Phase I (0 GPa) and Phase II (11.5 GPa) of $CuAs_2O_4$. The tabulated parameters for Phase I were refined in spacegroup $P4_2/mbc$ (no. 135) from the data obtained at ambient pressure with lattice parameters a = 8.5913(1) Å and c = 5.5437(1) Å. The tabulated parameters for Phase II were refined from the data collected at 11.5 GPa assuming the spacegroup $P\bar{4}2_1c$ (no. 114) with lattice parameters a = 7.9945(1) Å and c = 5.3491(1) Å. The refinement agreement factors are R_{obs} = 0.0186, wR_{obs} = 0.0215 for Phase I and R_{obs} = 0.0207, wR_{obs} = 0.0313 for Phase II.

	Atom:Wyck.	As:8h	Cu:4d	O(2):8h	O(1):8g
Phase I	Site symm.	m..	2.22	m..	..2
	x/a	0.16082(4)	1/2	0.1222(3)	0.2022(2)
	y/b	0.20076(5)	0	0.4014(3)	0.7022(2)
	z/c	0	1/4	0	1/4
	↓	↓	↓	↓	↓
	Atom:Wyck.	As:8e	Cu:4d	O(2):8e	O(1):8e
Phase II	Site symm.	1	2..	1	1
	x/a	0.31336(7)	1/2	0.5975(6)	0.2857(7)
	y/b	0.33792(8)	0	0.1415(6)	0.1679(7)
	z/c	0.2395(1)	-0.0279(2)	0.2223(7)	0.0184(7)

the basal plane split into two pairs with a distance difference of ≈ 0.07% at 11.5 GPa. The O(2)-O(2)-O(2) buckling angle along the ribbon-chains is significantly altered and amounts to 158.95° at 11.5 GPa (Figure 5.4). In Phase II, the two As-O(1) bonds which are of equal length in Phase I are split into two separate bonds differing by ≈ 1 %. Additionally, the apex O(1) atoms shift and they are no longer centered above and below the central Cu atoms. Consequently, in Phase II the apex oxygen atoms form zig-zag chains along the c-axis, above and below the CuO_4 basal planes (see Figure 5.6b). At 11.5 GPa, the O(1)-Cu-O(1) angle amounts to ≈ 167° (increased twisting).

As shown in Figure 5.7, there is a significantly larger decrease in the a- and b-axes with pressure as compared to the c-axis compression. The most noticeable effect of the large decrease in the a- and b-axes in Phase I is the substantial reduction of the CuO_6

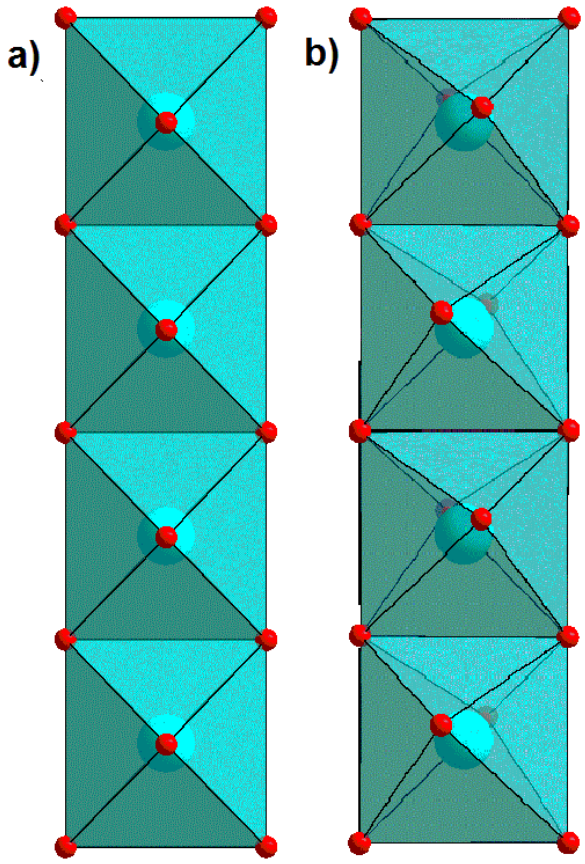

Figure 5.6: **CuO_6 Octahedra Chains.** Projection of the CuO_6 octahedra chains observed in Phase I (a) and Phase II (b) along [110]. The small (red) spheres represent O atoms and the larger (cyan) spheres represent Cu atoms. The deviation from 180° of the O(1)-Cu-O(1) angle formed by the apex oxygen atoms with the Cu atom can be clearly seen in Phase II.

axial elongation. Up to ≈ 7 GPa, the decrease in the axial elongation with pressure is the main source of the compression of the base area, a^2, of the tetragonal cell, see Figure 5.7. The relative change in the Cu-O(1) bond length with pressure coincides with twice the relative change in the lattice parameter a. The Cu-O(1) bond, being the weakest and most compressible bond in the CuO_6 octahedra, is therefore most significantly affected by a reduction of the cell volume. In the pressure regime of 0 to 7 GPa the Jahn-Teller elongation is strongly reduced whereas the Cu bonds to the equatorial O(2) atoms are hardly affected.

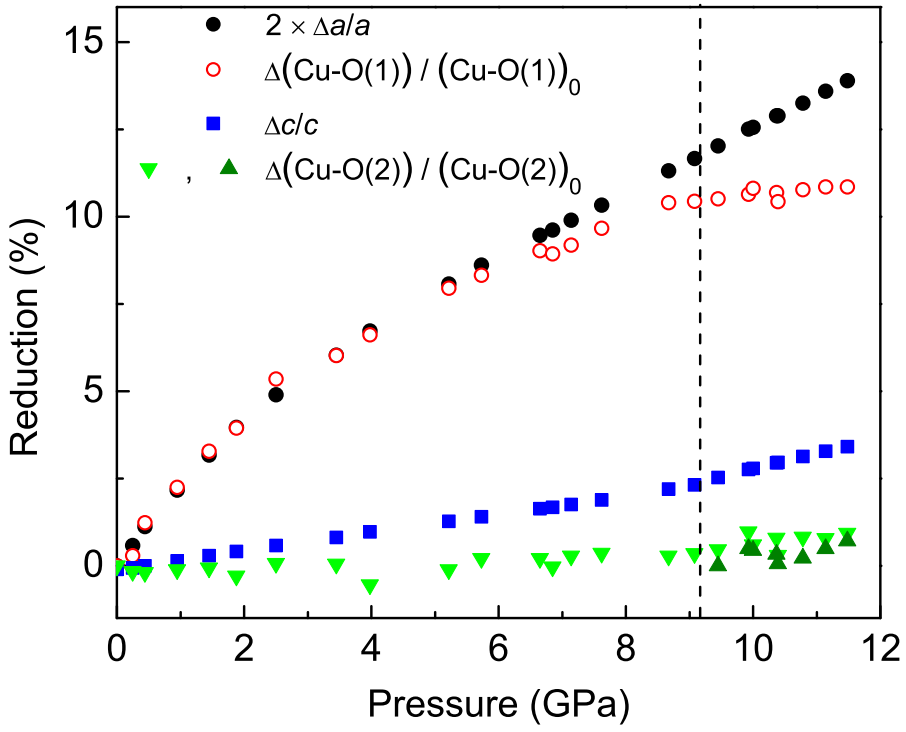

Figure 5.7: **$CuAs_2O_4$ Pressure Induced Reductions.** Plot of the relative changes of various bond distances compared with the decrease of the lattice parameters.

As the pressure is further increased above 7 GPa, the cell volume reduction is no longer controlled by a reduction of the Jahn-Teller elongation. Once this is sufficiently minimized, a structural phase transition occurs. The phase transition involves a

loss of half of the symmetry elements and is most noticeable in the positions of the apex oxygen atoms O(1) and somewhat less of the oxygen atoms in the basal plane. In the structure representation Figure 5.8, the displacements of the apex oxygen atoms is indicated by arrows. All atoms undergo a shift along the tetragonal *c*-axis perpendicular to the *a*-*b* plane. Additionally, the apex oxygen atoms alternately tilt away from the tetragonal axis by a movement in the *a*-*b* plane. Additionally, the buckling angle O(2)-O(2)-O(2), which measures the degree of twisting of the ribbon-chains, reduces continuously with pressure ($\approx 5\%$ at 9 GPa) until the phase transition is reached, see Figure 5.4b. At the phase transition, a glitch is observed in the buckling angle and a further reduction is found in Phase II. In contrast to the bucking angle, the NN bonding angle, Cu-O(2)-Cu, decreasing continuously with pressure and shows no anomaly at the transition from Phase I to Phase II, see Figure 5.4a.

Figure 5.9 presents the decrease in the unit cell volume with pressure. The inset shows the c/a ratio of the tetragonal unit cell. With increasing pressure, the c/a ratio increases and saturates at the phase transition with a value of ≈ 0.67. In order to extract the bulk moduli and their derivatives with respect to pressure, the experimental pressure/volume relationships were fitted to a Vinet equation of state (EoS).[116] The Vinet EoS can be expressed as

$$P = \frac{3\,K_{0,i}(1-x)}{x^2}\exp\left(\frac{3}{2}(K'_{0,i}-1)(1-x)\right), \tag{5.2}$$

where $x = (V_i(P)/V_{0,i})^{1/3}$ with the volumes $V_{0,i}$ for the initial pressure taken for each phase (i = I, II) separately, the bulk moduli $K_{0,i}$ and their derivatives at the initial pressure, $K'_{0,i}$. The fitted parameters are listed in Table 5.3. In the Phase II fit, $K'_{0,2}$ was fixed to a value of 4.

$CuAs_2O_4$ at ambient pressure conditions is isostructural to $FeSb_2O_4$ "Schafarzikite".[117]

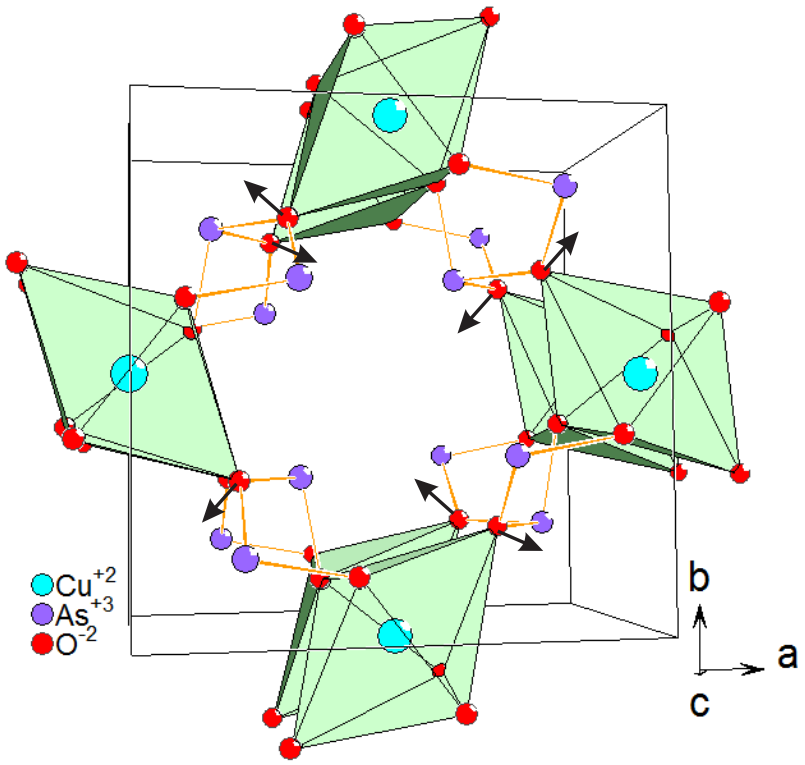

Figure 5.8: **$CuAs_2O_4$ Pressure Induced Atomic Shifts.** $CuAs_2O_4$ structure at ambient pressure. Arrows represent the atom displacements initiated by the transition from Phase I to Phase II.

Table 5.3: **$CuAs_2O_4$ Vinet Equation of State Fit Parameters.** Parameters of the Vinet equation of state (Eq. 5.2) fitted to the pressure/volume data of $CuAs_2O_4$. The derivative of the bulk moduli with respect to pressure, $K'_{0,2}$, was fixed to a value of 4 for Phase II.

Phase	$V_{0,i}$ (Å^3)	$K_{0,i}$ (GPa)	$K'_{0,i}$
I ($<$ 9 GPa)	409.18(5)	36(2)	8.4(8)
II ($>$ 9 GPa)	351.92(9)	66(1)	4

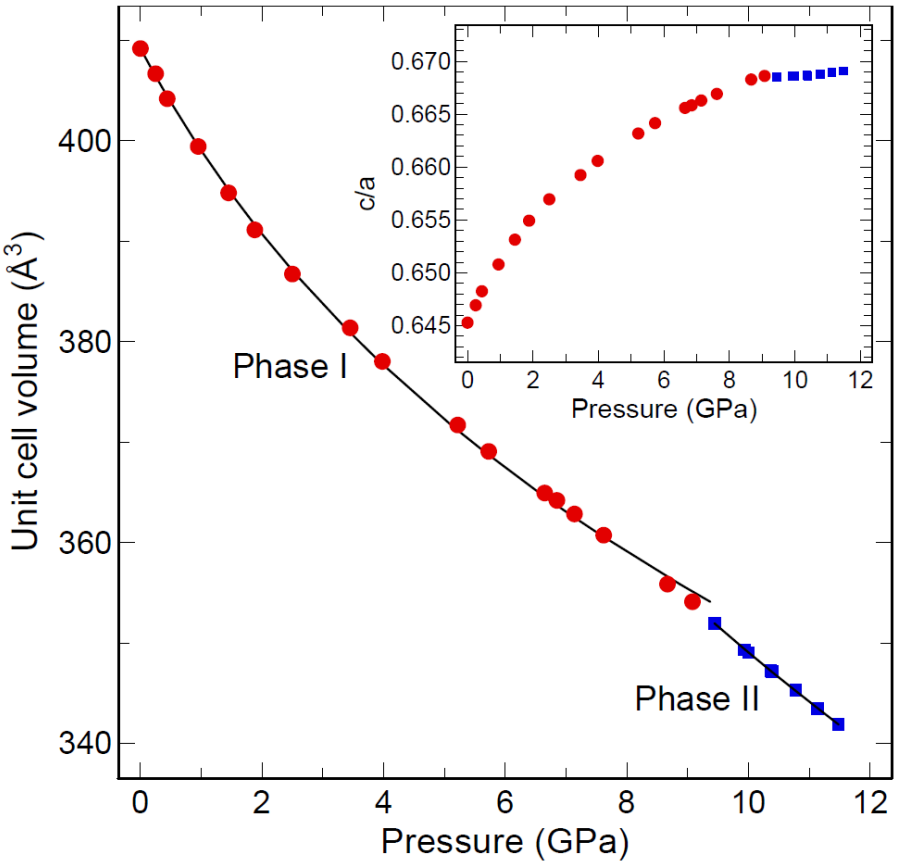

Figure 5.9: **$CuAs_2O_4$ Unit Cell Volume.** $CuAs_2O_4$ unit cell volume reduction with increasing external pressure. The inset displays the ratio of the lattice parameters c/a. The (red) points indicate the lattice parameters in Phase I (spgr. $P4_2/mbc$) and the (blue) points indicate the parameters in Phase II (spgr. $P\bar{4}2_1c$). The (black) solid lines represent the results of the fits to the Vinet equation of state with parameters listed in Table 5.3.

In contrast to $CuAs_2O_4$, $FeSb_2O_4$ undergoes two subsequent structural phase transitions under pressure. From spacegroup $P4_2/mbc$, $FeSb_2O_4$ transforms to $P2_1/c$ at $\approx$ 4 GPa, followed by a transition to $P4_2/m$ at $\approx$ 7 GPa.[118] In the $P4_2/mbc$ phase, the bulk modulus of $FeSb_2O_4$ amounts to 49(2) GPa, somewhat larger than what we find for $CuAs_2O_4$ in Phase I. However, $CuAs_2O_4$ was found to follow an anisotropic compressibility with $K'_{0,1} = 8.4(8)$ for Phase I. Values $K'_0 > 4$ are commonly found for non-isotropic structures reflecting the largely spaced CuO_6 chains in the crystal structure and the lone electron ligand.[67, 118] An analysis of the pressure induced atom displacements in the high pressure phases of $FeSb_2O_4$ reveals very similar movements of the apex oxygen atoms, also forming a zig-zag chain at high pressure, and slight movements of the oxygen atoms in the basal plane. Below 43 K $FeSb_2O_4$ orders with a canted antiferromagnet structure and shows a concomitant magnetoelectric effect.[119–122]

5.3 Evaluation of the Spin-Exchange Constants

The structural changes with pressure in $CuAs_2O_4$ affect both the NN and NNN spin-exchange interactions. The NN exchange angle decreases from 91.5° at ambient pressure to 88.4° at 11.5 GPa as shown in Figure 5.4. This angle decrease results from an increased twisting between two adjacent CuO_4 square planes, which enhances the FM component of the J_{nn} by reducing the overlap between the O $2p$ orbitals (from the magnetic orbitals of the Cu^{2+} sites at the bridging O atoms), see Figure 2.9.[90, 91] In a collaboration with M. Whangbo at North Carolina State University, the spin-exchange parameters for various pressures were calculated using DFT+U_{eff} calculations with the structural parameters determined from the x-ray diffraction results. The same method as employed in the previous chapter for the spin-exchange

parameters of $CuAs_2O_4$ at ambient conditions was followed.[67] The calculations included the NN intrachain exchange, J_{nn}, and the NNN intrachain exchange, J_{nnn}. The calculated spin-exchange parameters are summarized in Table 5.4 for ambient pressure and 11.5 GPa.

Table 5.4: **$CuAs_2O_4$ Phase I & II Spin-Exchange Parameters.** Values of J_{nn} and J_{nnn} obtained from the DFT+U_{eff} calculations. The structural parameters at ambient pressure (Phase I) and at 11.48 GPa (Phase II), given in Table 5.2, were used for the calculations. The Curie-Weiss temperatures obtained using Eq. (4.2) are listed in the rightmost column.

	U_{eff} (eV)	J_{nn} (K)	J_{nnn} (K)	Θ_{CW} (K)
Phase I	0	174.4	-100.7	36.9
	4	154.5	-52.9	50.8
	6	134.8	-39.0	47.9
	8	108.7	-27.5	40.6
Phase II	0	269.1	112.6	190.9
	4	46.5	78.0	62.3
	6	24.3	65.2	44.7
	8	13.3	49.8	31.6

Figure 5.10 shows the J_{nn} and J_{nnn} values (U_{eff} = 8 eV) plotted against pressure. In Phase I, J_{nn} (ferromagnetic) increases with pressure by about 40% whereas J_{nnn} (antiferromagnetic) remains approximately constant. A jump of both spin-exchange constants appears across the structural phase transition at $\approx$ 9.2 GPa when the system transforms into Phase II. In Phase II, J_{nn} drops to a value of approximately 10 K whereas J_{nnn} rises to a larger ferromagnetic value. J_{nnn} reaches $\approx$ 50 K, about five times larger than J_{nn}. We expect the magnetic ordering temperature to decrease as reflected by the drastic drop of J_{nn}.

$\alpha = J_{nn}/J_{nnn}$ is plotted in Figure 5.10 versus pressure. In Phase I, the NNN exchange is AFM with $\alpha \approx$ -4.1 whereas in Phase II, the NNN interactions are FM and dominate the NN spin-exchange (also FM), resulting in $\alpha \approx 0.3$. Effectively, external pressure removes the magnetic frustration from the system and causes the

NNN interactions to become larger than the NN interactions.

5.4 Magnetic Properties Under Hydrostatic Pressure

Magnetization measurements as a function of pressure were carried out to gain insight on how the structural changes and phase transition affect the magnetic properties of $CuAs_2O_4$. Figure 5.11 displays the magnetic ordering temperature, T_C, of $CuAs_2O_4$ versus pressure. In Phase I, a stabilization of the FM groundstate is indicated by an increase of T_C up to ≈ 12 K. This is consistent with the increase of J_{nn} with pressure in Phase I predicted by the DFT calculations. In Phase II, T_C drops to a value of ≈ 7 K signaling an alteration of the magnetic properties. The large drop of J_{nn} predicted by the DFT calculations in Phase II is consistent with the large drop of the measured ordering temperature. To compare the experimental findings with the DFT calculations, the calculate Curie-Weiss temperatures were plotted against the measured ordering temperatures, Figure 5.11. The Curie-Weiss temperatures were calculated with Eq. (4.2) including the NN and NNN intrachain interactions. T_C and θ_{CW} exhibit correlated behaviour across the whole pressure range, irrespective of the transition from Phase I to Phase II. Consequently, the ratio θ_{CW}/T_C ("frustration ratio")[123] is pressure independent and assumes a value of ≈ 5. Although $CuAs_2O_4$ is quasi-one-dimensional and the groundstate ordering is a result of both intrachain and interchain interactions, the intrachain interactions are the dominant interactions and are the essential determining factor for the long-range ordering and the development of the FM groundstate.

Up to the phase transition ($P < 9.2$ GPa) ferromagnetic ordering is observed. In Phase II, the magnetic ordering temperature substantially drops, the details of

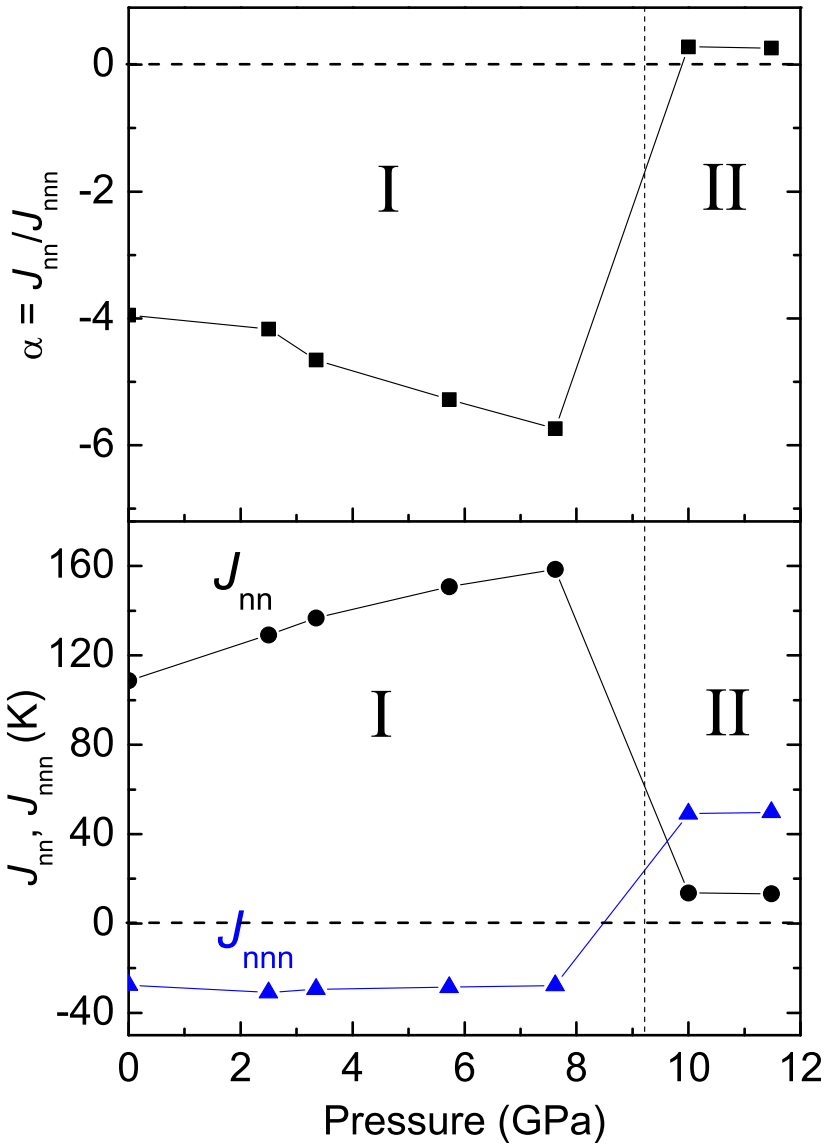

Figure 5.10: **$CuAs_2O_4$ Spin-Exchange Parameters.** Summary of the DFT+U_{eff} calculations depicting how the NN and NNN spin-exchange constants, J_{nn} and J_{nnn}, ($U_{\text{eff}} = 8$ eV) evolve with pressure in Phase I and II.

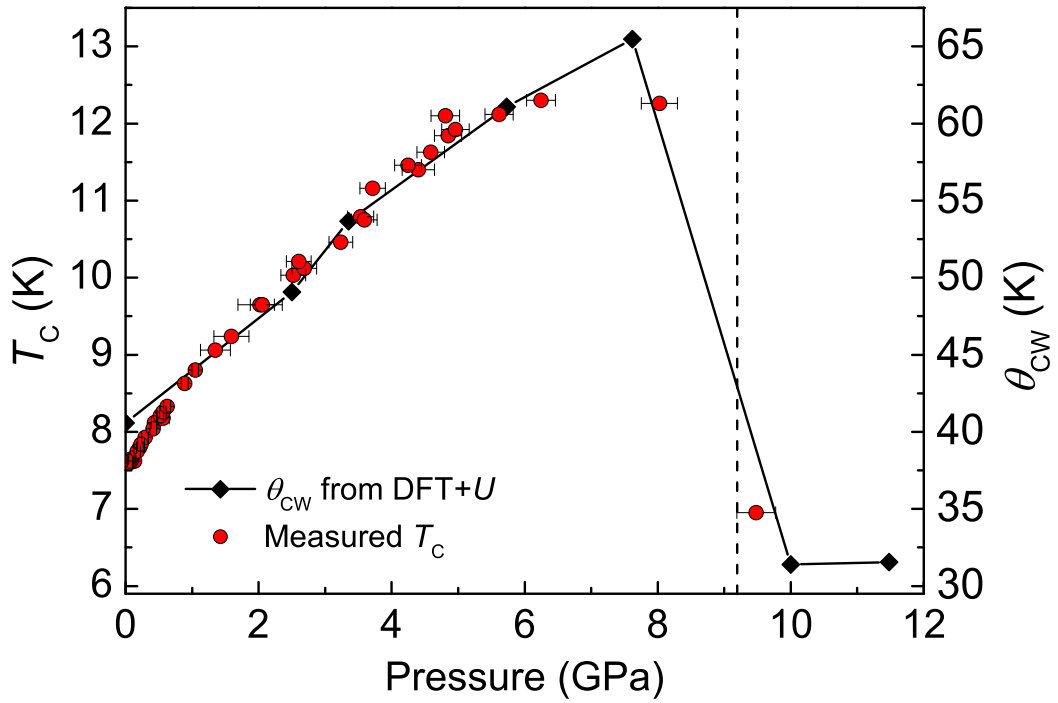

Figure 5.11: **$CuAs_2O_4$ Magnetic Ordering Temperature.** Magnetic ordering temperature of $CuAs_2O_4$ versus pressure.

the long-range ordered state in Phase II are difficult to ascertain due to the large background signal from the diamond anvil cell.

In order to characterize the increase in T_C with unit cell volume in Phase I, a linear relationship to $\Delta T_C(P)$ versus $\Delta v(P)$ was fitted according to

$$\beta = -\frac{\delta \ln(T_C(P))}{\delta \ln(v(P))} \approx -\frac{v(0)}{T_C(0)} \frac{\Delta T_C(P)}{\Delta v(P)}. \tag{5.3}$$

From the fitted results, best agreement was found with $\beta = 6.18(6)$.

5.5 Summary

In summary, I have studied the effect of hydrostatic pressure on the structural and magnetic properties of the quasi-one-dimensional quantum spin-chain ferromagnet,

$CuAs_2O_4$. At ambient pressure, this compound contains CuO_2 ribbon-chains with dominating NN ferromagnetic spin-exchange interactions. The NNN spin-exchange interactions are antiferromagnetic and smaller than the NN spin-exchange by a factor of $\approx$ 4.1. Consequently, $CuAs_2O_4$ represents a rare example of a quantum spin-chain system with competing spin-exchange interactions, in proximity to the quantum critical limit at J_{nn}/J_{nnn}= -4, for which a FM groundstate has been realized. Similar systems with ferromagnetically aligned chains, so far, have been found to order with an AFM groundstate due to interchain interactions.

With the application of hydrostatic pressure, synchrotron x-ray diffraction results revealed a large suppression of the axial Jahn-Teller elongations of the oxygen octahedra surrounding the Cu^{2+} cations. Raman spectroscopy identified a structural phase transition which led to a new ribbon-chain structure. Magnetic susceptibility measurements found that the structural phase transition was accompanied by a severe alteration of the magnetic properties. Before the phase transition, a stabilization of the FM groundstate was indicated by a continuous increase of the magnetic ordering temperature. The phase transition induced a notable change of the magnetic properties which was signaled by a dramatic drop in the ordering temperature. It was shown that hydrostatic pressure alters $\alpha = J_{nn}/J_{nnn}$ from $\approx$ -4.1 at ambient pressure to $\approx$ 0.3 at 11.5 GPa, effectively removing the magnetic frustration.

In conclusion, the described investigations demonstrate that it is possible to reach new magnetic groundstates in ribbon-chain systems through the application of external pressure. Similar investigations could be carried out on other ribbon-chain compounds and may lead to the realization of unique magnetic groundstates such as helical ordering and possibly multiferroicity.

6

Copper Antimonite - $CuSb_2O_4$

In this chapter, I will discuss the magnetic and structural properties of the S=1/2 quasi-one-dimensional antiferromagnet $CuSb_2O_4$. The motivation to investigate this compound came from its chemical relation and similar crystal structure to $CuAs_2O_4$. Both compounds belong to the $CuM_2^{3+}O_4$ (M = 3+ metalloid) family with tetragonal crystal structures. Both compounds contain CuO_2 ribbon-chains located in the basal planes of linking CuO_6 octahedra. However, the Jahn-Teller elongations of the octahedra in $CuSb_2O_4$ are much weaker than in $CuAs_2O_4$ at ambient pressure but similar to those found in $CuAs_2O_4$ in the high-pressure structure. Similarly to $CuAs_2O_4$, $CuSb_2O_4$ exhibits FM-NN and AFM-NNN spin-exchange interactions within the spin-chains. Despite the large number of similarities, $CuAs_2O_4$ and $CuSb_2O_4$ are magnetically very different. $CuAs_2O_4$ orders in a FM groundstate with $\alpha = J_{\mathrm{nn}}/J_{\mathrm{nnn}} \approx$ -4.1, placing it in the "Ferromagnetic" regime of the phase diagram, Figure 2.7. In the high-pressure structure (11.5 GPa), $CuAs_2O_4$ displays $\alpha = 0.3$, still placing it in the "Ferromagnetic" regime. $CuSb_2O_4$ orders in an incommensurate AFM groundstate with α = -1.8 and is located in the "Highly Frustrated" regime, see Figure 2.7.

A reflux reaction synthesis procedure for $CuSb_2O_4$ was reported in detail by Focke *et al.*[124] in 2013. A preliminary investigation of the structural and magnetic properties of $CuSb_2O_4$ was carried out by Atanasova *et al.* [125] in 2014. The authors

reported a crystal structure solution, Raman spectroscopy measurements, and found antiferromagnetic ordering below 1.8 K according to magnetic susceptibility and heat capacity measurements. In this thesis work, I have confirmed the x-ray diffraction and Raman spectroscopy results and extended the magnetic investigations down to 700 mK for the magnetic susceptibility and 400 mK for the heat capacity. Using the low-temperature heat capacity and magnetization results, I constructed a (T, H) magnetic phase diagram. Additionally, I characterized the magnetic structure using neutron diffraction and found indications of ferroelectricity with dielectric capacitance measurements.

6.1 Sample Characterization

A polycrystalline powder sample of $CuSb_2O_4$ had been previously prepared and gratefully provided by the authors of Ref. [125]. The sample was prepared by reacting antimony trioxide with a copper-ammonium complex in a reflux synthesis method.[124, 125] This synthesis procedure involves mixing ammonia solution with dicopper carbonate dihydroxide (the natural mineral Malachite) and antimony trioxide. The mixture was stirred with a reflux temperature of 70 °C with cooling water to prevent ammonia from escaping. After 15 hours, the cooling water was removed and the ammonia was evaporated. $CuSb_2O_4$ powder was recovered from the remaining solution by filtration. For further details on the synthesis of $CuSb_2O_4$, refer to references [124, 125].

X-ray diffraction measurements with Mo $K\alpha_1$ radiation (λ = 0.70932 Å) were performed to evaluate the phase purity and crosscheck the crystal structure with previously published results.[125] Figure 6.1 displays the x-ray diffraction pattern (red data points) along with a single phase Rietveld refinement fitted using FullProf

Suite software.[68] The fit is represented as a black line, the difference between the fit and the measured data is shown as a blue line, and the green vertical dashes indicate the Bragg positions. The profile refinement shows that the sample is of very good quality with only one impurity peak appearing at $\approx 25.5°$ ($d = 0.8238$ Å) and consistent with the previously reported data.[125] The impurity could not be identified from a single diffraction peak but is investigated further with the magnetic susceptibility measurements.

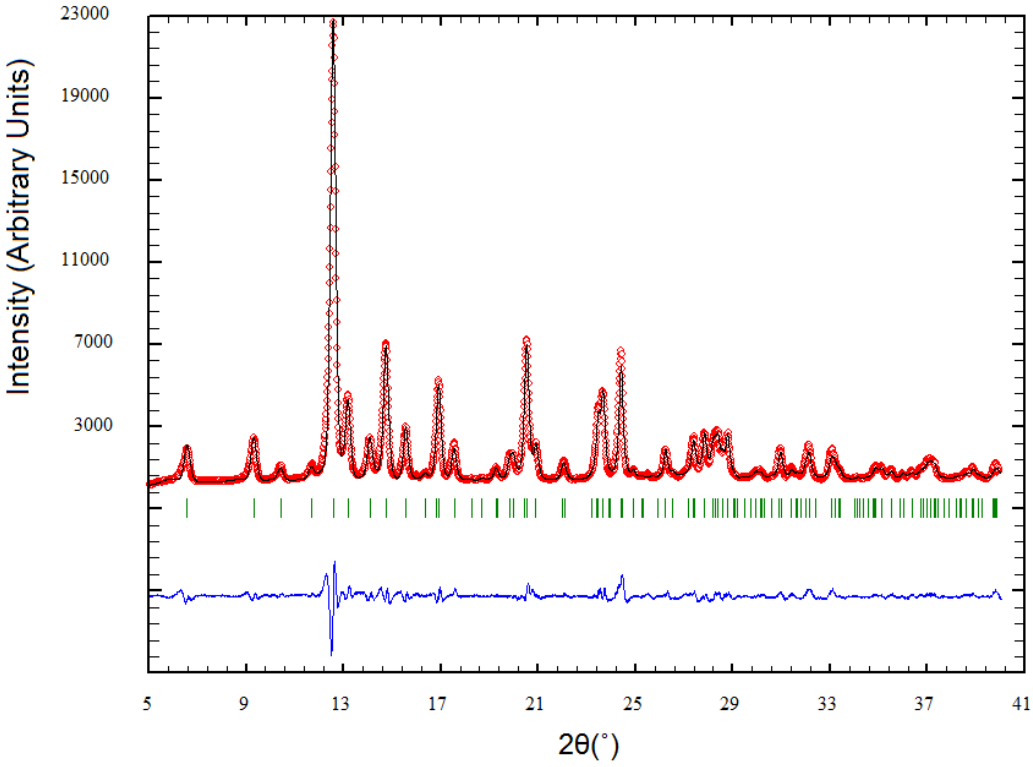

Figure 6.1: **$CuSb_2O_4$ X-ray Diffraction.** A Mo x-ray diffraction pattern of a $CuSb_2O_4$ polycrystalline sample (red circles). The single phase Rietveld fit (black line) to the pattern was calculated using FullProf Suite software. The green vertical dashes represent the Bragg reflections used to simulate the pattern. The difference between the measured pattern and calculated fit is shown as the blue line.

Table 6.1: **$CuSb_2O_4$ Refined Structural Parameters.** Refined positional parameters of $CuSb_2O_4$ from a Rietveld profile refinement of x-ray diffraction data. The tabulated parameters for were refined in space group $P4_2bc$ (no. 106) with lattice parameters $a = 8.7396(3)$ Å and $c = 5.7853(3)$ Å. The agreement indicies were Bragg R-factor = 2.61 and RF-factor = 2.49.

Atom:Wyck.	Sb:8c	Cu:4b	O(2):8c	O(1):8c
Site symm.	1	2..	1	1
x/a	0.1863(2)	0	0.413(1)	0.714(1)
y/b	0.1533(7)	1/2	0.122(1)	0.175(1)
z/c	-0.27(2)	0.48(1)	-0.227(1)	0.490(1)

6.2 Crystal Structure

$CuSb_2O_4$ crystallizes with a tetragonal structure and space group $P4_2bc$, see Figure 6.2.[125] The fitted lattice parameters amounted to $a = b = 8.7396(3)$ Å and $c = 5.7853(3)$ Å. The Cu^{2+} ions are positioned on Wyckoff sites 4b and the Sb^{3+} ions are located on sites 8c. Both the O(1) (apical oxygen) and O(2) (basal oxygen) atoms are located on sites 8c. Similar to $CuAs_2O_4$, the Cu^{2+} ions are centered in O_6 octahedra which experience Jahn Teller distortions. These distortions elongate the Cu-O(1) bonds such that the distances are $2 \times 2.45(1)$ Å and the basal plane Cu-O(2) distances are $2 \times 1.877(4)$ Å and $2 \times 2.073(4)$ Å. The CuO_6 octahedra link together via opposite edges to form infinite chains and give rise to the CuO_2 ribbon-chains within the basal planes. Neighbouring CuO_6 chains are nearly orthogonally oriented and connected via $SbO_3{}^{3-}$ groups.

$CuSb_2O_4$ and $CuAs_2O_4$ exhibit very similar crystal structures, the most noticeable difference between the them is found in distortions of the O_6 octahdra around the Cu^{2+} ions. The apical O(1) ions in $CuAs_2O_4$ are located exactly above and below the central Cu ion such that the O(1)-Cu-O(1) angle is 180°. In the $CuSb_2O_4$ structure, the apical O(1) atoms form zig-zag chains above and below the octahedra basal planes such that the O(1)-Cu-O(1) angle amounts to 172.04°. Consequently,

the crystal structure of $CuSb_2O_4$ is more similar to the high-pressure crystal structure of $CuAs_2O_4$ which was found to have a O(1)-Cu-O(1) angle of 167.04° at 11.5 GPa.

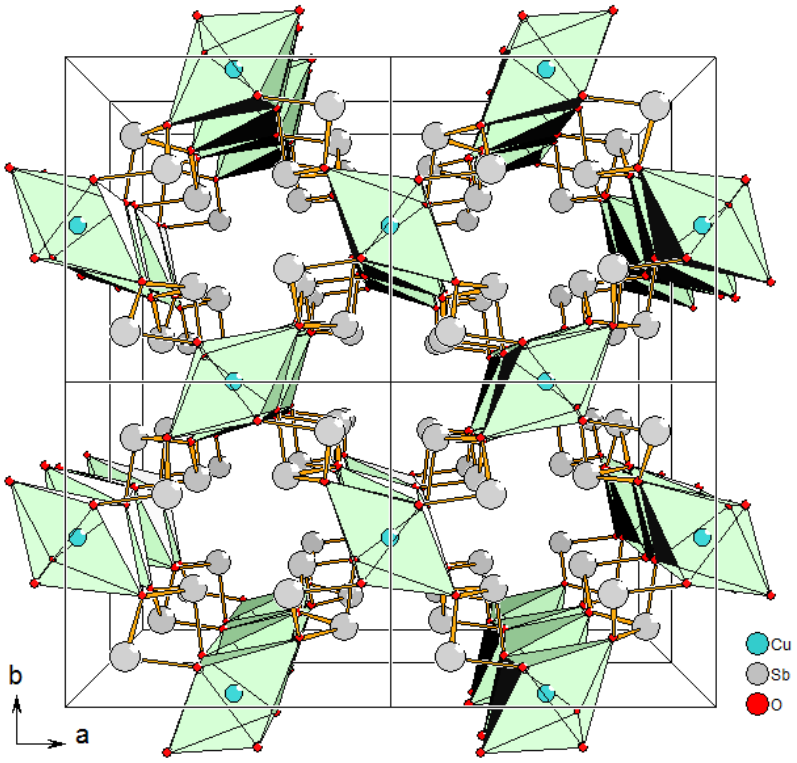

Figure 6.2: **$CuSb_2O_4$ Crystal Structure.** Projection along [001] of the $CuSb_2O_4$ crystal structure. The Cu^{2+} atoms are represented by the green spheres, the oxygen atoms by red spheres, and the Sb atoms by gray spheres.

6.3 Raman Spectroscopy

Raman spectroscopy measurements were performed on a polycrystalline powder sample of $CuSb_2O_4$ at room temperature, Figure 6.3. The pattern is consistent with the previously published data.[125] A comparison of the Raman peak positions measured in this work with those calculated and measured by Atanasova *et al.* [125] is given in Table 6.2.

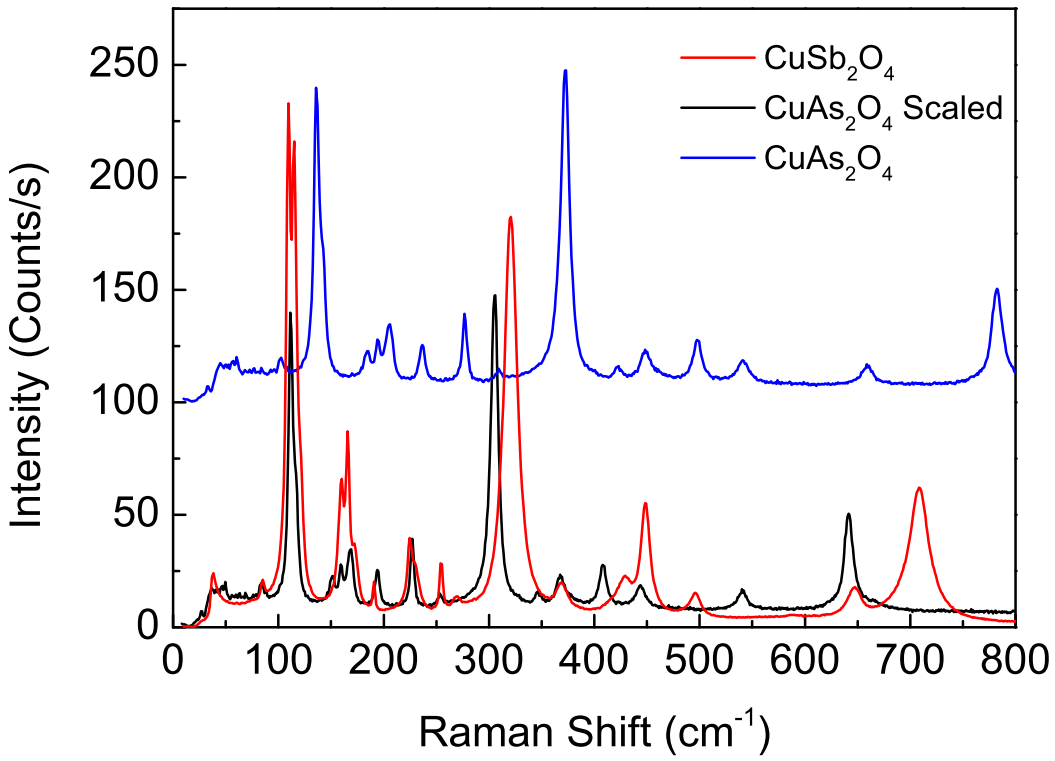

Figure 6.3: **$CuSb_2O_4$ Raman Diffraction.** The room temperature Raman spectrum of $CuSb_2O_4$ collected on a polycrystalline powder is shown as the black curve. The red curve is the $CuAs_2O_4$ with the Raman shift multiplied by a factor of 0.82. The blue curve is the unscaled Raman Spectrum of a $CuAs_2O_4$ powder sample for comparison (offset for clarity).

Table 6.2: **$CuSb_2O_4$ Raman Active Modes.** Comparison of the measured $CuSb_2O_4$ Raman peak positions with those measured and calculated by Atanasova *et al.*[125]. The notation n.r. indicates a peak which was not reported.

Symmetry	Calculated [125] (cm^{-1})	Atanasova[125] (cm^{-1})	This Work (cm^{-1})
B_1	44.3	36	38.3
A_1	93.8	n.r.	84.8
E	111.6	110	109.4
B_1	121.3	115	114.9
B_2	121.7	120	120.5
B_1	160.9	161	160.0
B_2	161.9	166	165.8
E	186.5	173	172.2
E	207.3	n.r.	190.7
E	218.9	n.r.	224.9
B_1	221.6	225	229.0
n.r.	n.r.	n.r.	254.6
n.r.	n.r.	n.r.	269.3
E	331.3	322	320.6
B_1	358.8	n.r.	369.4
E	436.1	430	429.5
E	470.9	451	448.7
B_2	485.6	497	496.1
E	589.8	589	589.6
A_1	648.3	650	647.2
E	705.9	709	708.5

To compare the $CuSb_2O_4$ spectra with the $CuAs_2O_4$ spectra, additional Raman spectroscopy measurements were performed on a powder sample on $CuAs_2O_4$ at room temperature. The spectra for both compounds are displayed in Figure 6.3. The difference in Raman peak positions between $CuSb_2O_4$ and $CuAs_2O_4$ can be largely attributed to the difference in mass between the Sb ion ($m_{Sb} \approx 121$ u) and the As ion ($m_{As} \approx 75$ u). In the view of a simple harmonic oscillator with the assumption that the force constants for both compounds are the same, the Raman frequencies below ≈ 400 cm^{-1} of the two compounds can be related by:

$$\omega_{Sb} = \sqrt{\frac{m_{As}}{m_{Sb}}}\omega_{As}. \tag{6.1}$$

From this equation, $\omega_{Sb} \approx 0.8\omega_{As}$. For wavenumbers below ≈ 400 cm^{-1}, the phonon densities of states is dominate by contributions from the Cu and As (Sb) vibrations, see Figure 4.4. The higher wavenumbers are dominated by contributions from the oxygen ions. As shown in Figure 6.3, the Raman spectrum of $CuAs_2O_4$ scaled by 0.82 matches well with the Raman spectrum of $CuSb_2O_4$ for wavenumbers below 400 cm^{-1}.

6.4 Spin-Exchange Interactions

DFT+U_{eff} calculations have been performed[1] for the NN and NNN intrachain spin-exchange parameters of $CuSb_2O_4$. The calculations were carried out following the same method used for $CuAs_2O_4$ described in detail above for the three ordered spin states shown in Figure 6.4. The results of the DFT+U_{eff} calculations along with the Curie-Weiss temperatures calculated using Eq. 4.2 are displayed in Table 6.3.

[1]The DFT calculations have been gratefully performed by M. Whangbo and collaborators at North Carolina State University.

Table 6.3: **$CuSb_2O_4$ Spin-Exchange Parameters.** Values of the NN and NNN spin exchange constants, J_{nn} and J_{nnn}, respectively, obtained from the DFT+U_{eff} calculations. The calculated Curie-Weiss temperatures from the spin-exchange constants are also listed.

U_{eff} (eV)	J_{nn} (K)	J_{nnn} (K)	Θ_{CW} (K)
2	156.7	-121.8	17.5
4	140.4	-88.2	26.1
6	117.2	-63.8	26.7

The results reveal that the NN interactions are FM and dominate while the weaker NNN interactions are AFM, similar to what was found for $CuAs_2O_4$. The resulting spin-exchange parameters imply strong intrachain magnetic frustration. The ratio of the two spin-exchange interactions (U_{eff} = 6 eV) amounts to $\alpha = J_{nn}/J_{nnn} \approx$ -1.8. This places $CuSb_2O_4$ in the "Highly Frustrated" regime of the magnetic phase diagram (Figure 2.7).

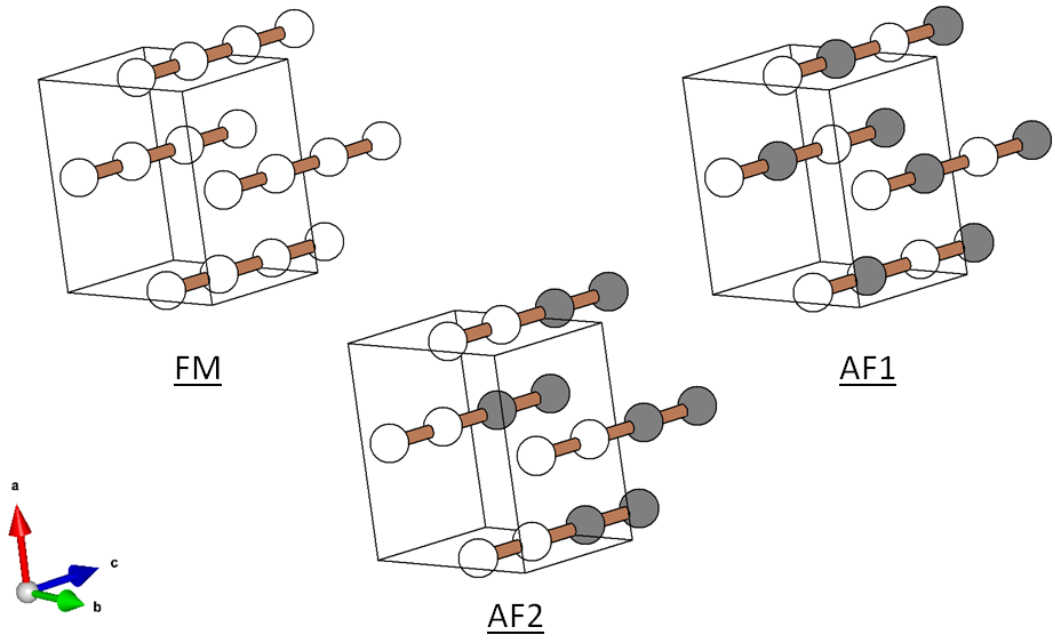

Figure 6.4: **$CuSb_2O_4$ Ordered Spin States.** The ordered spin states are created with a 1a × 1b × 2c supercell. Shaded and unshaded spheres represent down-spin and up-spin configurations.

It was observed that α amounts to -4.1 for $CuAs_2O_4$ at ambient pressure and $\alpha = 0.3$ in the high-pressure structure. The large difference in α values between $CuSb_2O_4$ and $CuAs_2O_4$, two compounds which contain very similar crystal structures, can be largely attributed to the difference in the Cu-O(2)-Cu super-exchange bonding angles. As shown in Figure 2.9, the NN spin-exchange interactions (and α) are highly sensitive to the super-exchange angle, minute corrugations in the CuO_2 ribbon-chains due to three-dimensional bonding or structural distortions appear to have a large effect on $J_{\rm nn}$. $CuAs_2O_4$ exhibits a Cu-O(2)-Cu super-exchange of $\approx 91^\circ$ ($\approx 88.5^\circ$ at 11.5 GPa) while $CuSb_2O_4$ displays a super-exchange angle of $\approx 94.3^\circ$. The transition between the FM regime and the Highly Frustrated regime of the groundstate phase diagram appears to occur at an angle of $\approx 91.5^\circ$, see Figure 2.9.

$CuSb_2O_4$ exhibits long-range magnetic order below $T_{\rm N} \approx 1.8$ K. The magnetic ordering temperature allows for an estimation of the order of magnitude of the interchain interactions. For an antiferromagnetic Heisenberg spin-chain system, the interchain interactions can be estimated with the following equation[99, 100]:

$$J_{\rm inter} \sim T_{\rm N}\frac{\pi}{2}\left(\ln(5.8 \times J_{\rm nn}/T_{\rm N})\right)^{-1/2} \tag{6.2}$$

Using $J_{\rm nn} = 117$ K and $T_{\rm N} = 1.8$ K, the interchain spin-exchange interactions in $CuSb_2O_4$ were estimated to be ~ 7 K, two orders of magnitude smaller than $J_{\rm nn}$.

6.5 Magnetic Susceptibility and Magnetization

The magnetic susceptibility of $CuSb_2O_4$ was measured for a temperature range of 0.7 K to 375 K in a magnetic field of 0.01 T. To reach temperatures below 1.8 K, a home-built ^{3}He cooling system was used with the MPMS.[80]

The low temperature susceptibility, $T < 1.6$ K, was dominated by a "Curie tail",

a paramagnetic increase in the susceptibility due to small paramagnetic impurities in the sample (mentioned in the x-ray diffraction results). By fitting a Curie-Weiss law to the low temperature susceptibility, the "Curie tail" could be removed from the total susceptibility. The impurity susceptibility, $\chi_{\rm imp}(T)$, was fitted using:

$$\chi_{\rm imp}(T) = P \times \frac{C}{T} \tag{6.3}$$

Where $C = 0.375153$ Kcm^3/mol for $S = 1/2$ entities with a g-factor of 2 and P is the prefactor which amounts to the percentage of impurity in the total sample. The best fit was achieved with $P = 0.6(1)\%$ indicating that the paramagnetic impurity amounts to less than 1% of the sample. At ≈ 1 K, a kink is seen in the magnetic susceptibility data which is also attributed to the small amount of impurity since no anomaly is seen in the heat capacity or neutron diffraction data near this temperature (see below).

Figure 6.5 displays the $CuSb_2O_4$ magnetic susceptibility curve below 12 K with the Curie-tail subtracted. A broad maximum is seen at ≈ 7 K attributed to antiferromagnetic short-range correlations. The onset of long-range antiferromagnetic ordering occurs at $T_{\rm N} \approx 1.8$ K indicated by a dashed line in Figure 6.5. The high temperature ($T > 150$K) data was fitted to a Curie-Weiss law as described in Eq. (4.4). The best fit was achieved with a g-factor of

$$g = 2.10(1),$$

a Curie-Weiss temperature of

$$\theta_{\rm CW} = +26.3(2)\text{K},$$

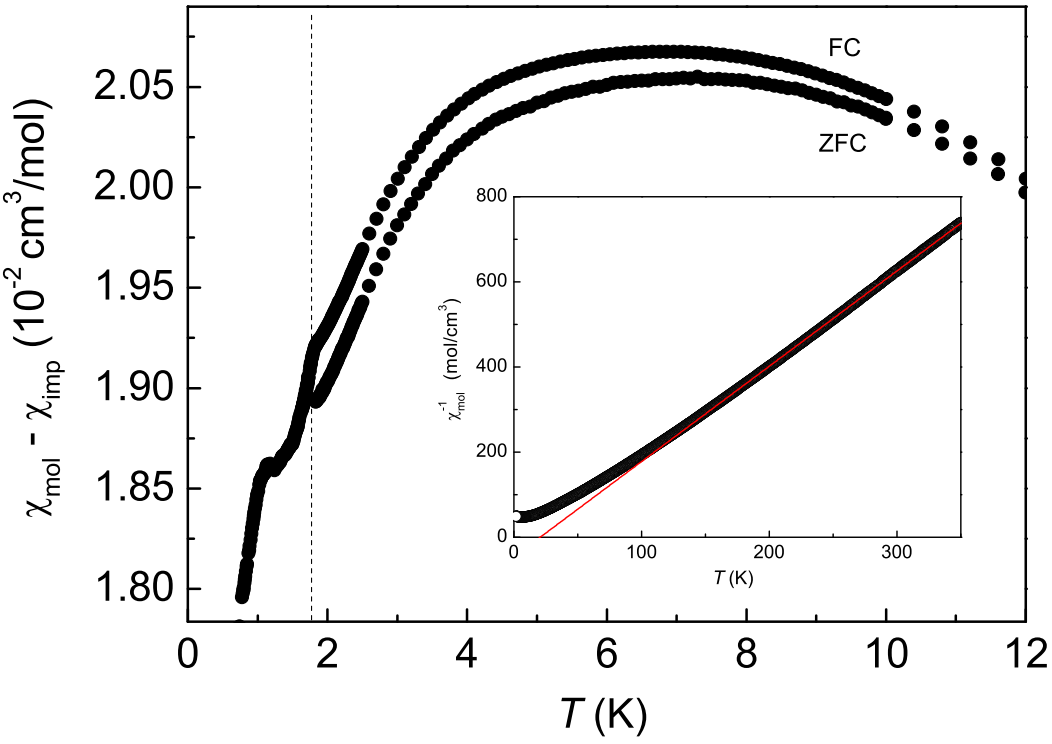

Figure 6.5: **$CuSb_2O_4$ Magnetic Susceptibility.** Field cooled (FC) and zero-field cooled (ZFC) magnetic susceptibility curves of $CuSb_2O_4$ measured on a polycrystalline powder sample with a magnetic field of 0.01 T. The dashed line represents the ordering temperature of $CuSb_2O_4$. The inset shows the inverse susceptibility fitted with an inverse Curie-Weiss function.

and a temperature independent offset of

$$\chi_0 = 25.2(1) \times 10^{-6}\text{cm}^3/\text{mol}.$$

The fitted g-factor agrees well with the measured value from the EPR results (see below) and is also similar to the g-factor found for $CuAs_2O_4$. The positive Curie-Weiss temperature value indicates dominate FM spin-exchange interactions consistent with the DFT calculations. The value of the Curie-Weiss temperature is close to the calculated value from the DFT calculations given in Table 6.3.

The diamagnetic temperature independent contribution, χ_{Dia}, was estimated to be -93 $\times$ 10^{-6} cm^3/mol from the tabulated values of individual ions.[103] The total temperature independent contribution to the magnetic susceptibility was determined to be $\chi_0 = \chi_{\text{Dia}} + \chi_{\text{VV}} \approx 25 \times 10^{-6}$ cm^3/mol. This indicates a van Vleck susceptibility of $\approx 118 \times 10^{-6}$ cm^3/mol, in the expected range for a Cu^{2+} system.[31, 104, 105] Refer to Appendix A for more details.

In a collaboration with J. M. Law from the Dresden Hochfeld-Magnetlabor (Dresden, Germany), pulsed high-field magnetization measurements were performed on $CuSb_2O_4$ up to 60 T. Figure 6.6 displays the magnetization measurements for various temperatures between 1.5 K and 5 K. The inset displays the first derivative of the magnetization with applied field. Magnetic saturation for $CuSb_2O_4$ was observed at $\approx$ 14 T. Additionally, indications of a spin-flop transition can be seen at $\approx$ 5 T (investigated further in a following chapter). The dotted red line in Figure 6.6 is a calculated magnetization curve reported in Ref. [126] for a S=1/2 Heisenberg AFM chain with NN and NNN spin-exchange interactions and α = -2. Best agreement with the experimental data was found with J_{nnn} = -20.5 K. This value is somewhat lower than what was found from DFT calculations, however, it has been found for similar

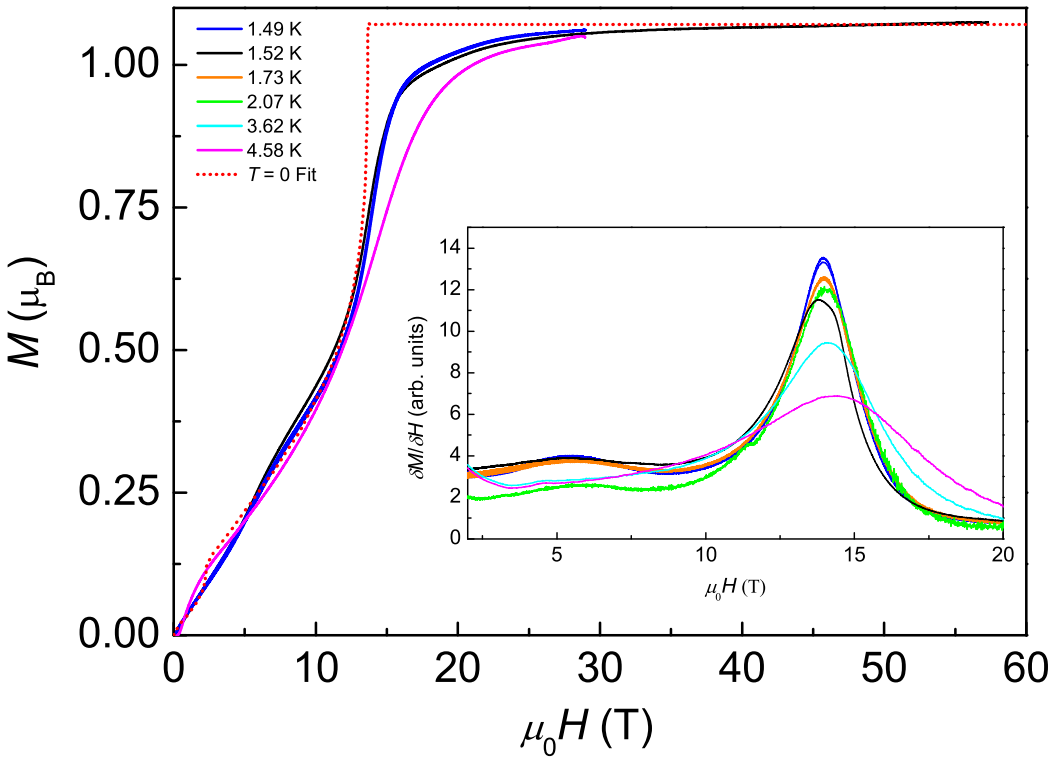

Figure 6.6: **$CuSb_2O_4$ High-Field Magnetization.** The magnetization curve of $CuSb_2O_4$ measured on a polycrystalline sample with pulsed magnetic fields at various temperatures as indicated. The onset of magnetic saturation can be seen at $\approx$ 14 T. The calculated magnetization for an AFM Heisenberg chain with J_{nnn} = -20.5 K and α = -2 is represented as the dotted line. The inset shows the magnetic field derivative of the magnetization.

ribbon-chain systems that DFT calculations produce the correct $\alpha = J_{\rm nn}/J_{\rm nnn}$ values but overestimate the absolute spin-exchange parameters.[31, 64]

6.6 Heat Capacity

Heat capacity measurements were performed on a powder sample of $CuSb_2O_4$ versus temperature and magnetic field. The heat capacity data for 0, 3, 6, and 9 T are shown in Figure 6.7. In zero-field, a λ-shaped anomaly is clearly visible at

$$T_{\rm N} = 1.81 \pm 0.1{\rm K},$$

in agreement with what was found in the magnetic susceptibility. With the application of a magnetic field, the anomaly broadens and shifts in temperature. The peak position of the anomaly differs for various fields indicating multiple magnetic phases, a detailed magnetic phase diagram for $CuSb_2O_4$ is described below. Note that no anomaly is seen at ≈ 1 K, as was seen in the magnetic susceptibility, supporting that the 1 K transition is due to the small amount of impurities.

6.7 Neutron Diffraction

Elastic neutron powder diffractions experiments were carried out on the D20 beamline at the Insititute Laue-Langevin (Grenoble, France). Diffraction patterns were collected with a wavelength of $\lambda = 2.41$ Å at temperatures above and below $T_{\rm N}$. In the magnetically ordered phase, weak magnetic Bragg reflections were detected at the low angular parts of the diffraction patterns. A comparison of two diffraction patterns collected at 432 mK and 3 K is shown in Figure 6.8. Additional magnetic scattering below $2\theta \approx 60^\circ$ can be seen and is indicated by arrows in Figure 6.8. Due

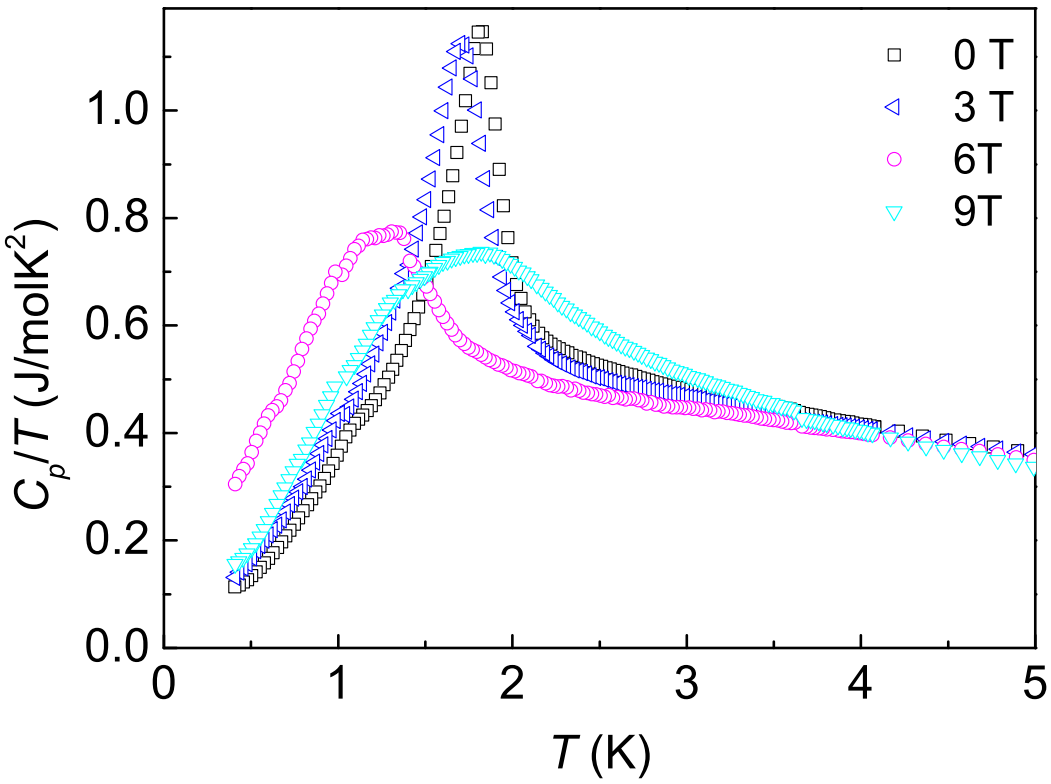

Figure 6.7: **$CuSb_2O_4$ Heat Capacity.** The heat capacity of a polycrystalline powder of $CuSb_2O_4$ versus temperature and magnetic field.

to the relatively weak magnetic moment of Cu^{2+} ($\mu \lesssim 1\ \mu_B$), the intensity of the magnetic Bragg reflections ($\propto \mu^2$) was small. To obtain a pattern of only magnetic Bragg reflections of the long range ordered state, the nuclear reflections were removed by subtracting the 3 K pattern from the 423 mK pattern. The resulting magnetic diffraction pattern is shown in Figure 6.9.

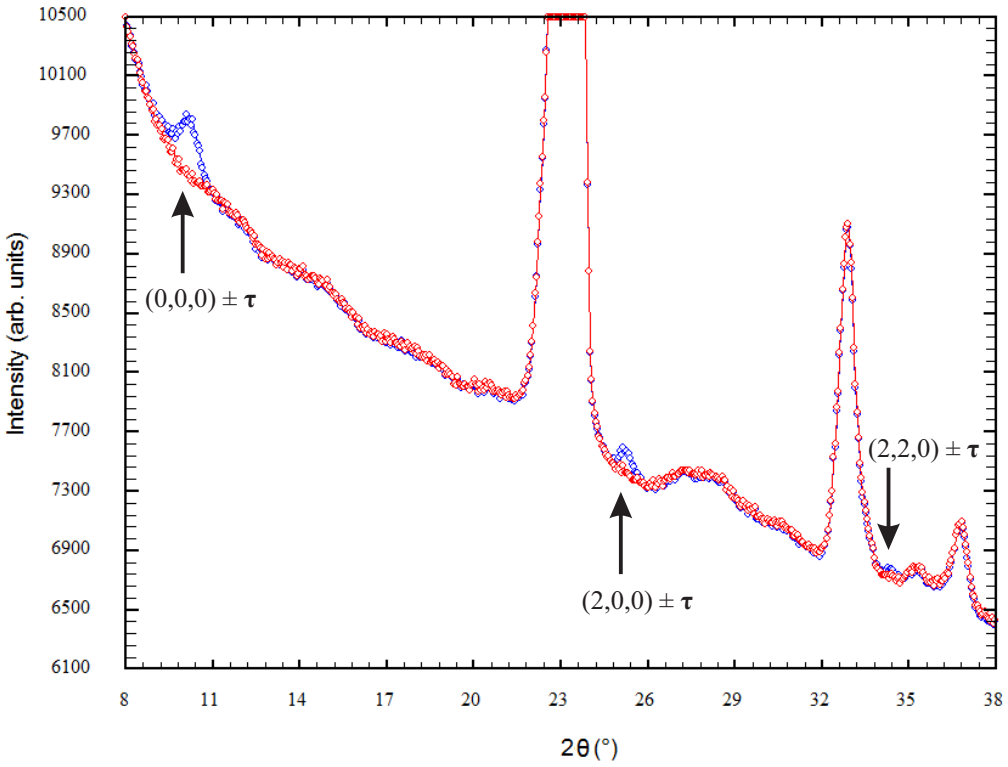

Figure 6.8: **$CuSb_2O_4$ Neutron Diffraction.** Two neutron diffraction patterns of $CuSb_2O_4$ taken at 432 mK (blue data points) and 3 K (red data points). Additional weak magnetic Bragg reflections are visible and indicated by black arrows.

A Rietveld profile refinement was used to analysis the magnetic diffraction pattern using FullProf Suite software.[68] A nuclear structure profile refinement was performed on the 3 K diffraction pattern to obtain accurate nuclear, profile, and scale parameters which were used for the subsequent refinement of the magnetic diffraction pattern. A

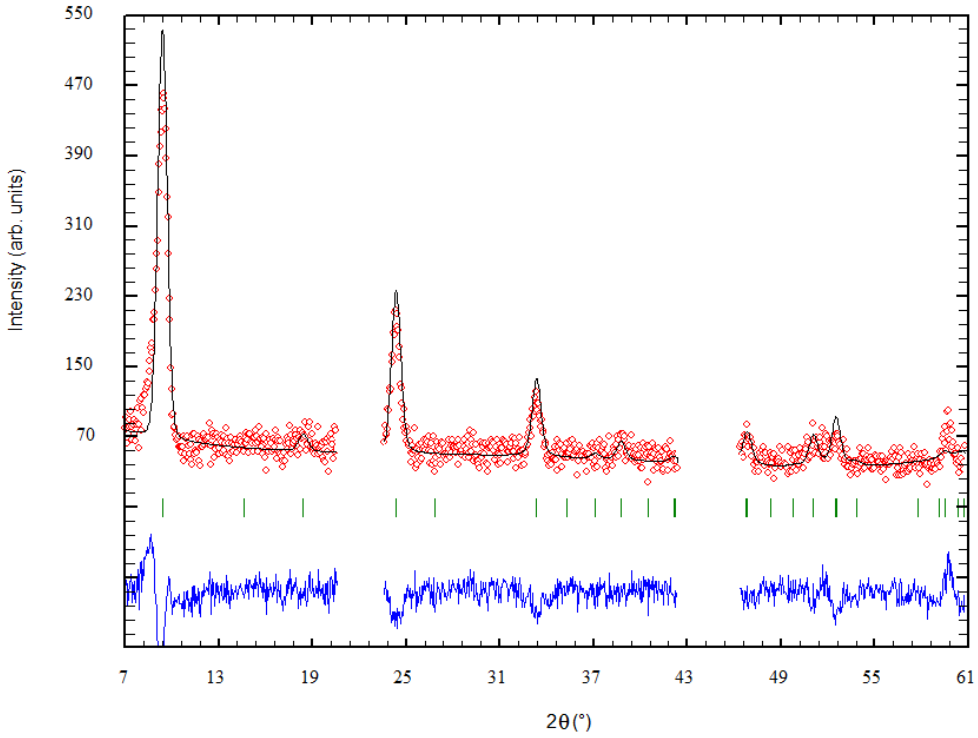

Figure 6.9: **$CuSb_2O_4$ Magnetic Diffraction Pattern.** Neutron diffraction pattern of the magnetic Bragg reflections of $CuSb_2O_4$ at 432 mK. The pattern was obtained by taking the difference between diffraction patterns at 432 mK (below T_N) and 3 K (above T_N). The experimental data (red circles) are plotted with a profile refinement (black line) and Bragg reflections used in the simulation (green bars). The difference between the simulated and measured data is shown as the blue line.

profile refinement of the magnetic diffraction pattern provided the propagation vector and magnetic structure. The refinement converged to a magnetic moment at 432 mK of $\mu = 0.52(1)\ \mu_{\mathrm{B}}$. All magnetic Bragg reflections at 432 mK could be indexed with an incommensurate propagation vector

$$\boldsymbol{\tau} = \big(0, 0, 0.3962(1)\big).$$

This indicates an incommensurate AFM ordering with the moments oriented in a helicoidal spiral along the c-axis direction (along the spin-chains), see Figure 6.10. The magnetic unit cell is approximately 2.5 times the length of the nuclear cell in the c-axis direction.

The most intensive magnetic Bragg reflection is centered at $2\theta \approx 10^{\circ}$, indexed as (0,0,0) $\pm\ \boldsymbol{\tau}$. In order to obtain the temperature dependence of this magnetic Bragg reflection, a series of diffraction patterns between 432 mK and 2 K were collected. The difference between the series of collected patterns below 2 K and the 3 K pattern was fitted and the integrated intensities are plotted versus temperature in Figure 6.11. The temperature dependence of the integrated intensities were fitted to a critical power law according to:

$$I(T) = I_0(1 - T/T_{\mathrm{N}})^{2\beta}, \tag{6.4}$$

where I_0 is the $T = 0$ K intensity and β is the magnetization critical exponent. The fit converges to a magnetic ordering temperature $T_{\mathrm{N}} = 1.95(2)$ and a critical exponent $\beta = 0.33$. The fitted ordering temperature is slightly higher than that found in the magnetic susceptibility and heat capacity data. The fitted critical exponent β for the magnetization is consistent with values for the $3d$-Heisenberg standard universality class.

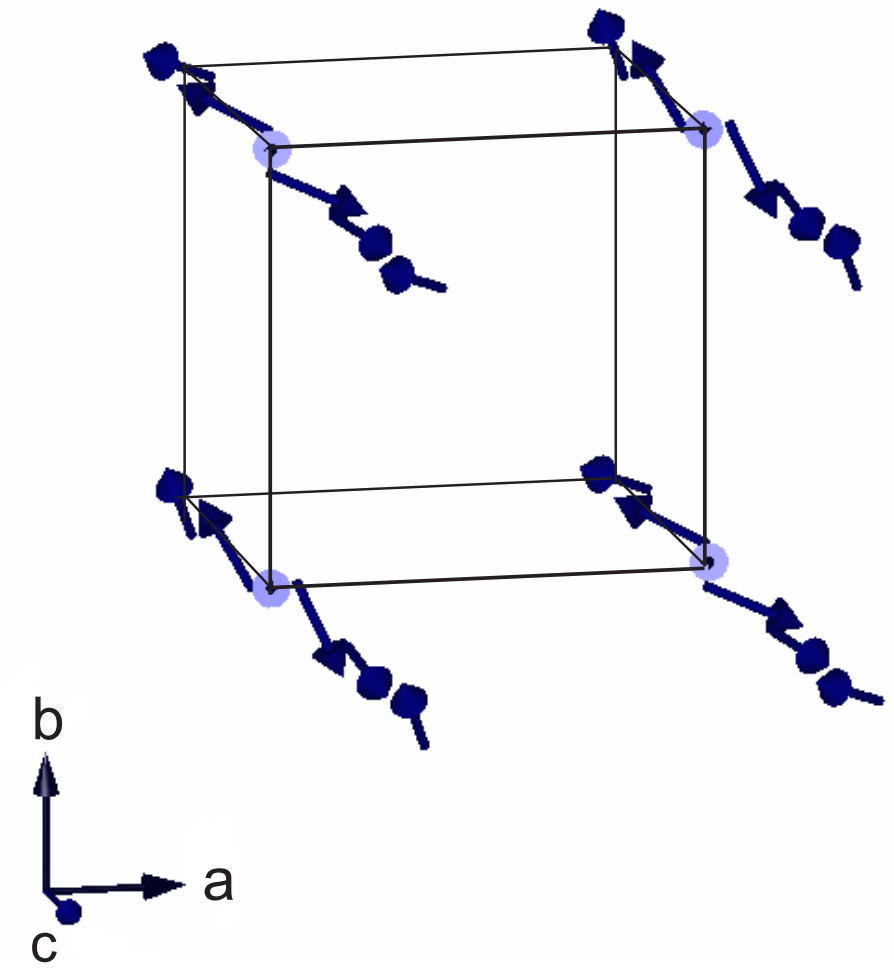

Figure 6.10: **$CuSb_2O_4$ Magnetic Structure.** The magnetic structure of $CuSb_2O_4$ at 432 mK. An incommensurate AFM helicoidal ordering is seen along the *c*-axis direction within the spin-chains.

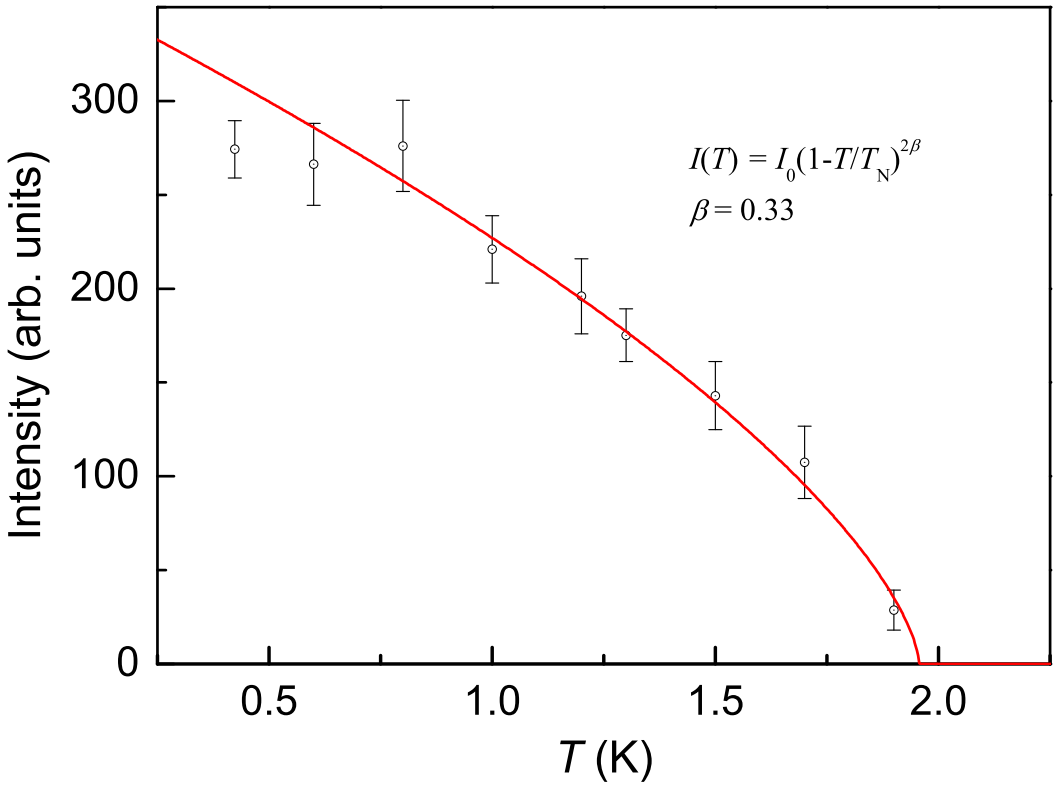

Figure 6.11: **$CuSb_2O_4$ Critical Power Law.** The temperature dependence of the integrated intensity of the magnetic Bragg reflection at $2\theta \approx 10°$ ($d \approx$ 13.8 Å). The solid red line represents a fit to a critical power law.

6.8 Magnetic Phase Diagram of $CuSb_2O_4$

$CuSb_2O_4$ exhibits multiple magnetic groundstates which depend on temperature and magnetic field. The (T, H) transition points from magnetization and heat capacity measurements were used to construct a magnetic phase diagram, shown in Figure 6.12. Magnetization field scans, heat capacity field scans and heat capacity temperature scans were performed to map the boundaries between the magnetic phases. Proposed boundary lines are also shown in Figure 6.12.

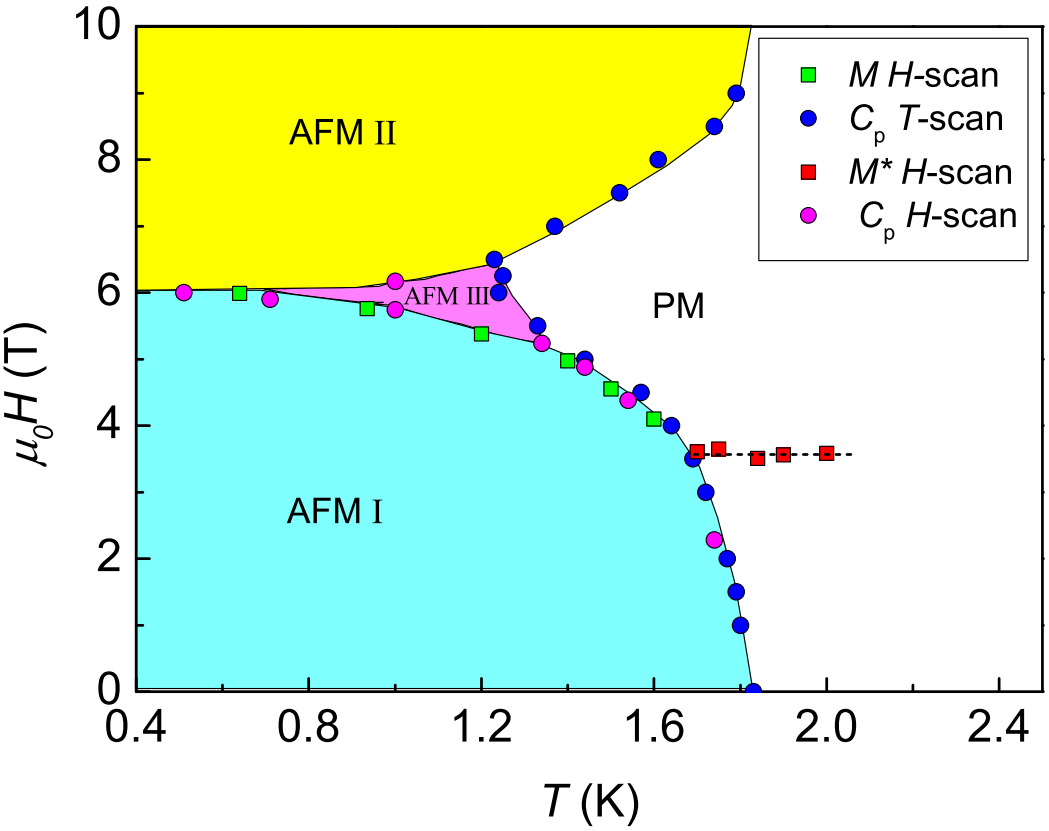

Figure 6.12: **$CuSb_2O_4$ Phase Diagram.** The (T, H) magnetic phase diagram of $CuSb_2O_4$. The black lines represent proposed phase boundary lines. The phase diagram is characterized by three order states (AFM I, AFM II, AFM III) and a paramagnetic state (PM).

$CuSb_2O_4$ is characterized by three ordered magnetic phases. The low temperature,

low field phase labeled "AFM I" is the incommensurate AFM ordering which has been characterized by the neutron diffraction results. $CuSb_2O_4$ transitions to the phase "AFM II" with the application of a magnetic field. The transition from Phase AFM I to AFM II is a spin-flop transition which is characterized by a reorientation of the magnetic moments. To obtain exact details of the AFM II state further neutron diffraction measurements with magnetic fields above 6 T are required. The pulsed high-field magnetization data indicated that magnetic saturation occurs at $\approx$ 14 T which would correspond to the upper boundary of AFM II (not shown in Figure 6.12).

The third phase, "AFM III", is a relatively small ordered phase which resides between the two AFM phases. The details of this third phase are currently unknown, further measurements to characterize the ordering are required. In the paramagnetic "PM" phase, a spin-flop transition is still visible with the magnetization measurements (red squares) for $T < 2$ K due to short-range correlations.

6.9 Electron Paramagnetic Resonance

EPR measurements were performed on a powder sample of $CuSb_2O_4$ in order to obtain the average g-factor and the temperature dependence of the g-factor. The g-factor obtained from EPR measurements can provide insight on the Cu^{2+} environment and its magnetic properties. The EPR spectra were measured with a 9.48 GHz microwave frequency in a temperature range of 4 K to 300 K. The spectra were fitted using a field derivative Lorentzian absorption resonance line, Eq. (3.16). Figure 6.13 displays the g-factor as a function of temperature. The g-factor increases linearly until $\approx$ 70 K at which point it reaches its maximum. The temperature position of the maximum corresponds approximately to the value of the NNN exchange constant J_{nnn} marked by the dashed line in Figure 6.13. This may be an indication of magne-

tostriction effects in the short-range ordered phase. The high temperature ($T > 100$ K) average g-factor amounts to

$$g = 2.104(1) \tag{6.5}$$

This high temperature averaged g-factor agrees with the expected value for a Cu^{2+} ion in an elongated octahedral environment.[101] Within error bars, the averaged g-factor for $CuSb_2O_4$ matches the value found for $CuAs_2O_4$. The measured g-factor indicates an effective magnetic moment of $\mu_{\text{eff}} = 1.82\ \mu_{\text{B}}$.

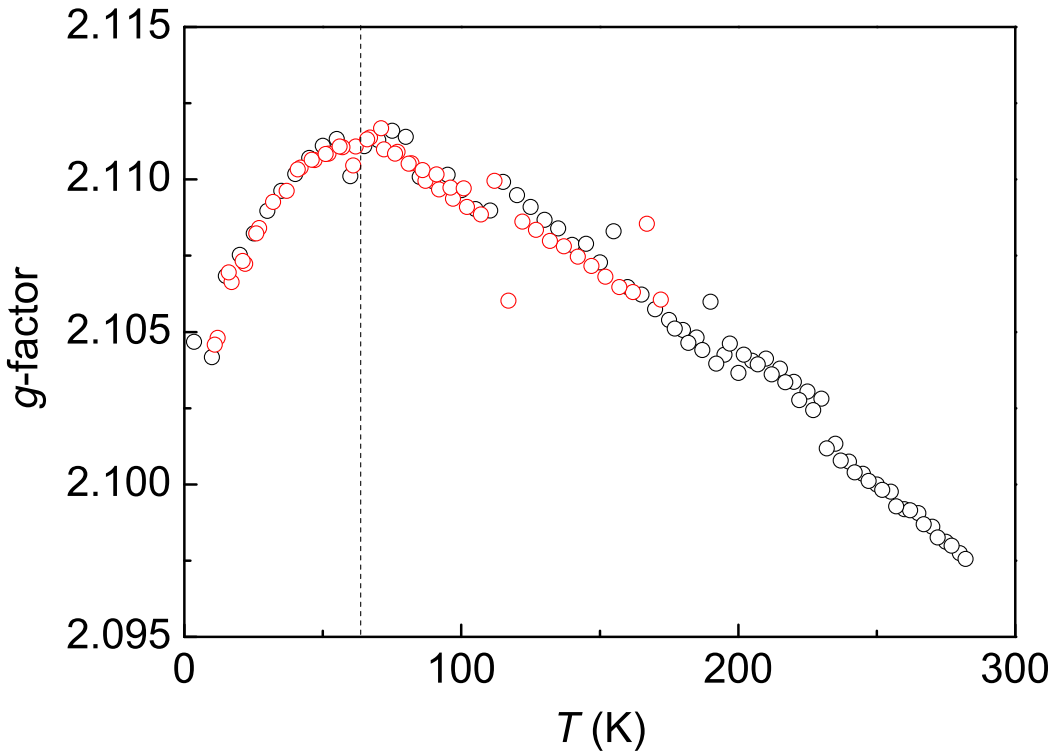

Figure 6.13: **$CuSb_2O_4$ g-factor.** The temperature dependence of the g-factor measured with EPR. The dashed line indicates the NNN exchange constant.

6.10 Dielectric Capacitance Spectroscopy

Dielectric capacitance measurements on $CuSb_2O_4$ were utilized for the characterization of the dielectric properties. $CuSb_2O_4$ powder was measured in a powder capacitance cell which compacts the sample powder between two metal plates to form the dielectric of a two-plate capacitor. The measurement was carried out in a ^{4}He cryostat with a temperature range of 1.3 K to 300 K and a maximum magnetic field of 6 T. Figure 6.14 displays the temperature dependent dielectric constant. The dielectric value appears to be minimally effected by magnetic field and frequency (not shown here). At the ordering temperature $T_N \approx 1.8$, a sharp increase in the dielectric constant is seen indicating a ferroelectric transition. Due to the limitations of the cryostat, only a minimum temperature of $\approx$ 1.3 K could be reached. For a conclusive characterization of the dielectric properties, measurements to lower temperatures requiring a ^{3}He insert are required.

Other spin-chain compounds which fall in the Highly Frustrated regime of the magnetic phase diagram have been found to exhibit ferroelectricity in the long-range ordered state, see Figure 2.9. The ferroelectric ordering is induced through a magnetostriction effect which causes a tiny structural distortion.[38] The structural distortion leads to a shift of the oxygen electron densities in the ribbon-chains resulting in a net polarization perpendicular across the ribbon-chains.

6.11 Conclusion

$CuSb_2O_4$ represents a rare example of a quantum spin-chain system with competing intrachain interactions. Structurally, $CuSb_2O_4$ is very similar to $CuAs_2O_4$. The crystal structure is characterized by edge sharing CuO_6 octahedra which give rise to CuO_2 ribbon-chains in their basal planes. The ribbon-chains exhibit competing

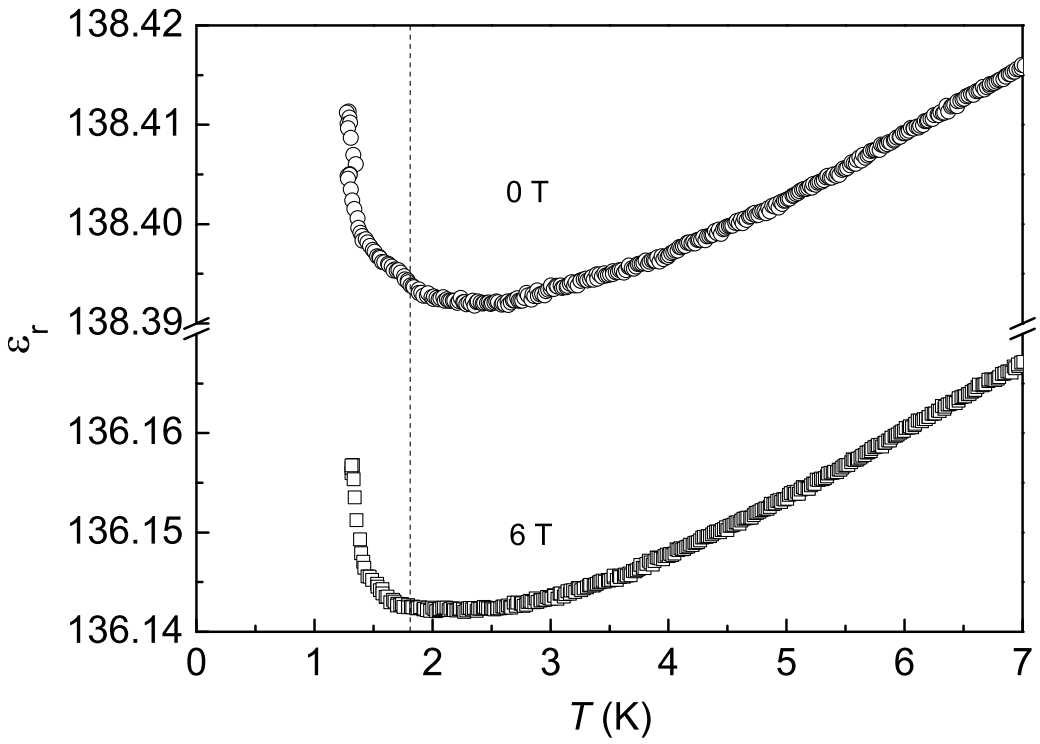

Figure 6.14: **$CuSb_2O_4$ Dielectric Constant.** Dielectric capacitance results measured at 0 and 6 T in a capacitance powder cell. Indications of ferroelectricity are seen below ≈ 1.5 K.

FM-NN and AFM-NNN spin-exchange interactions with $\alpha = J_{nn}/J_{nnn} \approx$ -1.8. This places $CuSb_2O_4$ in the "Highly Frustrated" regime of the groundstate phase diagram (Figure 2.7). Other spin-chain systems located in this regime, such as $NaCu_2O_2$, $LiCu_2O_2$, $LiCuVO_4$, and $PbCu(SO)_4(OH)_2$, also display helicoidal ordering. Of these compounds, $LiCuVO_4$ and $LiCu_2O_2$ have been found to also exhibit ferroelectricity in the magnetically ordered state. In this study, I have shown that $CuSb_2O_4$ displays helicoidal ordering which may be accompanied with ferroelectric order.

Low temperature magnetic susceptibility and heat capacity measurements showed that $CuSb_2O_4$ magnetically orders below $\approx$ 1.8 K. EPR measurements and a Curie-Weiss fit to the magnetic susceptibility indicated an average g-factor of $g \approx 2.10$ and a positive Curie-Weiss temperature reflecting the dominant FM-NN interactions. Inelastic neutron diffraction experiments revealed that the magnetic groundstate was incommensurate with helicoidal ordering. A three-ordered-phase diagram was complied using temperature and magnetic field scans in magnetization and heat capacity measurements. Indications of ferroelectricity in the magnetically ordered state were seen in the dielectric capacitance data. Further measurements of the dielectric capacitance down to lower temperatures are required to confirm the ferroelectric ordering. Elastic neutron diffraction experiments at magnetic fields above 6 T and temperatures below 1.7 K are necessary to characterize the high-field magnetic ordering phases.

7 Conclusions

In this thesis, I have reported experimental investigations on the structural and magnetic properties of two quasi-one-dimensional quantum spin-chain materials. The two compounds which have been studied are Copper arsenite $CuAs_2O_4$ and Copper antimonite $CuSb_2O_4$. $CuAs_2O_4$ and $CuSb_2O_4$ crystallize with very similar tetragonal crystal structures. Both compounds support Cu^{2+} spin-chains within CuO_2 ribbon-chains which are formed in the linked basal planes of edge sharing CuO_6 octahedra. Such ribbon-chain systems have been intensively investigated in the last decade because they may magnetically order with unconventional groundstates. The CuO_6 octahedra that harbor the ribbon-chains experience Jahn-Teller distortions which elongate the bonds between the central Cu ion and the two apical oxygens. Neighbouring CuO_2 ribbon-chains are largely separated and connected via $MO_3{}^{3-}$ groups (M = As^{3+}, Sb^{3+}) leading to quasi-one-dimensional magnetic behaviour. The Cu^{2+} ion has a $3d^9$ electronic configuration with S=1/2. $CuAs_2O_4$ and $CuSb_2O_4$ both exhibit strong magnetic frustration along the spin-chains arising from competing ferromagnetic nearest-neighbour and antiferromagnetic next-nearest-neighbour spin-exchange interactions. Despite the large number of similarities between $CuAs_2O_4$ and $CuSb_2O_4$, they give rise to very different magnetic properties. I present structural and magnetic characterizations with experimental results from x-ray diffraction, magnetic suscepti-

bility, heat capacity, neutron diffraction, Raman spectroscopy, electron paramagnetic resonance, and dielectric measurements. Additionally, I use hydrostatic pressure to further investigate a relationship between the structural and magnetic properties.

$CuAs_2O_4$ is characterized by ferromagnetic nearest-neighbour and antiferromagnetic next-nearest-neighbour spin-exchange interactions. The nearest-neighbour interactions are stronger by a factor of $\approx$ -4.1. $CuAs_2O_4$ exhibits long-range magnetic ordering below $T_C \approx 7.4$ K with a ferromagnetic groundstate. An extensive magnetic analysis was carried out which included magnetic susceptibility measurements with a comparison to theory, directional single-crystal magnetization measurements, and Arrott-Noakes analysis. The magnetic contribution to the heat capacity was estimated by fitting and subtracting the lattice contribution. Additional characterization measurements including electron paramagnetic resonance, Raman spectroscopy, and x-ray diffraction were carried out.

In order to establish a relationship between the structural and magnetic properties of $CuAs_2O_4$, an investigation using hydrostatic pressure was performed. Raman spectroscopy measurements with a diamond anvil cell revealed a structural phase transition at $\approx$ 9 GPa. The high-pressure phase of $CuAs_2O_4$ maintained a tetragonal crystal structure still supporting CuO_2 ribbon-chains, however with a symmetry reduction. The structural changes in the high-pressure phase were predominantly found in the distortions of the CuO_6 octahedra. Using single-crystal synchrotron x-ray diffraction experiments, it was observed that hydrostatic pressure suppresses the Jahn-Teller elongations in the CuO_6 octahedra. Additionally, it was found that hydrostatic pressure alters the Cu-O-Cu bonding angle along the ribbon-chains relevant for the nearest-neighbour super-exchange. The induced structural changes were followed with pressure and the results were used to calculate the intrachain spin-exchange interactions. Magnetization measurements under hydrostatic pressure were

carried out and found to exhibit correlated behaviour with the calculations. In the high-pressure phase, a severe alteration in the magnetic properties was observed with a removal of the magnetic frustration. Both the nearest- and next-nearest-neighbour interactions are ferromagnetic in the high-pressure with the next-nearest-neighbour interactions strongest by a factor of $J_{\mathrm{nn}}/J_{\mathrm{nnn}} \approx 0.3$.

$CuSb_2O_4$ features ferromagnetic nearest-neighbour and antiferromagnetic next-nearest-neighbour interactions with $J_{\mathrm{nn}}/J_{\mathrm{nnn}} \approx$ -1.8. $CuSb_2O_4$ shows long-range antiferromagnetic order below $T_{\mathrm{N}} \approx 1.8$ K with an unconventional groundstate. Using neutron diffractions measurements, it was found that $CuSb_2O_4$ orders with an incommensurate helicoidal magnetic structure in the antiferromagnetic state. Furthermore, indications of ferroelectricity were observed using dielectric capacitance measurements in the magnetically ordered state. A detailed (H, T) magnetic phase diagram was constructed using ^{3}He heat capacity and magnetization measurements. Magnetic saturation was found at $\approx$ 14 T with pulsed high-field magnetization experiments and compared to theory. The complex magnetic behaviour in $CuSb_2O_4$ arises from the frustration of the competing intrachain spin-exchange interactions. Additional characterizations included x-ray diffraction, Raman spectroscopy, and electron paramagnetic resonance measurements.

The next steps in the investigation of $CuAs_2O_4$ would be a detailed characterization of the magnetic structure below $\approx$ 7.4 K at ambient pressure. This would require neutron diffraction measurements on a large enough sample. A second future step would be a definitive characterization of the high-pressure magnetic properties. This could be accomplished with magnetic susceptibility measurements for pressures above 10 GPa, which would require modifications to the current diamond anvil cell, or neutron diffraction experiments above 10 GPa. Future work for the investigation of $CuSb_2O_4$ would include dielectric capacitance measurements in a ^{3}He cryostat to

fully characterize the ferroelectric transition. Furthermore, a characterization of the magnetic properties for the remaining two unsolved high-field phases in the magnetic phase diagram could be determined with low-temperature neutron diffraction experiments.

A

Temperature Independent Magnetic Contributions

The high temperature paramagnetic range of a magnetic susceptibility can be fitted to a Curie-Weiss Law,

$$\chi(T) = \frac{\mathrm{N_A}}{3k_B}\frac{g^2 S(S+1){\mu_\mathrm{B}}^2}{T-\theta_\mathrm{CW}} + \chi_0. \tag{A.1}$$

Where $\mathrm{N_A}$ is Avogadro's number, k_B is the Boltzmann constant, g is the g-factor, S is the spin, μ_B is the Bohr magneton and θ_CW is the Curie-Weiss temperature. χ_0 is the temperature independent offset of the susceptibility from Van Vleck paramagnetic and diamagnetic contributions.[41, 52]

$$\chi_0 = \frac{2N}{V}\sum_i \frac{|\left\langle 0\right| \mu_\mathrm{B}(\hat{L}+g\hat{S})\left|i\right\rangle|^2}{E_0 - E_i} - \frac{Ne^2\mu_0}{6Vm_\mathrm{e}}\sum_{j=1}^{Z_o}\left\langle {r_j}^2\right\rangle. \tag{A.2}$$

Because the diamagnetic and van Vleck contributions are temperature independent, they become noticeable at high temperatures as the Curie-Weiss-type magnetic susceptibility becomes small. If χ_0 is not properly accounted for a Curie-Weiss fit will yield incorrect values for the g-factor and Curie-Weiss temperature.

A.1 Diamagnetism

Diamagnetism is present in all materials to some extent, it is an induced magnetism which opposes any applied magnetic field. For a classical understanding of this effect, it is analogues to Lenz's law with an electron orbital viewed as a current loop. In this view, an applied magnetic field will change the frequency of the electrons orbit to induce an opposing magnetic field. However, diamagnetism is actually a quantum mechanical effect which can be described using first-order perturbation theory of the electron orbitals from the expression:[41]

$$\chi_{\text{dia}} = -\frac{Ne^2\mu_0}{6Vm_{\text{e}}} \sum_{j=1}^{Z_o} \left\langle {r_j}^2 \right\rangle . \tag{A.3}$$

This gives the diamagnetic contribution to the susceptibility from N magnetic ions with Z_o electrons in the outer shell of radius r_j. For simplicity one can approximate all electrons in the outer shell to have the same orbital radius so that $\sum_{j=1}^{Z_o} \left\langle {r_j}^2 \right\rangle \approx r^2 Z_o$.

An approximation of the diamagnetic contribution can be calculated using the tabulated values for individual ions from Selwood.[103] For a magnetic cuprate, χ_{dia} is typically around -100 $\times 10^{-6}$ $\frac{\text{cm}^3}{\text{mol}}$.

A.2 Van Vleck Paramagnetism

Van Vleck paramagnetism occurs in materials with open electron shells due to a mixing of the magnetic ground state with excited states. A correction to the ground state energy, E_0, can be described using second order perturbation theory,[41]

$$E^{(2)} = \sum_i \frac{|\left\langle 0 \right| \mu_{\text{B}} (\hat{L} + g\hat{S}) \cdot \vec{B} \left| i \right\rangle|^2}{E_0 - E_i}. \tag{A.4}$$

The correction to the magnetic susceptibility can then be calculated by $\chi = \frac{\partial^2 E^{(2)}}{\partial B^2}$.

Consider a magnetic Cu^{2+} ion centered in an O_6 octahedral environment. From the crystal field splitting, the e_g doublet and t_{2g} triplet will be split by ΔE with the doublet being the open orbital in the ground state. Van Vleck paramagnetism will come about from a small amount of mixing of the spin-hole with the t_{2g} orbitals. Typical values for the van Vleck contributions in cuprates are in the range of 90 to 130 $\times 10^{-6}$ $\frac{\text{cm}^3}{\text{mol}}$.[31] For most cuprate systems, the diamagnetic and van Vleck contributions almost cancel each other out, resulting in $\chi_0 \sim 10 \times 10^{-6}$ $\frac{\text{cm}^3}{\text{mol}}$.

Bibliography

[1] E. Ising, Z. Physik **31**, 253 (1925).

[2] N. Mermin and H. Wagner, Phys. Rev. Lett. **17**, 1133 (1966).

[3] L. D. Faddeev and L. A. Takhtajan, Phys. Lett. A **85**, 375 (1981).

[4] F. D. M. Haldane, Physics Letters **93A**, 464 (1983).

[5] F. D. M. Haldane, Phys. Rev. Lett. **50**, 1153 (1983).

[6] R. E. Peierls, *Quantum Theory of Solids* (Oxford University Press, London, 1955).

[7] E. Pytte, Phys. Rev. B **10**, 4637 (1974).

[8] P. Pincus, Solid State Commun. **9**, 22 (1971).

[9] J. W. Bray, H. R. Hart, J. L. V. Interrante, I. S. Jacobs, J. S. Kasper, G. D. Watkins, S. H. Wee, and J. C. Bonner, Phys. Rev. Lett. **35**, 744 (1975).

[10] M. Hase, I. Terasaki, and K. Uchinokura, Phys. Rev. Lett. **70**, 3651 (1993).

[11] R. M. Morra, W. J. L. Buyers, R. L. Armstrong, and K. Hirakawa, Phys. Rev. B **38**, 543 (1988).

[12] Z. Tun, W. J. L. Buyers, R. L. Armstrong, K. Hirakawa, and B. Briat, Phys. Rev. B **42**, 4677 (1990).

[13] T. Yokoo, T. Sakaguchi, K. Kakurai, and J. Akimitsu, J. Phys. Soc. Jpn. **64**, 3651 (1995).

[14] J. Darriet and L. P. Regnault, Solid State Commun. **86**, 409 (1993).

[15] Z. Tun, W. J. L. Buyers, A. Harrison, and J. A. Rayne, Phys. Rev. B **43**, 13331 (1983).

[16] W. J. L. Buyers, Z. Tun, A. Harrison, J. A. Rayne, and R. M. Nicklow, Physica B **180**, 222 (1992).

[17] H. Bethe, Z. Phys. **71**, 205 (1931).

[18] B. Lake, Nature Physics **1**, 143 (2005).

[19] D. A. Tennant, T. G. Perring, R. A. Cowley, and S. E. Nagler, Phys. Rev. Lett. **70**, 4003 (1993).

[20] B. Lake, D. A. Tennant, J. S. Caux, T. Barthel, U. Schollwöck, S. E. Nagler, and C. D. Frost, Phys. Rev. Lett. **111**, 137205 (2013).

[21] M. Arai, M. Fujita, M. Motokawa, J. Akimistu, and S. Bennington, Phys. Rev. Lett. **77**, 3649 (1996).

[22] M. Fujita, C. D. Frost, S. M. Bennington, R. Kajimoto, M. Nakamura, Y. Inamura, F. Mizuno, K. Ikeuchi, and M. Arai, J. Phys. Soc. Jpn. **82**, 084708 (2013).

[23] M. Enderle, B. Fåk, H.-J. Mikeska, R. K. Kremer, A. Prokofiev, and W. Assmus, Phys. Rev. Lett. **104**, 237207 (2010).

[24] S. Masatoshi, Y. Yukio, K. Yoshiaki, S. Kenji, N. Yutaka, T. Yasuko, and K. Yuji, Solid State Sci. **12**, 670 (2010).

[25] J. Sudan, A. Lüscher, and A. M. Läuchli, Phys. Rev. B **80**, 140402(R) (2009).

[26] S. Furukawa, M. Sato, and S. Onoda, Phys. Rev. Lett. **105**, 257205 (2010).

[27] M. Enderle, Habilitation thesis, Universität des Saarlandes (1999).

[28] B. J. Gibson, R. K. Kremer, A. V. Prokofiev, W. Assmus, and G. J. McIntyre, Physica B **350**, e253 (2004).

[29] M. Enderle, C. Mukherjee, B. Fåk, R. K. Kremer, J.-M. Broto, H. Rosner, S.-L. Drechsler, J. Richter, J. Malek, A. Prokofiev, et al., Europhys. Lett. **70**, 237 (2005).

[30] L. Zhao, T.-L. Hung, C.-C. Li, Y.-Y. Chen, M.-K.Wu, R. K. Kremer, M. G. Banks, A. Simon, M.-H. Whangbo, C. Lee, et al., Adv. Mater. **24**, 2469 (2012).

[31] M. G. Banks, R. K. Kremer, C. Hoch, A. Simon, B. Ouladdiaf, J.-M. Broto, H. Rakoto, C. Lee, and M.-H. Whangbo, Phys. Rev. B **80**, 024404 (2009).

[32] T. Masuda, A. Zheludev, A. Bush, M. Markina, and A. Vasiliev, Phys. Rev. Lett. **92**, 177201 (2004).

[33] S. Park, Y. J. Choi, C. L. Zhang, and S.-W. Cheong, Phys. Rev. Lett. **98**, 057601 (2007).

[34] B. Willenberg, M. Schäpers, K. C. Rule, S. Süllow, M. Reehuis, H. Ryll, B. Klemke, K. Kiefer, W. Schottenhamel, B. Büchner, et al., Phys. Rev. B **108**, 117202 (2012).

[35] A. U. B. Wolter, F. Lipps, M. Schäpers, S.-L. Drechsler, S. Nishimoto, R. Vogel, V. Kataev, B. Büchner, H. Rosner, M. Schmitt, et al., Phys. Rev. B **85**, 014407 (2012).

[36] S.-L. Drechsler, N. Tristan, R. Klingeler, B. Büchner, J. Richter, J. Málek, O. Volkova, A. Vasiliev, M. Schmitt, A. Ormeci, et al., J. Phys.: Condens. Matter **19**, 145230 (2007).

[37] L. Capogna, M. Mayr, P. Horsch, M. Raichle, R. K. Kremer, M. Sofin, A. Maljuk, M. Jansen, and B. Keimer, Phys. Rev. B **71**, 140402(R) (2005).

[38] H. J. Xiang and M.-H. Whangbo, Phys. Rev. Lett. **99**, 257203 (2007).

[39] Y. Naito, K. Sato, Y. Yasui, Y. Kobayashi, and M. Sato, J. Phys. Soc. Jpn. **76**, 023708 (2007).

[40] S. Seki, T. Kurumaji, S. Ishiwata, H. Matsui, H. Murakawa, Y. Tokunaga, Y. Kaneko, T. Hasegawa, and Y. Tokura, Phys. Rev. B **82**, 064424 (2010).

[41] S. Blundell, *Magnetism in Condensed Matter* (Oxford University Press Inc., New York, 2001).

[42] D. C. Johnston, R. K. Kremer, M. Troyer, X. Wang, A. Klümper, S. L. Bud'ko, A. F. Panchula, and P. C. Canfield, Phys. Rev. B **61**, 9558 (2000).

[43] J. C. Bonner and M. E. Fisher, Phys. Rev. **135**, A640 (1964).

[44] J. M. Law, H. Benner, and R. K. Kremer, J. Phys.: Condens. Matter **7**, 8605 (2013).

[45] R. L. Carlin, *Magnetochemistry* (Springer-Verlag, Berlin, 1986).

[46] L. Onsager, Phys. Rev. **65**, 117 (1944).

[47] R. M. F. Houtappel, Physica. **16**, 425 (1950).

[48] J. B. Goodenough, Phys. Rev. **100**, 564 (1955).

[49] J. Kanamori, J. Phys. Chem. Solids **10**, 87 (1959).

[50] P. W. Anderson, Solid State Phys. **14**, 99 (1963).

[51] D. Bloch, J. Phys. Chem. Solids **27**, 881 (1966).

[52] C. Kittel, *Introduction to Solid State Physics - 8th ed.* (John Wiley & Sons, Inc., Hoboken, N.J., 2005).

[53] T. M. Dunn, Trans. Faraday Soc. **57**, 1441 (1961).

[54] H. A. Jahn and E. Teller, Proc. Royal Soc. **161**, 220 (1937).

[55] R. Bursill, G. A. Gehring, D. J. J. Farnell, J. B. Parkinson, T. Xiang, and C. Zeng, J. Phys.: Condens. Matter **7**, 8605 (1995).

[56] G. Toulouse, Commun. Phys. **2**, 115 (1977).

[57] T. Hikihara, M. Kaburagi, and H. Kawamura, Phys. Rev. B **63**, 174420 (2001).

[58] C. K. Majumdar and D. K. Ghosh, J. Math. Phys. **10**, 1388 (1969).

[59] C. K. Majumdar and D. K. Ghosh, J. Math. Phys. **10**, 1399 (1969).

[60] M. Braden, G. Wilkendorf, J. Lorenzana, M. Aïn, G. J. McIntyre, M. Behruzi, G. Heger, G. Dhalenne, and A. Revcolevschi, Phys. Rev. B **54**, 1105 (1996).

[61] S. Lebernegg, M. Schmitt, A. A. Tsirlin, O. Janson, and H. Rosner, Phys. Rev. B **87**, 155111 (2013).

[62] W. Geertsma and D. Khomskii, Phys. Rev. B **54**, 3011 (1996).

[63] K. Fabricius, A. Klümper, U. Löw, B. Büchner, T. Lorenz, G. Dhalenne, and A. Revcolevschi, Phys. Rev. B **57**, 1102 (1998).

[64] J. M. Law, P. Reuvekamp, R. Glaum, C. Lee, J. Kang, M.-H. Whangbo, and R. K. Kremer, Phys. Rev. B **84**, 014426 (2011).

[65] L. E. Svistov, L. A. Prozorova, A. A. Bush, and K. E. Kamentsev, J. Phys.: Conf. Ser. **200**, 022062 (2010).

[66] H. J. Xiang, C. Lee, and M.-H. Whangbo, Phys. Rev. B **76**, 220411(R) (2007).

[67] K. Caslin, R. K. Kremer, F. S. Razavi, A. Schulz, A. Muñoz, F. Pertlik, J. Liu, M.-H. Whangbo, and J. M. Law, Phys. Rev. B **89**, 014412 (2014).

[68] J. Rodriguez-Carvajal, Physica B **192**, 55 (1993).

[69] M. Merlini and M. Hanfland, High Press. Res. **33**, 511 (2013).

[70] H. K. Mao, J. Xu, and P. M. Bell, J. Geophys. Res. **91**, 4673 (1986).

[71] Oxford Diffraction: Data collection and data reduction GUI; CrysAlis Pro, version 171.34.44, Oxford Diffraction Ltd. (2010).

[72] Cf. http://wwwba.ic.cnr.it/content/sir2011-v10.

[73] Cf. http://www.xtl.ox.ac.uk/crystals.html.

[74] V. Petricek, M. Dusek, and L. Palatinus, Z. Kristallogr. **229**, 345 (2014).

[75] J. Clark and A. I. Braginski, *The SQUID Handbook, Vol. 2: Applications of SQUIDs and SQUID Systems* (Wiley-VCH, New York, 2006).

[76] N. Tateiwa, Y. Haga, Z. Fisk, and Y. Ōnuki, Rev. Sci. Instr. **82**, 053906 (2011).

[77] N. Tateiwa, Y. Haga, D. Matsuda, and Z. Fiski, Rev. Sci. Instr. **83**, 053906 (2012).

[78] A. Eiling and J. S. Schilling, J. Phys. F: Metal Phys. **11**, 623 (1981).

[79] R. Lortz, Private Communication (2015).

[80] R. K. Kremer, Unpublished (2014).

[81] *Quantum Design Physical Properties Measurement System: Heat Capacity Option User's Manual* (2004).

[82] K. Syassen, High Press. Res. **28**, 75 (2008).

[83] Cf. www.ill.eu/instruments-support/instruments-groups/instruments/d20/.

[84] Andeen-Hagerling, *AH2700A 50 Hz - 20 kHz Ultra Precision Capacitance Bridge: Operation and Maintenance Manual* (2003).

[85] J. Zemann, TMPM Tschermaks Min. Petr. Mitt. **2**, 417 (1951).

[86] F. Pertlik, TMPM Tschermaks Min. Petr. Mitt. **22**, 211 (1975).

[87] F. Pertlik, Z. Anorg. Allg. Chem. **436**, 201 (1977).

[88] B. Hinrichsen, R. E. Dinnebier, P. Rajiv, M. Hanfland, A. Grzechnik, and M. Jansen, J. Phys.: Condens. Matter **18**, S1021 (2006).

[89] S. Kharbish, J. Geosciences **57**, 53 (2012).

[90] M. Whangbo, H. Koo, and D. Dai, J. Solid State Chem. **176**, 417 (2003).

[91] H. J. Xiang, C. Lee, H.-J. Koo, X. G. Gong, and M.-H. Whangbo, Dalton Trans. **42**, 823 (2013).

[92] D. Dai and M. Whangbo, J. Chem. Phys. **114**, 2887 (2001).

[93] D. Dai and M. Whangbo, J. Chem. Phys. **118**, 29 (2003).

[94] P. Blöchl, Phys. Rev. B **50**, 17953 (1994).

[95] G. Kresse and D. Joubert, Phys. Rev. B **59**, 1758 (1999).

[96] G. Kresse and J. Furthmüller, Phys. Rev. B **54**, 11169 (1996).

[97] J. P. Perdew, A. Ruzsinszky, G. I. Csonka, O. A. Vydroz, G. E. Scuseria, L. A. Constantin, X. L. Zhou, and K. Burke, Phys. Rev. Lett. **100**, 136406 (2008).

[98] S. L. Dudarev, G. A. Botton, S. Y. Savrasov, C. J. Humphreys, and A. P. Sutton, Phys. Rev. B **57**, 1505 (1998).

[99] H. J. Schulz, Phys. Rev. Lett. **77**, 2790 (1996).

[100] H. Rosner, H. Eschrig, R. Hayn, S.-L. Drechsler, and J. Málek, Phys. Rev. B **56**, 3402 (1997).

[101] A. Abragam and B. Bleaney, *Electron Paramagnetic Resonance of Transition Ions* (Clarendon Press, Oxford, 1970).

[102] J. A. Weil, J. R. Bolton, and J. E. Wertz, *Electron Paramagnetic Resonance. Elementary Theory and Practical Applications* (Wiley, New York, 1994).

[103] P. W. Selwood, *Magnetochemistry* (Interscience, New York, 1956).

[104] M. Takigawa, P. C. Hammel, R. H. Heffner, Z. Fisk, J. L. Smith, and R. B. Schwarz, Phys. Rev. B **39**, 300 (1989).

[105] H. J. Koo, M.-H. W. C. Lee, G. J. McIntyre, and R. K. Kremer, Inorg. Chem. **50**, 3582 (2011).

[106] R. Bursill, T. Xiang, and G. A. Gehring, J. Phys.: Cond. Matter **8**, L583 (1996).

[107] X. Wang and T. Xiang, Phys. Rev. B **56**, 5061 (1997).

[108] A. Arrott and J. E. Noakes, Phys. Rev. Lett. **19**, 786 (1967).

[109] J. C. LeGuillou and J. Zinn-Justin, Phys. Rev. Lett. **39**, 95 (1977).

[110] J. C. LeGuillou and J. Zinn-Justin, Phys. Rev. B **21**, 3976 (1980).

[111] R. Reisser, R. K. Kremer, and A. Simon, Physica. B **204**, 265 (1995).

[112] R. J. Goetsch, V. K. Anand, A. Pandey, and D. C. Johnston, Phys. Rev. B **85**, 054517 (2012).

[113] S.-L. Drechsler, O. Volkova, A. N. Vasiliev, N. Tristan, J. Richter, M. Schmitt, H. Rosner, J. Málek, R. Klingeler, A. A. Zvyagin, et al., Phys. Rev. Lett. **98**, 077202 (2007).

[114] M. Schmitt, J. Málek, S.-L. Drechsler, and H. Rosner, Phys. Rev. B **80**, 205111 (2009).

[115] R. O. Kuzian, S. Nishimoto, S.-L. Drechsler, J. Málek, S. Johnston, J. van den Brink, M. Schmitt, H. Rosner, M. Matsuda, K. Oka, et al., Phys. Rev. Lett. **109**, 117207 (2012).

[116] P. Vinet, J. R. Smith, J. Ferrante, and J. H. Rose, Phys. Rev. B **35**, 1945 (1987).

[117] R. Fischer and F. Pertlik, Mineral. Petrol. **22**, 236 (1975).

[118] B. Hinrichsen, R. E. Dinnebier, P. Rajiv, M. Hanfland, A. Grzechnik, and M. Jansen, J. Phys.: Cond. Matter **18**, S1021 (2007).

[119] J. A. Gonzalo, D. E. Cox, and G. Shirane, Phys. Rev. **147**, 415 (1966).

[120] R. Charter, J. R. Gavarri, and A. Hewat, J. Solid State Chem. **60**, 78 (1985).

[121] G. Gorodetsky, M. Sayar, and S. Shtrikman, Mat. Res. Bull. **5**, 253 (1970).

[122] A. Iyama, Y. Wakabayashi, N. Hanasaki, and T. Kimura, Jpn. J. Appl. Phys. **53**, 05FB02 (2014).

[123] A. P. Ramirez, Annu. Rev. Mater. Sci. **24**, 453 (1994).

[124] W. W. Focke, S. S. Mkhize, R. Storey, O. D. Fabbro, and E. Muller, Chem. Eng. Comm. **201**, 153 (2014).

[125] M. T. Atanasova, A. M. Strydom, C. J. H. Schutte, L. C. Prinsloo, and W. W. Focke, J. Mater Sci. **49**, 3497 (2014).

[126] F. Heidrich-Meisner, A. Honecker, and T. Vekua, Phys. Rev. B **74**, 020403(R) (2006).